Politecnico di Torino

Politecnico di Torino

Master of Science in Mechanical Engineering
Graduation Session July 2025
Academic Year 2024/2025

Master Thesis

Design of Ultralight Inflatable Antenna for Low Earth Orbit: Lorentz Force-Based Orientation

Feasibility study

Supervisors:
Prof.ssa Raffaella Sesana
Prof. Ladislau Matekovits

Candidate:
Simone Pacetti

Table of Contents

List of Figures

List of Tables

1. ABSTRACT

This thesis investigates the preliminary feasibility study of a new class of ultra-light inflatable antennas with a large transmitting and receiving surface composed of metallized fabric. These antennas are designed for deployment in Low Earth Orbit (LEO), at approximately 2000 km altitude from sea level. The orientation is controlled through the interaction between the Earth's magnetic field and electric currents induced within conductive elements embedded in the antenna's structure. This innovative control method eliminates the need for traditional mechanical actuators or booms, reducing complexity, mass, and transportation cost to space, while increasing operational efficiency.

A critical challenge associated with inflatable antennas is deployment and ensuring structural integrity of the membrane. Historical NASA experiments with inflatable space antennas were conducted in the 20th century, revealing a high failure rate due to uncontrolled inflation in vacuum conditions, leading to sudden structural collapse. This thesis addresses these concerns by conducting a pre-feasibility study on suitable materials specifically selected, inflation techniques, and rigidization methods. The selected inflation strategy ensures safe and controlled deployment, while rigidization mechanisms provide long-term structural stability, reducing the effects of micrometeoroid impacts and material degradation over time.

In addition to structural considerations, this work explores power generation solutions necessary for antenna operation. Advanced photovoltaic technologies, including new generation lightweight and flexible solar cells, are evaluated as a means of supplying power to the system. These solar cells can be integrated onto the antenna's surface or deployed on an auxiliary CubeSat operating in proximity to the antenna, enabling wireless energy transfer and improving mission sustainability.
The inflatable antenna structure is designed as a spheroid, with the southern hemisphere forming a parabolic reflective surface composed of metallized fabric, while the northern hemisphere remains transparent to electromagnetic radiation. The proposed system holds significant potential for aerospace applications, including radio astronomy and deep-space communication.

Through structural simulations, material selection studies, and power system evaluations, this thesis lays the groundwork for further development of inflatable antennas for space applications. While the findings confirm the feasibility of this innovative concept, additional experimental validation and optimization are required to transition from theoretical analysis to practical implementation in orbit.

Target

This thesis focuses on several critical aspects necessary for the successful realization of the proposed antenna system. First, the structural integrity of the inflatable membrane is analyzed, considering material selection, deployment mechanisms, and rigidization techniques. The research evaluates potential materials, such as metallized Mylar and other multi-layer composites, to ensure durability against space environmental factors, including atomic oxygen, micrometeoroid impacts, and extreme thermal variations. Furthermore, different inflation and rigidization strategies are examined to achieve a stable and long-lasting operational configuration in orbit.

Furthermore, power supply solutions are examined. The integration of lightweight and high-efficiency solar arrays is analyzed to determine the feasibility of generating sufficient power for the antenna's operation. The study also evaluates whether solar cells should be mounted directly onto the antenna's surface or deployed on an auxiliary CubeSat that remains near the antenna, enabling remote control.

Another key objective of this work is the development of a control methodology capable of achieving precise orientation of the inflatable antenna. By modulating electric currents within embedded conductive elements, the structure can generate distributed electromagnetic forces sufficient to induce controlled rotational motion. Dedicated simulations have been carried out to analyze the relationship between applied current and maneuver time, with the aim of identifying optimal parameters for effective and reliable control.

2. Introduction

Principal missions overview and design concepts

The development of large inflatable structures for space applications has its roots in the early 1960s, when the United States successfully launched two large-diameter passive communication satellites, Echo 1 and Echo 2 [1][2]. These pioneering missions represented the first attempts to deploy ultralight spherical satellites made of metallized thin films. Echo 1 was placed in an elliptical orbit with an apogee of approximately 2157 km and a perigee of 966 km, had a diameter of 30.48 meters, and was constructed using a Mylar polyester film with a thickness of 12.7 μm [1]. Echo 2, launched shortly thereafter, featured a larger diameter of 41 meters and was composed of a Mylar film (9 μm) sandwiched between two layers of aluminum foil (each 4.5 μm thick), and was inserted in an orbit ranging between 1029 km and 1316 km in altitude [2].

Since both satellites had a spherical geometry and operated solely as passive radio wave reflectors, there weren't active orientation system. From that time onward, significant research efforts have been dedicated to studying the feasibility of deploying large inflatable antennas in space. In the 1980s, the European Space Agency (ESA) initiated a study for a 15-meter inflatable antenna based on the space rigidized concept. The antenna was intended for integration into QUASAT, a radio astronomy satellite designed to operate in conjunction with the Very Long Baseline Interferometry (VLBI) networks in Europe and the United States. QUASAT was conceived to function across multiple wavelengths, specifically 1.35 cm, 6 cm, 18 cm, and 92 cm [3].

Following these early European initiatives, further advancements were made during the 1990s and early 2000s by NASA's Jet Propulsion Laboratory (JPL), which led several projects exploring inflatable structures. In 1998, the ARISE (Advanced Radio Interferometry between Space and Earth) team at JPL published a detailed concept study describing a deployable satellite equipped with a 30 meter inflatable antenna in an elliptical orbit with a perigee of 5000 km and an apogee of 40000 km. At the same time, efforts were also pursued by the aerospace firm L'Garde Inc., which developed a variety of designs and materials tailored to inflatable space systems [3].

It's important to note that in all these cases, the antennas were mechanically oriented by the spacecraft using extended booms or structural appendages. In contrast, the present work proposes an innovative approach in which the antenna structure itself can generate distributed, low-intensity forces across its surface to orient itself without requiring mechanical actuation from the hosting satellite.

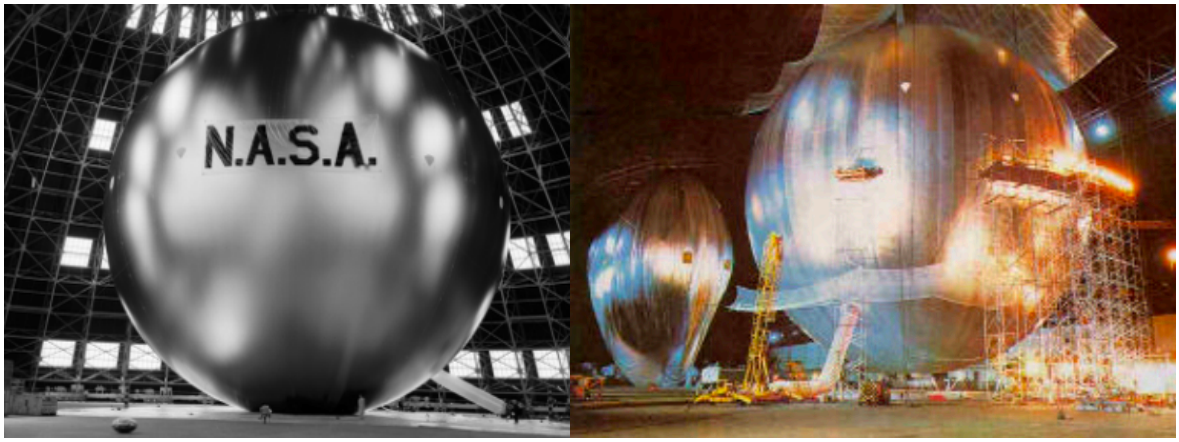

Figure 2.1 - Echo 1 Satellite (left), Echo 2 Satellite (right) [21][23]

3. Materials for ultra-light inflatable antenna

As the demand for advanced space technologies continues to grow, the development of ultra-light inflatable antennas has emerged as a crucial innovation for satellite and space exploration missions. These antennas offer significant advantages in terms of weight, compactness, and ease of deployment, making them ideal for applications in Low Earth Orbit (LEO). However, the success of these antennas largely depends on the selection of appropriate materials which can withstand the harsh conditions of the space environment while maintaining their structural integrity and performance.

In this chapter, the critical aspects of material selection for ultra-light inflatable antennas will be explored, focusing on the unique challenges and requirements these materials must meet to ensure optimal functionality in the space environment. The selection of suitable materials is not merely a matter of reducing weight but also ensuring durability and reliability over the antenna's operational lifetime. In particular, the lifetime of these objects is an important aspect, which will be better discussed in following chapters. Rigidization techniques will be also analyzed, since it has been proved that they can increase inflatable antennas lifetime.

Another important aspect is how to orient the object itself if it must behave like an antenna. Indeed, the extreme thickness of the walls together with their extremely large dimensions imposes to exercise a diffuse, weak but regular force to slowly turn the antenna in the right direction, in order not to introduce deformations and to induce instabilities in the envelope itself. Additionally, the chapter explores various folding techniques which can facilitate deployment and help avoiding critical damage or deformations during inflation. [41]

3.1. Environmental Parameters in LEO

The space environment can be particularly challenging, and it is crucial to evaluate every parameter to safely deploy an inflatable antenna. So, before choosing the most suitable material for our application, it is presented an overview of the environmental parameters which characterize the LEO space. Temperature in LEO expose materials to repeated cycles of intense sunlight and deep space cold, requiring them to withstand such thermal cycling without compromising performance. The constant exposure to solar ultraviolet radiation further demands that materials have high UV resistance Moreover, the presence of cosmic rays and solar particles subject materials to high-energy impacts, leading to atomic displacement and material damage.

Another important factor to consider is the significant presence of atomic oxygen, which poses a threat through erosion and degradation of exposed materials. This challenge necessitates the use of protective coatings or the selection of materials that are inherently resistant to such erosion. Furthermore, the material must demonstrate sufficient impact resistance to endure the collisions with micrometeoroids and orbital debris that are prevalent in LEO. A robust material, combined with a rigidization process, helps to minimize the risk of puncture and ensures the structure can survive impacts that would otherwise be fatal. The vacuum of space imposes strict requirements on material integrity. In such conditions, materials must exhibit minimal outgassing or sublimation, as these phenomena can compromise structural integrity.

3.2. Material Requirements

In this section, it will be analyzed specific requirements for materials used in the construction of ultra-light inflatable antennas intended for deployment in LEO. It is important to note that in inflatable space structures used as antennas, the materials for the reflector and the transparent canopy are not

the same [16]. The reflector portion is typically made of a metallized membrane to reflect and focus solar or radio frequency energy, while the canopy, which forms the other half of the structure, must be transparent to the wavelength of interest.

The production process must be conducted considering that the reflector is designed to achieve high surface precision, while the canopy does not require the same level of surface accuracy. The reflector is stressed to a higher pressure to maintain its shape and reflective properties, whereas the canopy is designed to provide structural support without needing the same precision. In this special application of inflatable space structures, particularly those used as antennas, the materials must respect the following requirements.

3.2.1. Mechanical Properties

The selected material for the inflatable antenna must satisfy several critical requirements to ensure both performance and reliability throughout its mission. First, it must demonstrate high tensile strength, as this property is essential to endure the stresses encountered during both the deployment phase and the subsequent operational period. In particular, the material's durability is important to withstand impacts from micrometeoroids, and to address this, a rigidization process has been planned to reinforce its structure once deployed.

Flexibility is another key characteristic; the material must be capable of accommodating significant elastic deformations, enabling compact stowage within the limited volume of the launch vehicle and reliable inflation upon reaching orbit. Minimizing the mass of the structure is another objective to reduce launch costs and facilitate the deployment of larger and more capable antenna systems. The choice of material must also account for its Young's modulus. A low modulus is desirable, as it ensures that the material can accommodate elastic deformations without sustaining damage, thereby contributing to the achievement of the antenna's final shape under internal pressure. Furthermore, the material must exhibit low long-term creep, resisting any deformation that might occur over extended periods of continuous load or pressure. This characteristic is fundamental for ensuring the antenna's shape stability and operational longevity.

It is equally important that the material can withstand the internal pressures generated during the inflation phase. Several spacecraft collapsed during this phase in the past. Although the surface will eventually be rigidized to ensure structural integrity, the material must initially resist collapse or deformation that could compromise the deployment process. It also must support efficient mechanical packaging, allowing the antenna to be stowed compactly for launch and to deploy seamlessly once in orbit. [9][10]

3.2.2. Thermal Properties

The material must exhibit excellent thermal stability, ensuring that its mechanical properties remain consistent across the wide temperature fluctuations typically encountered in LEO. In addition to stability, the material must possess a low coefficient of thermal expansion to mitigate the effects of temperature variations on the antenna's dimensions. Minimal thermal expansion is essential to preserve the precise shape and alignment of the antenna, which is fundamental for maintaining its functional accuracy.

Furthermore, the operational temperature range of the material must be sufficiently broad to withstand the extreme variations present in LEO, typically spanning from approximately -65°C to 150°C. Adequate thermal conductivity is necessary to enable the dissipation of heat, thus preventing the

formation of localized hotspots that could potentially compromise the material's integrity. [11][12][37][33]

3.2.3. Radiation Resistance

The material must possess also high resistance to ultraviolet radiation, as prolonged exposure to intense solar UV rays in the space environment can lead to rapid degradation of material properties. Ensuring that the material retains its integrity in such conditions is paramount to the long-term functionality of the antenna. In addition, it must also demonstrate resistance to ionizing radiation, which includes high-energy particles that can penetrate and weaken material structures over time. The persistent presence of these particles in orbit necessitates a material that does not suffer significant embrittlement or damage because of cumulative radiation exposure. In some applications, it may also be necessary for the material to provide a degree of radiation shielding to protect sensitive electronic components housed within the antenna structure. This protective capability can mitigate the negative effects of radiation on critical systems, ensuring continued functionality and extending the operational lifespan.[13][14]

3.2.4. Chemical Properties

The material must exhibit low outgassing characteristics, as the presence of volatile compounds can lead to contamination of sensitive equipment and surfaces in the vacuum of space. This property is crucial for preserving the performance and reliability of both the antenna and any nearby components. In addition to limiting outgassing, the material must demonstrate chemical inertness to ensure its stability in the presence of the reactive atomic oxygen that is prevalent in LEO. By maintaining its shape and mechanical performance despite continuous exposure to atomic oxygen, the material ensures that the inflatable antenna remains effective and reliable throughout its mission in the challenging environment of space.

3.2.5. Manufacturability and Lifetime

The materials should be easy to handle, process, and bond, which is essential for the construction of inflatable structures. The mission is considered successfully if the antenna lifetime span is 6 to 12 months. [15][16]

3.3. Inflation techniques

As mentioned before, this kind of antennas show many advantages, mainly correlated to their capability to be stowed in small volume. Once the deployment is completed in the expected orbit, these objects must be inflated to reach the desired final form. [16]
Inflation gas provides post-deployment structural rigidity for a finite period, then due to tiny imperfection in the antenna skin the gas will leak out. Those pinholes may appear for different reasons, for example manufacture, folding or impact with micrometeorites. [14]
Moreover, the gas pressure depends on the structure dimension, larger ones tend to require lower inflation pressure, perhaps a few pascals. To increase the lifetime a Rigidization phase is often planned following deployment, process which will be discussed in the following chapter.
It will be presented an overview of the most used inflation techniques for inflatable antenna orbiting in LEO region. [23]
The Inflation techniques for ultra-light inflatable antenna follows.

3.3.1. Gas Inflation

This technique involves using inert gases stored in pressurized tanks that are released to inflate the structure. The gas expands and fills the inflatable antenna, providing the necessary shape and rigidity. Some examples of gases which can be used in this application are:

- Nitrogen (N_2): Commonly used due to its inert nature and availability. Nitrogen gas inflation is reliable and has been used in several space missions.
- Helium (He): Another inert gas, lighter than nitrogen. Helium is often used in applications where minimizing weight is crucial.

Using directly gases lead to some advantages, like a simpler mechanism, reliable and well-understood technology. Nevertheless, it requires precise control to avoid over- or under-inflation. The gas storage system adds weight and volume to the payload. [17][18]

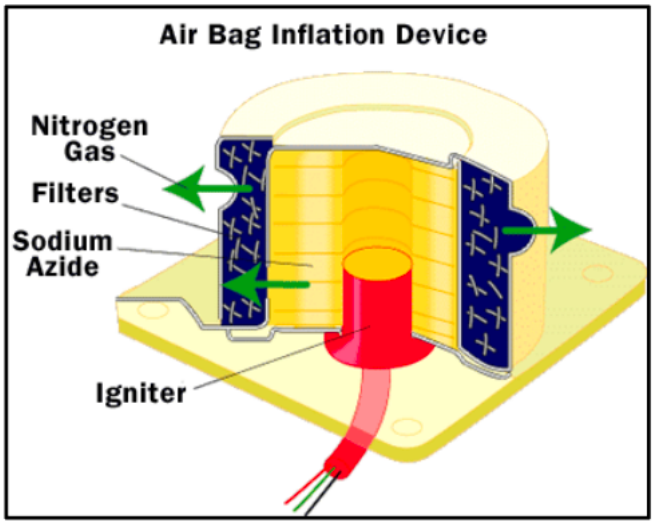

Figure 3.1 Gas Generator for airbag inflation [37]

3.3.2. Chemical Sublimates

This method uses solid materials that sublimate directly from a solid to a gas when exposed to void pressure conditions. The sublimation process generates the gas needed to inflate the structure.
Some examples of solid which can be used in this application are:

- Benzoic Acid: Sublimates at low pressures, providing controlled inflation. It has a favorable volume/mass ratio and is cost-effective.
- Ammonium Carbamate: Another common sublimating material used in similar applications.

Chemical sublimates eliminate the need for heavy gas storage tanks and leverages the space vacuum for efficient sublimation. The choice of sublimating materials is limited to those that are stable and non-toxic. [21][23]

Figure 3.2 Benzoic Acid Powder for inflation [37]

The following equation exploit the mass conversion rate due to sublimation [37]:

$$\frac{dm}{dt} = \alpha \sqrt{\frac{M}{2\pi RT}} \left(p_{eq} - p\right) \qquad (3.1)$$

Where:
α, represent a proportionality constant that is material specific
M, the molecular mass
R, the gas constant
T, the temperature
p, ambient pressure
p_{eq}, equilibrium vapor pressure dependent on temperature

This equation shows that the process tends to stop once ambient pressures approach the sublimates natural vapor pressure at that temperature.
p_{eq} is described by the following equation:

$$p_{eq} = \beta \sqrt{\frac{2\pi R}{M}} T e^{\frac{-\lambda}{RT}} \qquad (3.2)$$

Where β and λ are material specific constants. [37]

3.3.3. Electrostatic Inflation

This technique uses electrostatic forces to separate thin, flexible membranes coated with conductive materials, causing the structure to inflate. The electrostatic repulsion between the charged membranes creates the necessary pressure to inflate the structure.
An example of conductive material consists in Conductive Polymers. This inflation method is lightweight, does not require gas storage, and provides precise control over the inflation process.
Unfortunately, it requires a reliable power source and complex control systems to manage the electrostatic forces effectively.

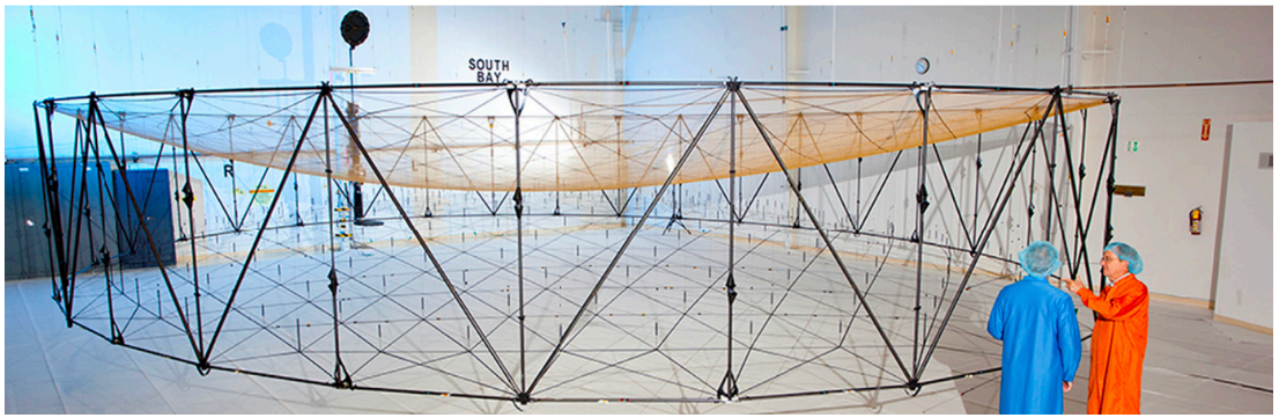

Figure 3.3 Electrostatic Controlled deployable membrane reflector by AstroMesh [42]

3.3.4. Chemical Inflation

It involves a chemical reaction which generates gas, inflating the structure. Practically, chemicals react to produce a gas which inflates the antenna.
Some examples of chemical agents are:

- Hydrogen Peroxide (H_2O_2): Decomposes into oxygen and water, generating gas for inflation.
- Sodium Azide (NaN_3): Used in automotive airbags, decomposes to produce nitrogen gas.

This technique provides a self-contained inflation system without the need for external gas sources. [28]

3.3.5. Mechanical Inflation

Mechanical means are used such as springs, elastic bands, or actuators to deploy the antenna. These mechanical elements expand and inflate the structure when released. Some of these elements follow:

- Springs and Elastic Bands: These components store potential energy that is released during deployment to inflate the structure.
- Actuators: Mechanical actuators can be used to push and pull components into place, inflating the antenna.

This method offers precise control over the deployment process and reduces reliance on external gas or chemicals. Though, it adds complexity to the design and may increase the overall weight of the system. [19,21,23]
Selecting the appropriate inflation technique for ultra-light inflatable antennas in LEO involves balancing simplicity, reliability, and efficiency. Each method has its advantages and challenges, and the choice depends on the specific requirements and constraints of the mission. Future research should continue to explore and refine these techniques to enhance the performance and durability of inflatable antennas in space.

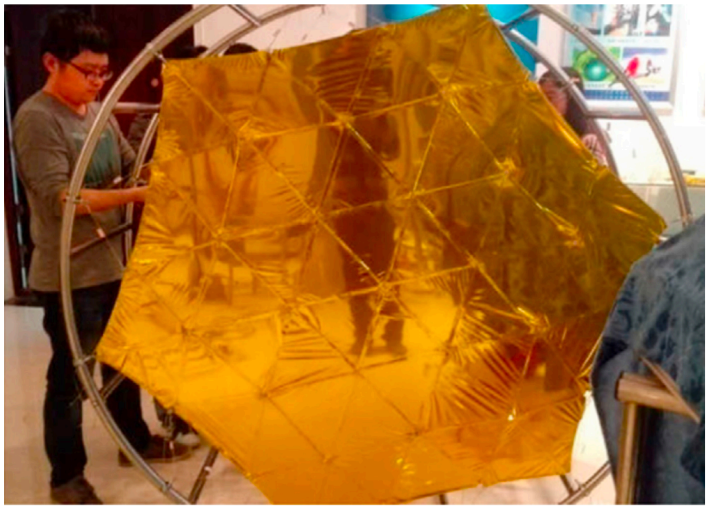

Figure 3.4 Cable based reflector [42]

3.4. Micrometeorites and space debris threats

The analysis of micrometeoroids and debris-related degradation is essential for developing more durable materials and ensuring the safety and longevity of spacecraft operating in the increasingly crowded space environment.
Over the last three decades, the number of satellites has dramatically increased the amount of debris in LEO, raising concerns about collisions that could damage spacecraft. Impacts with micrometeorites can cause a variety of malfunctions, such as degradation of solar cells, weakening of structural materials, and in worst scenario, the complete destruction of the antenna.
Space debris consists of hypervelocity fragments generated by satellite collisions, explosions, or disintegration, while naturally occurring micrometeoroids, traveling at ultrahigh velocities, also pose a serious risk.
Moreover, the penetration of micrometeoroid in our case of inflatable antenna, cause leaks that risks inflation gas losses and applies torque to the spacecraft. For the mentioned reasons and to increase the antenna's lifetime, it is advisable to apply rigidization techniques after the initial inflation. [25]

3.5. Rigidization techniques

This chapter provides a comprehensive overview of rigidization techniques for inflatable ultra-light antennas, as documented in the literature. In the subsequent chapter, a viable solution for rigidizing the antenna studied in this master thesis will be presented and thoroughly discussed.
As discussed briefly in previous chapters, purely inflated spacecraft are prone to issues such as wrinkling and gas leakage. However, the antenna structure must withstand the harsh conditions of the space environment while maintaining full functionality. Although the proposed inflatable ultra-large antenna design requires only low gas pressure, a rigidization method is essential for ensuring stability and sustainability during long-term missions.
Rigidization methods are closely linked to the materials chosen for the system's structure. As a result, some techniques may only be applicable when using specific layers of materials. Regardless of the chosen method, the key characteristics to prioritize include long storage life, low energy consumption, minimal outgassing, and ease of handling. [18]
These materials fall under a category known as "rigidizable materials", which are defined as materials that are initially flexible for inflation and deployment but become permanently rigid when subjected to external influences. [21]
The following sections describe several rigidization methods.

3.5.1. UV Rigidization

UV rigidization is a method where a layer of resin is applied, which is subsequently cured by ultraviolet (UV) radiation. The UV curing can be achieved using artificial lamps or solar radiation. Artificial UV sources offer better precision but require a power supply, making them less ideal for space missions where energy conservation is crucial. On the other hand, solar UV curing is a passive method that requires no power, though it is less precise due to inconsistencies in exposure. A key advantage of this technique is its low outgassing, which minimizes contamination risk in space environments, and the ability to store the material for extended periods without degradation. However, the main limitation lies in UV radiation's inability to uniformly penetrate all layers of certain structural materials, particularly those involving UV-opaque fibers such as graphite or polymers used in bladder layers. Additionally, UV rigidization is an irreversible process, complicating ground testing and reusability. This is not exactly a problem since the antenna is designed to a single deployment. [18][21].

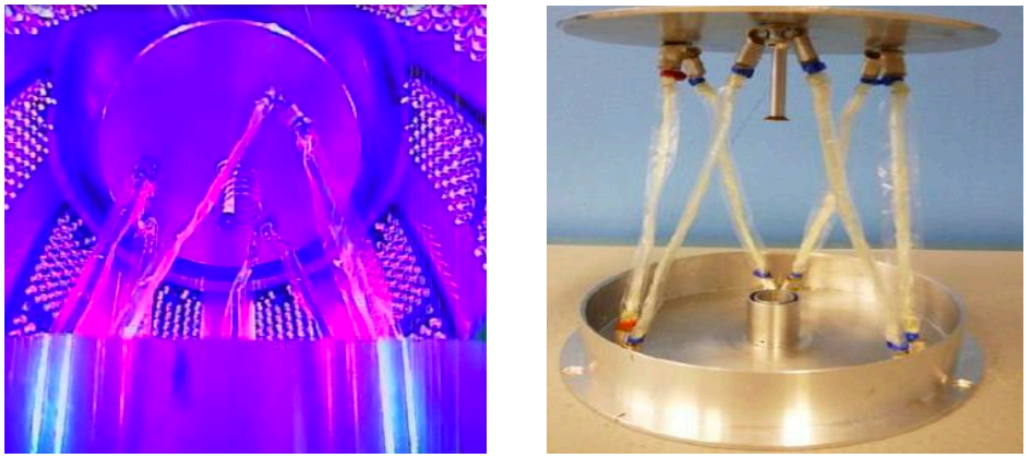

Figure 3.5 UV rigidized FOCUS mission sample [24]

3.5.2. Thermal Rigidization

Thermal rigidization uses heat to cure a resin-impregnated structure, typically utilizing thermosetting resins. The heat can come either from the sun (a passive method) or from an integrated heating system, which allows for more controlled and precise curing. After rigidization, the structure exhibits enhanced stiffness and strength, making this method particularly advantageous for load-bearing applications in space. It also benefits from low outgassing and a low thermal expansion coefficient, reducing structural deformation due to temperature changes. Unlike UV rigidization, this technique is compatible with a wider range of fibers used in space, including those that block UV light.
However, thermal rigidization poses challenges in terms of heat retention, although this can be mitigated with the use of multi-layer insulation blankets. The process is also irreversible, adding difficulty to handling and ground testing. [20] [21]

3.5.3. Glass Transition Rigidization

Glass transition rigidization leverages the phase change of polymers when temperatures drop below their glass transition temperature. Polymers contain both crystalline and amorphous regions; when the temperature falls below the glass transition point, the crystalline regions solidify while the amorphous ones remain flexible, resulting in a rubber-like material. Although structures rigidized through this method are not as stiff as those using thermosetting resins, they can still achieve sufficient rigidity for specific applications. [21] [24].

3.5.4. Stretched Metal Laminate Rigidization

This method involves laminating thin layers of ductile metal, such as aluminum, between polymer layers like Kapton or Mylar. Upon deployment, the internal pressure increases, causing the metal layer to exceed its yield stress while the polymer remains in its elastic region. This results in a pre-stressed configuration, where the metal is in compression and the polymer is in tension, stabilizing the structure. The key benefits of this method include low outgassing, long storage life, and the ability to predict the final rigidized state with high accuracy. However, the pre-stressed condition limits the structure's load-bearing capacity, restricting its use to applications that involve relatively low loads. This technique is interesting due to the low loads of our antenna. [20][24]

3.5.5. Gas and Vapor Curing Rigidization

Gas and vapor curing techniques gained attention in the 1960s for their potential in space inflatables. Various resins and catalysts have been tested, including water-curable resins and polyurethane systems rigidized by volatile peroxide vapors. One notable experiment involved polyurethane foam, which rigidized through a self-propagating reaction initiated by an aerosol-delivered catalyst. Despite these innovations, the method has fallen out of favor due to concerns over hazardous outgassing and difficulties in ensuring uniform catalyst penetration. Additionally, handling vapor-cured materials during ground operations can be challenging. [21]
Other techniques are available in the literature, but those presented above are the most relevant for this application.

3.6. Material selection

Materials suitable for aerospace application have a huge appeal for the main companies in the sector since the proper selection help reaching the mission goals, avoiding unexpected errors and failures. The material choice is fundamental and, as anticipated in the previous sections, the harsh environment to face in LEO lead to several implication in the antenna design.
The previous sections explained the material parameters that must be assessed to guarantee the antenna’s performance, durability, and longevity in LEO environment. Moreover, after deployment and initial inflation the antenna must be rigidized to overcome micrometeorites threats and increase the lifetime.
Accomplish all the requirements designing a multi-layer structure is particularly difficult because there are a lot of factors that must be considered at the same time. The following pages will introduce a method specifically elaborated for this innovative technology. Nevertheless, it is important to be aware that this feasibility study is a preliminary step. The following approach can be modified according to the final desired usage of the balloon. Indeed, it can be used as antennas, radio astronomy and eventually for transmission of solar power to earth.

The following choices will consider the examined ballon used as an antenna.

3.6.1. Overview of inflatable space antenna materials

Inflatable space antennas have been developed and tested in various missions, each employing specific material configurations to balance structural integrity, longevity and environmental protection. In general, it is advisable to use widely tested material because conducting specific test (such as vacuum ground test and dynamic test) is very complicated and expensive. According to this approach an overview of materials available in literature for large inflatable spacecraft will be briefly described.
Ultra-large inflatable antennas are stowed in a small volume and when the desired LEO orbit is reached, it starts the deployment phase. There are five methods for deploying which are inflation, inflation-rigidization, elastic ribs driven, shape memory polymer (SMP) and electrostatic forming. [26]

Inflation, it's a method which shows great advantages related to light weights and small stowage volumes. Though, a gas supplement system is required to cover eventual leakage, adding weight and making the structure susceptible to damages caused by micrometeorites.
This led to a short lifetime compared to other techniques.

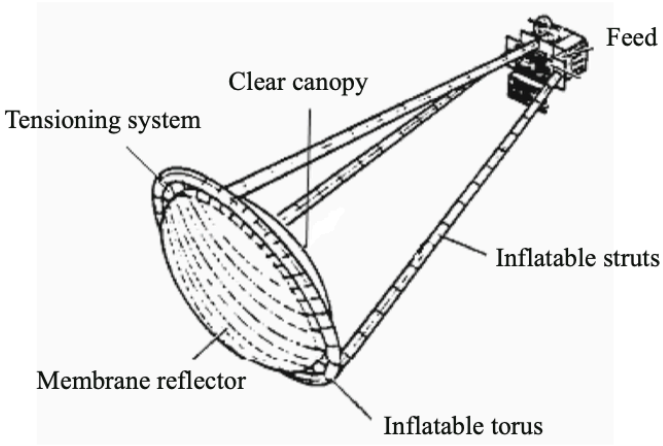

Figure 3.6 Membrane Inflated

Inflation-rigidization, after deployment the antenna's membrane is inflated and then rigidized with various available techniques. It maintains every advantage of the inflation method while avoiding many disadvantages like the presence of gas supplement system and micrometeorites threat. Nevertheless, selecting the proper rigidization technique according to the mission is a complex task.

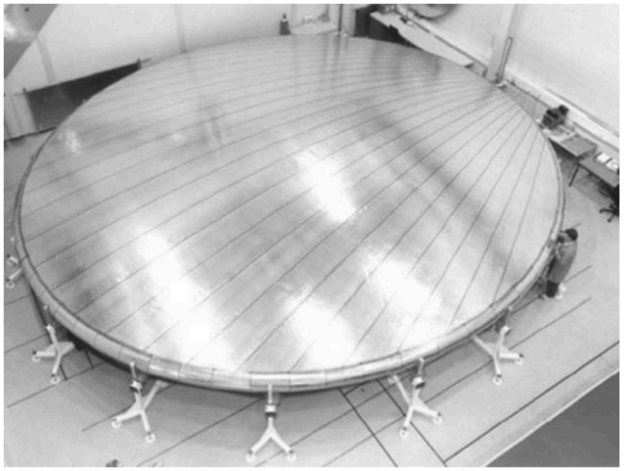

Figure 3.7 Contraves inflated-rigidized antenna [26]

Elastic Ribs Driven, during deployment elastic ribs are spiraled around a central hub and release their potential energy stretching out. Then hinges installed between elastic ribs and central hub drive the structure to open radially like an umbrella. The main advantage is the light weight, but there are several disadvantages of this technology: complex movements must be performed during deployment affecting the overall reliability, furthermore an improper folding method may easily cause critical damages to the membrane.

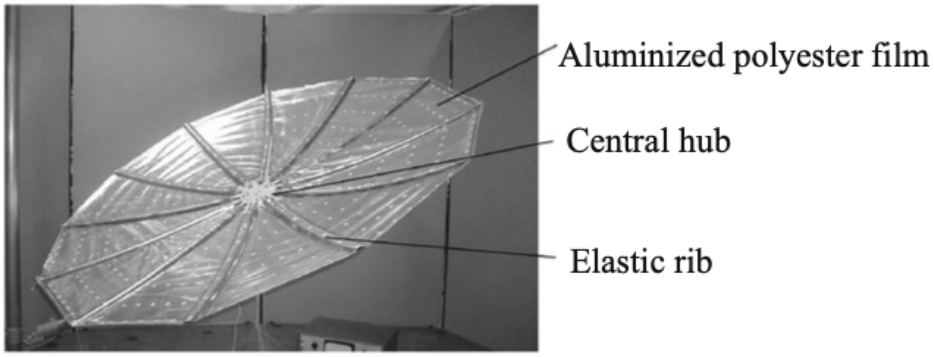

Figure 3.8 Elastic Ribs Driven antenna [26]

Shape memory polymer, the antenna is packed by an external load and the polymer is above the glass transition temperature. Then, keeping the external load and the temperature constant, the antenna maintains the shape. Once the selected orbit is reached the spacecraft is heated up above the glass transition temperature and it is inflated. Finally, the reflector returns to the initial shape and is rigidized after the temperature drops below the glass transition one. This method offers high reliability and strong surface accuracy, but the heating power required during deployment is high (around 70 kW for an antenna with a diameter of 35 m).

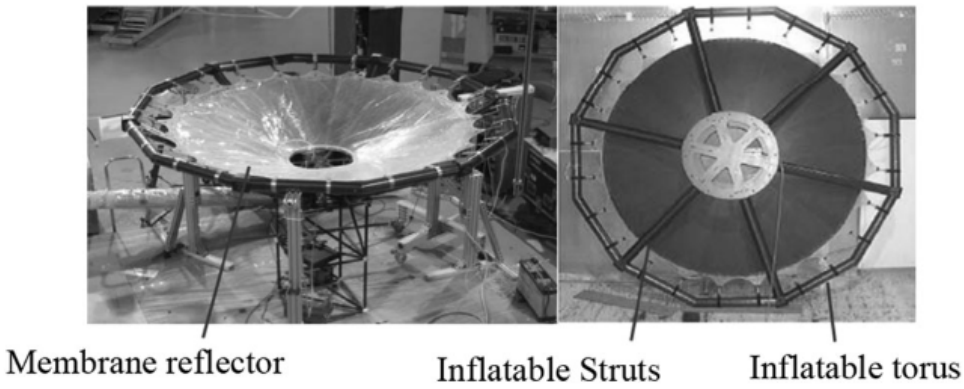

Figure 3.9 Shape Memory polymer membrane antenna [26]

Electrostatic forming, it is a recent technique which consist of creating an electric field using electrodes. So, the metal coated membrane becomes parabolic due to the electric field force.
Electrostatic forming membrane can theoretically be applied to large and high-precision antennas, but it is under development. High voltage applied can damage the electronic components on the spacecraft.

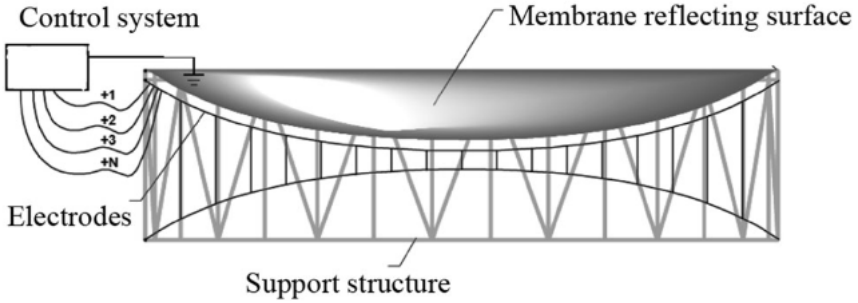

Figure 3.10 Electrostatic forming membrane antenna [26]

3.6.2. Comparative Analysis of Membrane materials

In this chapter will be discussed the chemical and mechanical requirements that a material must respect to accomplish the mission goal. The most important parameters are:
High thermal stability, high elasticity modulus, high shear strength, low density to reduce weights, small thickness, low thermal expansion coefficient and strong space radiation resistance.
Membrane material commonly used in this type of applications are polyester film (Mylar) and polyimide film (Kapton). The following table shows some commercial examples of these materials and their relative properties.

Table 3.1 Properties of different kind of membrane materials [26]

Property	Units	Mylar 48	Mylar 75	Mylar 92	Kapton 20EN	Kapton 50EN	UPilex-25S
Thickness	µm	12	19	32	5	12,5	25
Density	g/cm^3	1,40	1,38	1,39	1,42	1,42	1,47
Young Modulus	Gpa		3,79		5,0		9,1
Tensile Strenght	MPa	186 (MD)*	200 (MD)	187 (MD)	335	380	520
		234 (TD)*	244 (TD)	276 (TD)			
Thermal Expansion Coefficient	ppm/C°		17		16 (50-200°C)		12 (50-200°C)
Elongation at break	%	110 (MD)	130 (MD)	140 (MD)	55	62	42
		80 (TD)	100 (TD)	80 (TD)			
Anti-Ultraviolet radiation ability			Low			High	
Poisson's Ratio			0,38			0,34	

** MD= Machine direction; TD=Traverse Direction*

As show in table 3.1, kapton membrane exhibits superior mechanical strenght and flexibility, also it has an excellent thermal stability with lower Thermal Expansione Coefficients. Moreover it is inherently more resistant to UV Radiation, enhancing longevity in space environment. This charachteristic may be seen as a drawback if UV curing is selected as rigidization method. The structure will be rigidizide without an uniform process, because Kapton absorbs UV radiation.

These membranes are not highly reflective by themselves. To use these materials for the paraboloid reflector they must be coated with aluminum. After that they gain high reflectivity, which is crucial for reflecting and focusing electromagnetic waves. The Aluminum layer acts as a mirror for these waves, making aluminumized membrane an effective surface for gathering and reciting signals in ultra-large antennas.
Adding a thin layer to the Kapton or Mylar membrane doesn't significantly add mass which is optimal to reduce weights. Another reason to deposit this layer is to better withstand thermal variation in space, as the aluminum layer reflects solar radiation, helping to maintain a more stable temperature.
Moreover, considering the harsh space environment this upper layer provides a slight barrier against atomic oxygen degradation in LEO, although further protective coatings (like silicon dioxide) are often applied for full protection. Further detail about this will be exploited in next sections.
Considering the described properties of Mylar and Kapton, for this application an aluminized polyester film (Mylar 48) represents a better choice.

3.6.3. Protective Coatings

Spacecraft orbiting in LEO addresses atomic oxygen and extreme temperatures which lead to materials erosion and degradation. Furthermore, UV radiation has a negative impact on the durability. It is important to design the material layers according to these problems.
These threats may reduce the antenna lifetime or, in worst case scenario, critically compromise its functionality. So, a protective coating is compulsory to ensure the planned lifetime of the balloon.
Common protective coatings are:

- Silicon Dioxide (SiO_2):

  It provides excellent resistance to atomic oxygen, which is prevalent in LEO and can erode unprotected surfaces. Furthermore, its high UV shielding properties minimize degradation caused by prolonged exposure to solar radiation. It is often applied as a thin layer to avoid adding significant weight to lightweight structures. It has a density of 2,27 g/cm^3. [32]

- Aluminum Oxide (Al_2O_3):

  Provides robust resistance to atomic oxygen and UV radiation. Known for its high hardness, making it useful in applications where minor micrometeoroid impacts might occur. So, it is not the best choice for our case. [38]

3.6.4. Application Methods for Protective Coatings

There are two main techniques involved in thin material layer deposition:

- Physical Vapor Deposition (PVD):

PVD involves vaporizing the coating material in a vacuum environment and allowing it to condense onto the substrate, forming a thin and uniform layer. This method produces coatings with high purity and strong adhesion, essential for durability in space conditions. [27]

- Chemical Vapor Deposition (CVD):

CVD entails chemical reactions between gaseous precursors, resulting in the deposition of a solid material on the substrate. It can be produced high-quality, conformal coatings, even on complex geometries, ensuring comprehensive protection against Atomic Oxygen and UV radiation. [28]

3.6.5. Material configuration for the antenna

The following section proposes an optimized material configuration tailored to meet the demanding operational and environmental conditions of the antenna in LEO. This configuration address critical challenges as discussed, including atomic oxygen erosion, UV radiation, thermal cycling, and mechanical stability, while ensuring compatibility with inflation and rigidization techniques. The selected materials are designed to balance reflectivity, durability, and lightweight properties, making them ideal for the unique demands of space applications.
The antenna's structure consists of two parabolic hemispheres, the transparent canopy and the reflective section which are constructed with materials selected and optimized to ensure they effectively maintain their respective functionalities. The configuration selected for the Reflective Section is as follows:

Core Layer: Mylar to provide the primary structural integrity, stability and thermal resistance of this multi-layer for the reflective section.
Outer Core Layer: A thin layer of aluminum is present on Aluminized Mylar, exploiting the reflectivity function.
Outer Protective Coating: Silicon dioxide applied over the Aluminized Mylar surface to enhance resistance to atomic oxygen, UV radiation and micrometeoroids abrasion.

In a similar manner, the configuration adopted for the Non-Reflective Section (transparent canopy) is given below:

Inner layer: Mylar as transparent and structural resistance purpose. It also provides thermal resistance to the canopy.
Outer protective Coating: Silicon Dioxide has been also chosen for the canopy, which offers UV and atomic oxygen resistance for this section.

In the previous sections, it has been clarified that material must be chose according to inflation and Rigidization compatibility. This configuration of layers is suitable for Chemical sublimates inflation method.
Moreover, Thermal Rigidization and UV Rigidization techniques be used, as the materials are high compatible to both methods. The final choice between these suggested techniques depends on further studies and mission specific requirements.

In the following table, it will be explained the multi-layer thickness design, from the inner one to the outer:

Table 3.2 Material multi-layer with relative thickness

Reflective Section			Transparent Canopy		
Layer	**Material**	**Thickness**	**Layer**	**Material**	**Thickness**
Core Structural layer	Mylar	12,5 µm	**Core Structural layer**	Mylar	12,5 µm
Reflective Coating	Aluminum	200 nm	**Outer Protective Layer**	Silicon Dioxide	100 nm
Outer Protective Layer	Silicon Dioxide	100 nm			

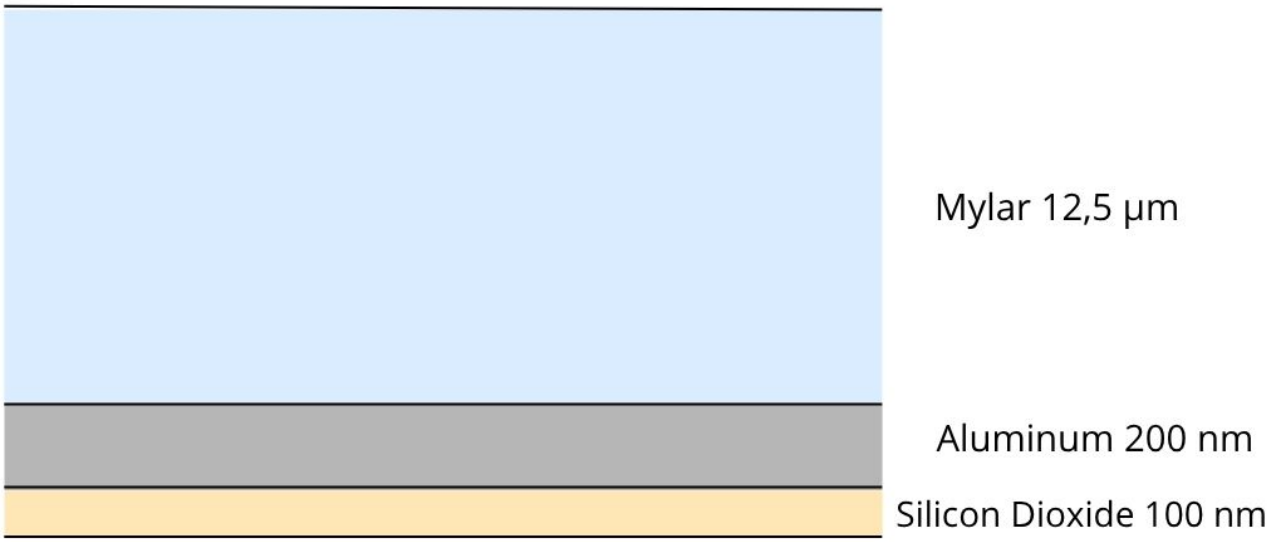

Figure 3.11 Material layers Reflective Section

Figure 3.12 Material layers Transparent Canopy

Depending on the mission requirements, a lighter multi-layer of materials can be chosen. Some of these parameters are structural integrity, thermal stability, manufacturing simplicity, and redundancy. A single layer configuration is presented in Table 3.2, right side.
This structure with aluminized Mylar and a silicon dioxide protective coating can be sufficient if weight minimization is critical, and the aluminized Mylar layer is engineered for adequate strength.

In conclusion, the chosen material configuration for the antenna's reflective section (comprising Aluminized Mylar, and a silicon dioxide protective coating) and transparent canopy (Mylar and silicone dioxide coating) has been carefully designed to ensure optimal performance in LEO. This multi-layer structure offers high reflectivity, exceptional thermal and mechanical stability, and robust protection against atomic oxygen, UV radiation, and micrometeoroid impacts.
To deploy this structure, gas inflation was chosen for its simplicity and reliability. This method is the most suitable according to the selected materials.
Following deployment, after the antenna reaches its final shape, the Rigidization process is applied using UV curing technique, a method that leverages the excellent thermal properties of Mylar. This process uses UV, potentially from solar exposure in LEO, to harden the structure, making it self-supporting and eliminating the need for continuous internal pressure. The rigidized antenna is robust enough to withstand thermal cycling, external stresses, and space debris impacts, ensuring long-term operational stability.
In the proposed configuration, the UV-curing resin should be inserted on the inner Mylar layer.
This strategic combination of advanced materials, chemical sublimates inflation, and UV rigidization delivers a lightweight, durable, and high-performing antenna. The approach aligns perfectly with the mission's objectives, ensuring reliability and efficiency in the demanding LEO environment.

Skin effects and its relevance to the Reflectivity of Aluminized Mylar
The applications in which the antenna can be implemented usually require a large size, high gain are mandatory for directional communication over long distances. For examples, mobile communication application operates at L-Band with frequencies of 1.5 GHz or Ka-band with 20/30 GHz, earth observation 6 – 20 GHz, microwave sensing 43 – 60 GHz.

The skin effect is a fundamental physical phenomenon observed in conductive materials subjected to alternating electromagnetic fields, particularly at high frequencies. Under such conditions, the induced current does not distribute uniformly throughout the conductor's volume. Instead, it becomes confined to a thin region near the surface, known as the skin layer. This behavior is caused by the exponential attenuation of the electromagnetic wave as it penetrates the conductor, resulting in a limited depth of penetration, commonly referred to as the skin depth. [39][40]

The skin depth "δ" is the characteristic distance over which the amplitude of the electromagnetic wave inside the conductor decays to approximately 37% (1/e) of its value at the surface. For good conductors such as the chosen aluminum for the reflective section of antenna, the skin depth can be calculated using the following expression:

$$\delta = \sqrt{\frac{\rho}{\pi * \mu * f}} \qquad (3.3)$$

where:

- δ is the skin depth [m]
- ρ is the conductor bulk resistivity in [Ohm-m]
- μ is magnetic permeability in [H/m]
- f is frequency in [Hz]

The relevance of skin depth in the design of reflective surfaces is critical. When using aluminum-coated membranes for inflatable space antennas, ensuring an adequate metal layer thickness is essential to achieving high electromagnetic reflectivity.

As supported in [39], if the thickness of the conductive layer is much greater than the skin depth, the material behaves almost like a perfect electric conductor (PEC), and nearly all the incident electromagnetic energy is reflected. Conversely, if the layer thickness is comparable to or less than the skin depth, a significant portion of the wave penetrates the material, leading to absorption and reduced reflection efficiency. The research was conducted on a 15 m reflector antenna operating at 1.5 GHz for mobile communications. The reflector surface was composed of Kevlar 49 composite of thickness 25 μm, a metal coating of aluminum and an indium tin oxide coating of thickness 0.006 μm.

The research demonstrated that the loss in gain is negligible if the thickness is greater than several hundred ˚ A. This is interesting since a thickness of several hundred ˚ A is much smaller than the skin depth of aluminum (2 μm at 1.4 GHz) and yet finite transmission is virtually nonexistent. For a thickness of 100 ˚ A, the loss in gain is about 0.1 dB, which may be important for some application.

As the frequency of the electromagnetic wave increases, the skin depth decreases accordingly.

Although the chosen aluminum layer thickness is only 200 nm and thus smaller than the corresponding skin depth at the operating frequency, the overall antenna efficiency remains effectively constant. This outcome is particularly significant, as it allows for a meaningful reduction in weight without compromising electromagnetic performance.

3.7. Stowage and Deployment

The technique used for folding the inflatable structures influences the deployment, so its choice and design are important aspects. It is needed to consider the available volume, the final shape and antenna's materials. Moreover, it is crucial to have a method to venting residual air.
The structure must have the flexibility to be folded many times, ensuring a safe controlled deployment. The following section will list an overview of the most used methodologies.

3.7.1. Coiling and Wrapping

This approach involves flattening the inflatable structure and rolling it around a central hub to form a compact coil. In the 'coiled' configuration (Figure 3.13 on the left), inflation gas is introduced from the open end of the coil, causing it to unfurl progressively. In the 'wrapped' configuration (Figure 3.13 on the right), gas is supplied through the central hub, leading the inflatable to unwrap during deployment. This method is particularly well-suited for deploying long, slender structures such as booms and trusses. Both methods present some issues regarding deployment stability. Nevertheless, angular velocity must be externally controlled in coiling technique to avoid critical damages. [15]

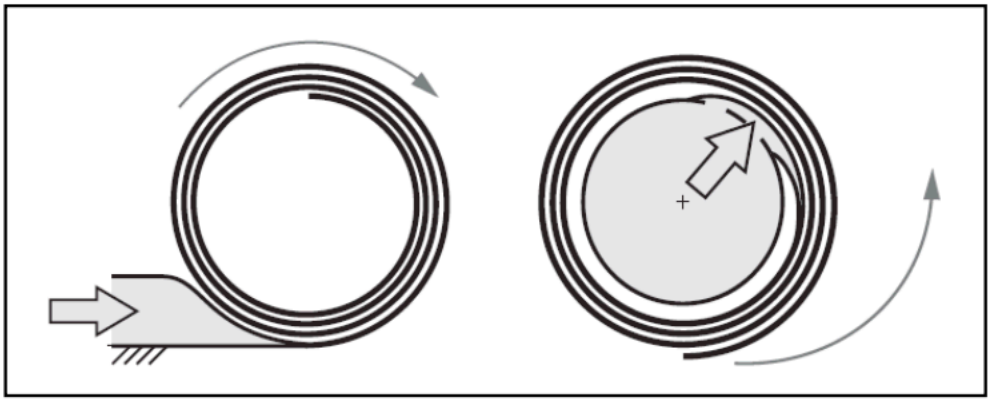

Figure 3.13 Inflatable coiling (left) and wrapping (right) techniques [15]

3.7.2. Z-folding

The z-folding technique involves folding the flattened inflatable structure back and forth along lines perpendicular to its longitudinal axis, creating a zigzag pattern. Each fold acts as a hinge, enabling the structure to unfold during deployment. As illustrated in Figure 3.14, this method has been used in notable experiments such as the deployment of 28-meter-long booms during the Inflatable Antenna Experiment (IAE).
While z-folding is straightforward and has the advantage of minimal air entrapment, it has some significant limitations. Studies and experimental results suggest that the method suffers from inherent instability during deployment, leading to uncontrolled inflation dynamics. Additionally, it offers lower packing efficiency compared to other techniques, making it less suitable for applications requiring compact stowage. Despite these drawbacks, its simplicity and history of successful use in space applications give it some practical relevance. [17]

Figure 3.14 IAE experiment, inflation and deployment of a z-folded antenna [17]

3.7.3. Origami Folding

The Origami folding technique leverage repeated parallel folds arranged in specific origami patterns to achieve compact stowage of inflatable structures. These patterns enable individual membrane segments to locally buckle into the stowed configuration, minimizing the overall volume. Upon inflation, the localized stiffening of the membrane segments facilitates self-deployment, reducing the need for complex mechanical systems.
This method shows significant potential for creating mechanically simple and space-efficient deployment mechanisms, without any important drawback. Studies by Tsunoda et al. [29] and Senda et al. [30] have extensively analyzed the structural behavior and feasibility of origami patterns, demonstrating their effectiveness in real-world applications.

Figure 3.15 illustrates fundamental origami folding patterns, showcasing their adaptability for compact stowage and controlled deployment in space environments.

Figure 3.15 Origami folding according to different patterns [15]

To ensure deployment stability and packing efficiency, it is advisable to use Origami folding for this ultra-light inflatable antenna.

4. Antenna preliminary design

Respect to Echo balloons launched almost 60 years ago, this kind of spacecraft is designed to operate as an antenna. To reach this objective, a metallic coating will be applied to just part of a sphere: in this way a large reflecting surface will be obtained. However, the main problem encountered is the method used to orient the object if it must act as antenna. Indeed, the extreme thickness of the walls and their extremely large dimensions imposes to exercise a diffuse, weak but regular force to slowly orient the antenna in the chose direction, avoiding the introduction of deformations and wrinkles.
In the following sections, an innovative technique for re-orienting the balloon in a chosen direction will be suggested. This is a preliminary feasibility study, so advanced further studies will be required to assess every aspect.
The new parabolic antenna has a diameter, D, of 30 m and has 3 copper rings or strip used to orient the antenna to the target.
The parabola can be described by two parameters, the diameter D and the focal length F. Moreover, two auxiliary parameters are also defined, the vertical height of the reflector section (H) and the max angle between the focal point and the edge of the dish (θ_0). These parameters are related to each other by the following equations:

$$\frac{F}{D} = \frac{1}{4\tan\frac{\theta_0}{2}} \qquad (4.1)$$

$$F = \frac{D^2}{16H} \qquad (4.2)$$

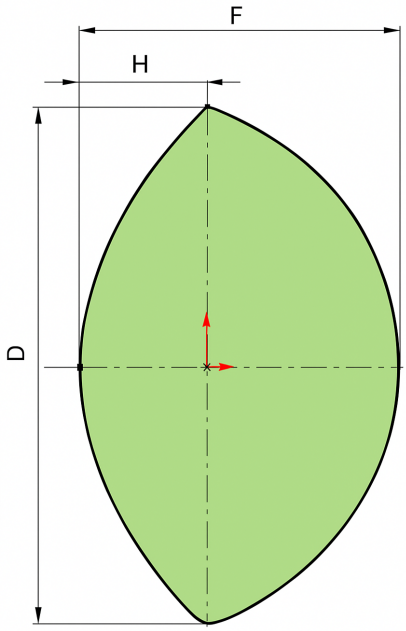

Figure 4.1 Parabola design

For design, the value of the diameter D should be increased to increase the gain of the antenna. The focal length F is then the only free parameter; typical values are commonly given as the ratio F/D, which usually range between 0.3 and 1.0.

For this purpose, two cases will be considered with two F/D ratio, 0.38 and 1.00.

4.1. First case F/D 0.38

In the first case, it has been selected a F/D ratio of 0.38. With the parabolic antenna diameter equal to 30 m the focal distance is computed as follows:

$$F = \frac{F}{D} * D = 0.38 * 30 = 11.4 \text{ m}$$

While the reflector vertical height is equal to:

$$H = \frac{D^2}{16F} = \frac{30^2}{16 \cdot 11.4} = 4.93 \text{ m}$$

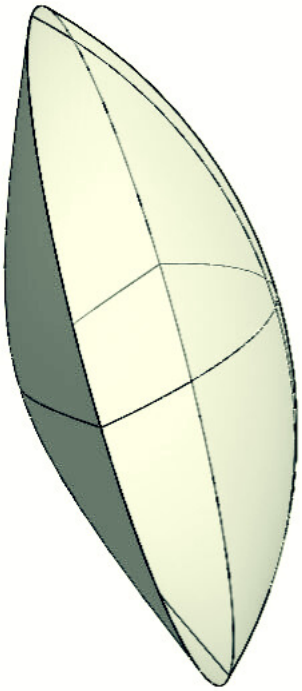

Figure 4.2 Layout parable first case

Using SolidWorks and assuming a layer thickness of 12.8 μm for the reflector and 12.6 μm for the transparent canopy, it is possible to compute the structural volume $V_{Structural}$, the total volume V_{Tot}, and the total surface S_{Tot} as follows:

$$V_{structural_{refl.}} = 0.00975 \text{ m}^3$$
$$V_{structural_{canopy}} = 0.01055 \text{ m}^3$$

So, the total Volume of the structure is computed: $V_{structural} = 0.020\ m^3$

$$V_{Tot} = 4029{,}41 \text{ m}^3$$
$$S_{Tot} = 1600.09 \text{ m}^2$$

Where V_{Tot} is the total volume occupied by the antenna once it reaches its final shape, S_{Tot} is the total lateral surface in the same condition. [31]
Assuming the layer distribution as described in previous chapters, the density for each section of the antenna follows:

$$\rho_{reflector} = \frac{s_{mylar}\rho_{mylar} + s_{aluminum}\rho_{aluminum} + s_{SiO2}\rho_{SiO2}}{s_{tot}} = 1427\ \mathrm{kg/m^3}$$

$$\rho_{canopy} = \frac{s_{mylar}\rho_{mylar} + s_{SiO2}\rho_{SiO2}}{s_{tot}} = 1407\ \mathrm{kg/m^3}$$

Where:

- s is the layer thickness in μm
- ρ is the density in $\mathrm{kg/m^3}$ and $\rho_{reflector}$ and ρ_{canopy} are equivalent structure density.

According to the material selection and the thickness of each layer, the structure weight is equals:

$$M_{structure} = \rho_{reflector}V_{structural_{refl.}} + \rho_{canopy}V_{structural_{canopy}} = 28{,}75\ \mathrm{Kg}$$

In Figure 2, it is visible that there are 1 circular ring, orthogonal to the antenna axis, with a diameter $D_{z_{ring}}$ of 30 m and two rings, coaxial with the antenna's axis, that follow the antenna's shape. For the first ring the surface, $S_{z_{ring}}$, is equal to:

$$S_{z_{ring}} = \frac{\pi D_{z_{ring}}^{\ 2}}{4} = \frac{30^2\pi}{4} = 706.86\ \mathrm{m^2}$$

And the total length is equal to:

$$l_{z_{ring}} = \pi D_{z_{ring}} = 30\pi = 94.25\ \mathrm{m}$$

The last two rings are computed with the CAD program:

$$S_{x_{ring}} = S_{y_{ring}} = 223.06\ \mathrm{m^2}$$
$$l_{x_{ring}} = l_{y_{ring}} = 65.36\ \mathrm{m}$$

Each ring, (alternatively the ring may be implemented with a copper strip 10 cm wide and 0.01 mm thick with the same weight), has an area, A_{Cu}, of 1 $\mathrm{mm^2}$ and with a density, ρ_{Cu}, of 8960 $\mathrm{kg/m^3}$ the 3 rings have a total weight of:

$$M_{rings} = M_{x_{ring}} + M_{y_{ring}} + M_{z_{ring}} = \rho_{Cu}\left(V_{x_{ring}} + V_{y_{ring}} + V_{z_{ring}}\right)$$
$$= \rho_{Cu}\left(A_{Cu}l_{x_{ring}} + A_{Cu}l_{y_{ring}} + A_{Cu}l_{z_{ring}}\right) = 2.02\ \mathrm{kg}$$

Ring's resistor is computed with the follow equation:

$$R_{ring} = \frac{\rho_{Cu} l}{A}$$

Where ρ_{Cu} is the conductor resistivity, l is the length and A is the conductor area.
For the circular ring orthogonal to the antenna axis:

$$R_{z_{ring}} = \frac{\rho_{Cu} l_{z_{ring}}}{A_{cu}} = \frac{1.68 * 10^{-8} * \pi * 30}{1 * 10^{-6}} = 1.58\ \Omega$$

Where $A_{cu} = 10^{-6}\ m^2$, $\rho_{Cu} = 1.68 \cdot 10^{-8}\ \Omega m$ at 293.15 K and $l = \pi D = \pi * 30$ m.
For the other rings, the resistivity is equal to:

$$R_{x_{ring}} = R_{y_{ring}} = \frac{\rho_{Cu} l_{x_{ring}}}{A_{cu}} = \frac{1.68 * 10^{-8} * 65.36}{1 * 10^{-6}} = 1.10\ \Omega$$

The total antenna weight, rings and structure, is about $28{,}75 + 2{,}02 = 30{,}77$ kg. With a static safety factor, SF_s, of 2, due to the early design phase, in the following chapter it will be considered a total mass of 70 kg.
With the total weight, the principle inertial moments can be computed:

$$I_x = I_y = 4677\ kgm^2$$
$$I_z = 8112\ kgm^2$$

4.2. Second case F/D 1

In the second case, it has been selected a ratio F/D of 1. With the parabolic antennas diameter equal to 30 m the focal distance is:

$$F = \frac{F}{D} D = 1 * 30 = 30\ m$$
$$H = \frac{D^2}{16F} = \frac{30^2}{16 \cdot 11.4} = 1.875\ m$$

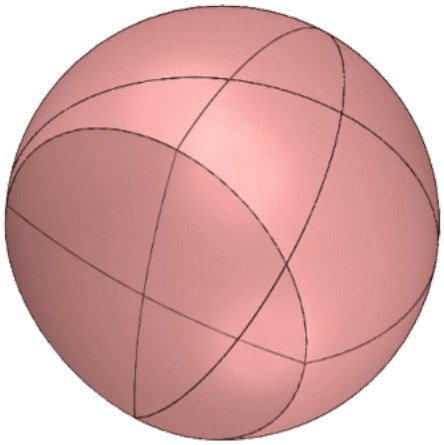

Figure 4.3 Layout parable second case

With the same layer thickness used in the previous antenna's design, it is possible to compute the following parameters:

$$V_{structural_{refl.}} = 0.00918\ m^3$$
$$V_{structural_{canopy}} = 0.04\ m^3$$

So, the total Volume of the structure is computed: $V_{structural} = 0.049\ m^3$

$$V_{Tot} = 10602{,}88\ m^3$$
$$S_{Tot} = 3910{,}00\ m^2$$

The structure weight is equals to:

$$M_{structure} = \rho_{reflector} V_{structural_{refl.}} + \rho_{canopy} V_{structural_{canopy}} = 69{,}37\ Kg$$

The ring on the z axis have the same properties in both cases:

$$S_{z_{ring}} = \frac{\pi D_{z_{ring}}{}^2}{4} = \frac{30^2\pi}{4} = 706.86\ m^2$$
$$l_{z_{ring}} = \pi D_{z_{ring}} = 30\pi = 94.25\ m$$
$$R_{z_{ring}} = 1.58\ \Omega$$

While the other two rings in this case have the following properties:

$$S_{x_{ring}} = S_{y_{ring}} = 893.69\ m^2$$
$$l_{x_{ring}} = l_{y_{ring}} = 108.37\ m$$

$$R_{x_{ring}} = R_{y_{ring}} = \frac{\rho_{Cu} l_{x_{ring}}}{A_{cu}} = \frac{1.68 * 10^{-8} * 108.37}{1 * 10^{-6}} = 1.82\ \Omega$$

Each ring has an area, A_{Cu}, of 1 mm^2 and with a density, ρ_{Cu}, of 8960 kg/m^3 the 3 rings have a total weight of:

$$M_{rings} = A_{Cu}\rho_{Cu}\left(2l_{x_{ring}} + l_{z_{ring}}\right) = 1 * 10^{-6} * 8960(2 * 108.37 + 94.25) = 2.79\ kg$$

For the second case the total antenna weight, rings and structure weight, is about $69{,}37 + 2{,}79 = 72{,}16$ kg. With a safety factor, SF, of 2, due to the early design phase, in the following chapter will be considered a total Mass of 150 kg.
With the total weight, the principle inertial moments can be computed:

$$I_x = I_y = 29293\ kgm^2$$
$$I_z = 30405\ kgm^2$$

4.3. Layout compare

In Table 4.1 are summarized the properties evaluated before. It can be noticed that the first configuration has less weight, volume and ring resistor than the second cases. For this reason, the forces required to rotate the antenna are smaller than the second case, with the same power the current on the ring is bigger and with the same area the magnetic torque is bigger. Though, at the same time with the same current, the second case is better due to bigger axial ring surfaces.

Table 4.1 Comparison between layout 1 and layout 2

	Layout 1	***Layout 2***
Total weight [kg]	70	150
Total volume [m^3]	4029,41	10602,88
Total surface [m^2]	1600,09	3910,00
R ring [Ω]	1,10	1,82
Ring surface [m^2]	223,06	893,69
Max inertial moment [kgm^2]	8112	30405

To reduce the satellite weight, volume and power consumption the first solution is the best choice to reduce the mission cost and deployments system complexity.

5. Orbit Environment and Its Impact on Inflatable Antenna Design

5.1. Preliminar orbit design

To fulfill all mission's requirement the orbit will be selected have the following boundary:

- The perigee and apogee altitude must be less than 35000 km, to satisfy magnetic field model validity region
- The mission lifetime must be more than 6 months
- Short eclipse period to reduce battery's volume and weight
- Reduce space debris impact risk; to satisfy this requirement we choose an orbit with perigee more than 2000 km height
- Reduce orbit perturbation to reduce the fuel mass or delete the orbit maintainability system, this is possible for small satellite and with a lifetime of few years

From the previous requirements, 10 possible orbit solution have been selected and are shown in table 5.1. The inclination i is the same of Hubble telescope orbit [4].

Table 5.1 Orbits Overview

Case	$h_a\ [km]$	$h_p[km]$	$i\ [deg]$	$a\ [km]$	e	$\tau[s]$
1	2000	2000	28.5	8378.4	0.000	7632.234
2	2000	5000	28.5	9878.4	0.152	9771.024
3	5000	5000	28.5	11378.39	0.000	12079.031
4	2000	10000	28.5	12378.4	0.323	13705.886
5	2000	20000	28.5	17378.4	0.518	22799.494
6	2000	35000	28.5	24878.4	0.663	39052.095
7	35000	5000	28.5	26378.4	0.569	42636.678
8	35000	10000	28.5	28878.4	0.433	48839.409
9	35000	20000	28.5	33878.4	0.221	62057.616
10	35000	35000	28.5	41378.4	0.000	83766.686

Where:

- h_a is Perigee, the closest point of the satellite to the Earth during its orbit.
- h_p is Apogee, the farthest point of the satellite form Earth during its orbit.
- i is Inclination, angle between the orbital plane and the Earth's equator, assumed equal to Hubble telescope.
- a is Semi-major Axis, the average distance from the center of the Earth to the satellite, which define the size of the orbit.
- e is Eccentricity, describes how elliptical an orbit is.
- τ is Orbital Period, the time it takes for the satellite to complete one orbit.

Using AGI's STK software, the satellite's orbital propagation it has been simulated over the time span from January 1, 2021, to December 31, 2021. The results of this analysis are presented in Table 5.2, which reports the satellite's time spent in eclipse and sunlight throughout the orbital periods over the year. From the data, it can be observed that increasing the semi-major axis leads to a reduction in the ratio between eclipse time and orbital period. This implies that selecting orbits with a smaller semi-major axis helps minimize the eclipse duration—an important factor in reducing or eliminating battery usage. Additionally, a lower orbit reduces the orbital day duration, which contributes to

minimizing orbital perturbations, fuel consumption, and the probability of collision with space debris, due to both a lower debris density and reduced relative velocity between the satellite and surrounding objects. [5]

However, opting for a highly elliptical orbit with a large semi-major axis shortens the satellite's residence time near perigee, where the Earth's magnetic field is stronger. This also extends the natural deorbiting period, thereby making the use of thrusters necessary for a timely and controlled deorbiting maneuver.

Table 5.2 Overview of Orbits eclipse and sunlight period

CASE	$\tau_{eclips}[s]$			$\tau_{sunlight}[s]$			$\frac{\tau_{eclipse}}{\tau}$ [%]
	Min	**Max**	**Mean**	**Max**	**Min**	**Mean**	
1	82.768	2110.746	1865.456	7549.466	5521.488	5766.778	24.44%
2	124.900	2712.261	1867.840	9646.124	7058.763	7903.184	19.12%
3	135.878	3535.391	1986.852	11943.153	8543.640	10092.179	16.45%
4	34.600	3307.674	2393.219	13671.286	10398.212	11312.667	17.46%
5	30.491	4764.560	2518.560	22769.003	18034.934	20280.934	11.05%
6	432.109	5307.051	2664.988	38619.986	33745.044	36387.107	6.82%
7	909.803	5779.769	3047.162	41726.875	36856.909	39589.516	7.15%
8	1069.574	5512.690	3319.663	47769.835	43326.719	45519.746	6.80%
9	1236.742	4817.426	3572.869	60820.874	57240.190	58484.747	5.76%
10	1579.244	4995.720	3856.598	82187.442	78770.966	79910.088	4.60%

In Table 5.3, are show the magnetic field magnitude that the satellite sees in its orbit trajectory. From the table, it can be noticed that the magnetic field decrease with the apogee altitude. For this reason, it is important to reduce the apogee altitude to reduce the electric power consumption and reduce the electronic systems weight and size. From an altitude of 2000 km to 35000 km the magnetic field module became 100 times less that follow that the current to control the spacecraft asset will be 100 times bigger that the current used at 2000 km. Another consideration is that at the apogee the angular acceleration is 100 times less and is possible to increase the precision of the antennas pointing direction. [8]

Table 5.3 Orbits magnetic field magnitude

CASE	**B [nT]**		
	Min	**Max**	**Mean**
1	10764.34	23382.46	15823.00
2	4520.17	43525.44	13370.93
3	4518.62	8801.06	6196.76
4	1579.28	23350.50	5712.16
5	392.95	23335.77	2792.02
6	104.24	19782.38	1431.14
7	104.22	7457.03	889.51
8	104.23	2251.78	510.52
9	104.18	498.50	248.72
10	104.18	163.44	126.57

In conclusion, to reduce the maneuver time and reduce the satellite weight the 2nd option has been chosen, with the following characteristics:

- $h_a = 2000$ km
- $h_b = 5000$ km
- $a = 9878.4$ km
- $e = 0.152$
- $\tau = 9771.024$ s
- $\tau_{eclipse} = 1867.840$ s
- $\tau_{sunlight} = 7903.184$ s
- $B_{max} = 43525.44$ nT

5.2. Magnetic field model

The Earth's magnetic field can be approximated as that of a magnetic dipole, currently tilted by approximately 11 degrees with respect to the planet's rotational axis. This field extends from the Earth's interior outward into space, where it interacts with the solar wind. At any given point, the magnetic field is represented as a three-dimensional vector. Its horizontal angle with respect to true north is known as the declination (D). When facing magnetic north, the angle that the field vector forms with the horizontal plane is called the inclination (I). The intensity of the magnetic field, denoted as B, is directly proportional to the force it exerts on a magnetic object.

The International Association of Geomagnetism and Aeronomy (IAGA) maintains a standard global model of Earth's magnetic field called the International Geomagnetic Reference Field (IGRF). The 11th-generation model (IGRF11), valid until the year 2000, was based on a spherical harmonic expansion truncated at degree 10 (120 coefficients). More recent versions are truncated at degree 13, involving 195 coefficients, to allow for higher resolution. The geomagnetic field is modeled mathematically by the following expansion:

$$B(r,\theta,\phi,t) = a\sum_{n=1}^{N}\sum_{m=0}^{n}\left(\frac{a}{r}\right)^{n+1}[g_n^m(t)\cos(m\phi) + h_n^m(t)\sin(m\phi)]P_n^m(\cos\theta) \qquad (5.1)$$

with r denoting the radial distance from the center of the Earth, $a = 6371.2$ km being the Earth's mean reference spherical radius conventionally used in geomagnetic modelling, θ denoting geocentric co-latitude, and φ denoting east longitude. The functions $P_n^m(\cos\theta)$ are the Schmidt quasi-normalized associated Legendre functions of degree n and order m. The Gauss coefficients g_n^m, h_n^m are functions of time t and are conventionally given in units of nano-Tesla (nT). The IGRF model is particularly useful for the analysis of historical geomagnetic data, as it spans from the year 1900 up to the present. Unlike the World Magnetic Model (WMM) -which is optimized for short-term navigation- the IGRF is updated every five years to reflect the latest geomagnetic observations. The current 13th edition, released in December 2019, is valid from 1900 to 2025. For the interval between 1945 and 2015, the model is considered "definitive", meaning that future updates are unlikely to bring significant changes.

The Earth's magnetic field varies as a function of the satellite's distance from the Earth's center (r), longitude (ϕ), latitude (θ), and time (t). In this model, the standard radius a is 6371.2 km, and the spherical harmonic expansion is truncated at degree N = 13. For this analysis, the IGRF model is

applied within an altitude range from –1000 m to 5.6 Earth radii. The following table presents the results for a polar circular orbit with an inclination of 90 degrees, simulated for early 2024. The magnetic field values were computed using the IGRF model implemented in MATLAB. This orbital configuration corresponds to a satellite path passing over both poles along a trajectory perpendicular to the equatorial plane. The variation in the magnetic field experienced by the satellite at different altitudes is summarized below.

Table 5.4 Mean, Max and Min value of B at different height depending on Latitude, Longitude of 0°

Latitude [deg]	B [NT] AT 500 KM	B [NT] AT 2000 KM	B [NT] AT 10000 KM	B [NT] AT 35000 KM
Max (near Poles)	46296	26416	3588.10	219.0654
Min (near equator)	20627	12384	1634.80	105.4564
Mean	31304	17833	2547.40	163.5648

From Table 5.4 it is visible that the $\vec{B}$ module decreases with height and from Pole to equator.

5.3. Influence of orbit environment parameters on balloon design

Here are some important parameters to consider when evaluating the orbit environment for an inflatable antenna:

Pressure and Micrometeoroids
Space is a near-vacuum environment. This means there is very little pressure to counteract the internal pressure of the inflatable antenna. The antenna will need to be designed to withstand the internal pressure differential without collapsing or bursting. Micrometeoroids are tiny particles of dust and rock orbiting the Sun. They can collide with the antenna and potentially puncture its skin. The size and frequency of micrometeoroid impacts depend on the specific orbit. Higher orbit will generally have fewer micrometeoroid impacts, but they can still be a threat.

Temperature
Spacecrafts in LEO experience large temperature swings as they pass from sunlight to eclipse phase. This can cause the antenna material to expand and contract, which could stress the structure and lead to tears or leaks. Materials with low coefficients of thermal expansion are preferred.

Radiation
Exposure to solar radiation can degrade the antenna's materials over time. The specific type of radiation and its intensity will depend on the orbit. Higher orbits will receive more intense solar radiation. High-energy particles from the Sun and other sources can also damage the antenna's electronics and control systems.

Orbital Mechanics and Perturbations
As mentioned previously, the pressure, micrometeoroid risk, and radiation levels all vary depending on the altitude of the orbit. LEO offers some advantages in terms of deployment and communication distance but comes with harsher environmental conditions. The angle of the orbit relative to the equator can affect the amount of solar radiation received by the antenna.
Even at LEO, there is a residual atmosphere that can cause drag on the antenna. This drag can affect the orbit of the antenna over time and may require occasional maneuvers to maintain its position.

Spacecraft Self-emissions

Some materials used in spacecraft construction can outgas, releasing contaminants that could condense on the antenna's surface and potentially affect its performance. So, materials with low outgassing rates are preferred.

6. Simulation and Model Results

In the present chapter will be discussed the relationship between the applied current and the maneuver time. It's crucial to correctly choose the current value applied to the conductor ring to have a proper maneuver time, while controlling power consumption. The following analysis have been conducted solving the dynamic equation for the antenna through Matlab scripts.
Each of the following cases have the following assumption: on the satellite is acting only the magnetic torque.

6.1. Apply a constant current *i* for all maneuver time

This analysis has been conducted to compute the time necessary to reach the 0 deg position of the antenna (normal vector parallel to magnetic field vector) evaluating different initial angles at constant current. The rotation verse is clockwise as showed in figure 6.1. Moreover, these variables have been studied at different magnetic field strength, where the minimum and maximum are respectively Low latitude and High latitude values.

The system parameters used for this evaluation are:

- Magnetic field strength "B", linearly spaced between 12.384 μT (equator) and 26.416 μT (near Poles), at 2000 km altitude form sea level.
- $S_{z_{ring}} = 706.86\ m^2$, surface of the ring orthogonal respect to the antenna axis in the I type of geometry (deeply discussed in next chapters).
- $I = 8112\ Kg\ m^2$, moment of inertia of antenna in I type of geometry
- Initial Angles $= [10, 20, 30, 45, 60, 80, 90]$
- Current $= 1$ A, current flowing in the conductor ring

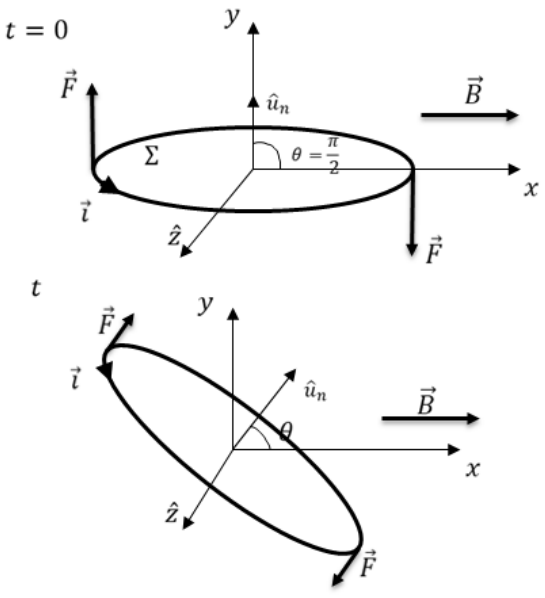

Figure 6.1 Initial pose of satellite θ=90° (upper), clock verse rotation (down) [9]

The following result has been obtained solving, through numerical integration, the nonlinear second order differential equation of the satellite dynamic:

$$\ddot{\theta} = \frac{-i\, S_{z_{ring}} \mathrm{B}\, \sin\theta}{I} \qquad (6.1)$$

In the fig. 6.2 it is showed the result of the analysis. At low latitude, near equator, where the B module is lower the maneuver time needed to a total rotation is higher than 25 min for little rotation and higher than 29 min with a 90 deg rotation. At highest latitude, near Poles, the $\vec{B}$ module is bigger, and the rotational time is under 18 min for little degree, while for a 90-degree rotation the total time is about 20 min. Applying the same current over time, the satellite oscillates at the equilibrium angle of 0 deg due to inertia.

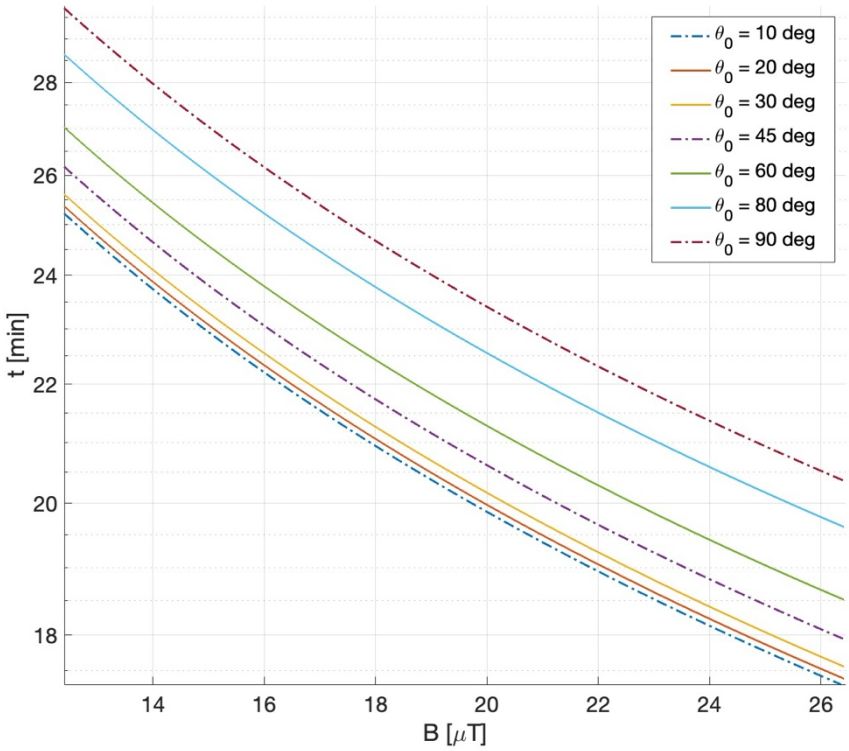

Figure 6.2 Time to align normal vector at B at different starting θ applying a constant current

6.1.1. Effect of current increase

This second analysis has been conducted to calculate the time necessary to reach the 0 deg position of the satellite (normal vector parallel to magnetic field vector) evaluating different current values starting from an initial angle of 90 deg. Moreover, these variables have been studied at different magnetic field strength, where the minimum and maximum are respectively Low latitude and High latitude values.
The system parameters used for this evaluation are:

- Magnetic field strength "B", linearly spaced between 12.384 μT (equator) and 26.416 μT (near Poles), at 2000 km altitude form sea level.
- $S_{z_{ring}} = 706.86\ m^2$, surface of the ring orthogonal respect to the antenna axis in the I type of geometry (deeply discussed in next chapters).
- $I = 8112\ Kg\ m^2$, moment of inertia of antenna in I type of geometry
- Initial Angle = 90 deg
- Current values = [0.1, 1.0, 5.0, 10.0, 50.0, 100.0] A, current flowing in the conductor ring

From this initial position, the satellite rotation verse is clockwise.
In **Errore. L'origine riferimento non è stata trovata.**.3, it is showed that applying a current of 0.1 A the time to reach 0 degree from 90 degree is up to 81 minutes at low latitude and 56 minutes near the poles, while with a current of 10.0 A is reduced by 95% compared to the previous case. Indeed, in this second current value, the time required is respectively 8 and 6 minutes. Applying a current of 1 A, the same results are obtained, particularly 26 min (low latitude) and 18 min (high latitude).
While with a current of 100.0 A the time to complete a rotation fell to few minutes. The last case was the best to reduce the maneuver time, but the power consumption is too high for this application. Indeed, $P = Ri^2 = 15800$ W, with ring resistance equal to R= 1.58 Ω. To reduce maneuver time and power consumption it's preferred to use a current between 1 A and 10 A, with a power consumption between 1.58 W and 158 W.

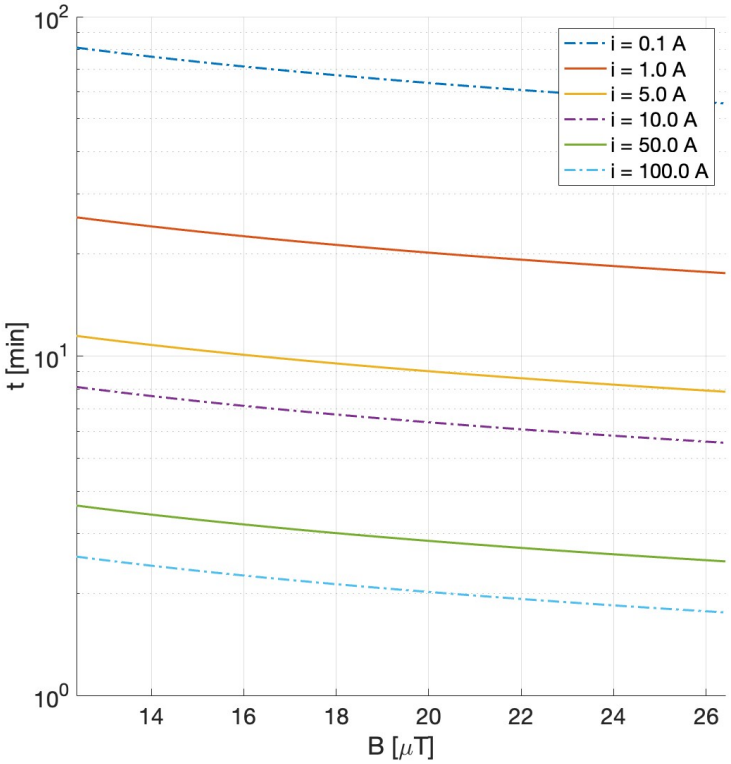

Figure 6.3 Time to align at B at different current i

6.1.2. Design of Controller for a Large Deployable Inflatable Antenna

In this section Will be evaluated a simple 1 DOF controller, to control the input current to drive the system to the desired state. Controller parameters are computed and analyzed to get reliable results, while achieving stability and responsiveness of the antenna.
For this application will be used a closed loop control, 6.4, in which the controller is dependent on the feedback from of the state variable. The output of the systems, y_k, is fed back to a comparison with the target value r_f. The controller than elaborate the error e_k between the reference value and the output to change the input u_k of the system under control.

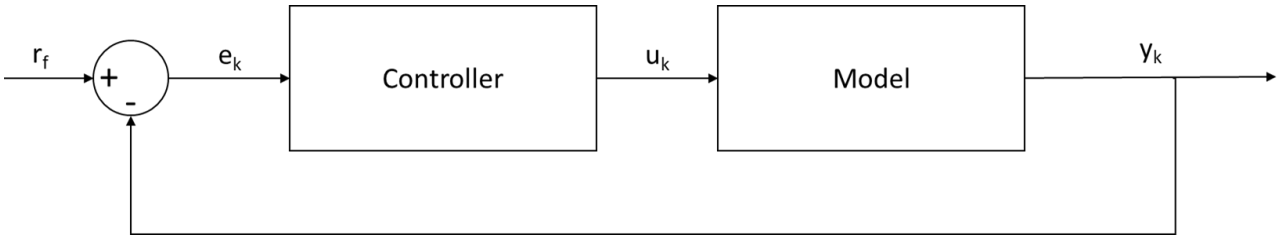

Figure 6.4 Closed loop control

In this case the model computes the angle between the magnetic field direction, $\vec{B}$, and the $\hat{u}_n$ vector perpendicular to the ring plane, while the controller compute the current i to reach the desired angle r_f.
The model that will be better explained in chapter 8.2 is a nonlinear model due to the $\sin\theta$ terms, for this reason we use a nonlinear model predictive control (Nonlinear MPC) to control the antenna system.
The system parameters used for this evaluation are:

- $B=12.384\ \mu T$.
- $S_{z_{ring}} = 706.86\ m^2$, surface of the ring orthogonal.
- $I = 8112\ Kg\ m^2$, moment of inertia of antenna in I type of geometry.
- $R = 15\ m$, Ring radius in meters.
- $\theta_0 = 90\ deg$ and $\dot{\theta}_0 = 0\ rad/s$, respectively starting angle and initial angular velocity.
- $\theta_f = 30\ deg$ and $\dot{\theta}_f = 0\ rad/s$, respectively final angle and final angular velocity.
- $Ph = 20$, the prediction horizon parameter predicts how the system will behave in the future and uses this information to make current control decisions.
- $Ch = 10$, the control horizon parameter reduces the computational load on the controller, making it more efficient.

In this analysis, will be applied a step signal to the desired angular position (theta) to test the performance of the controller. So important dynamic parameters have been calculated and commented below. The results are showed in 6.5.

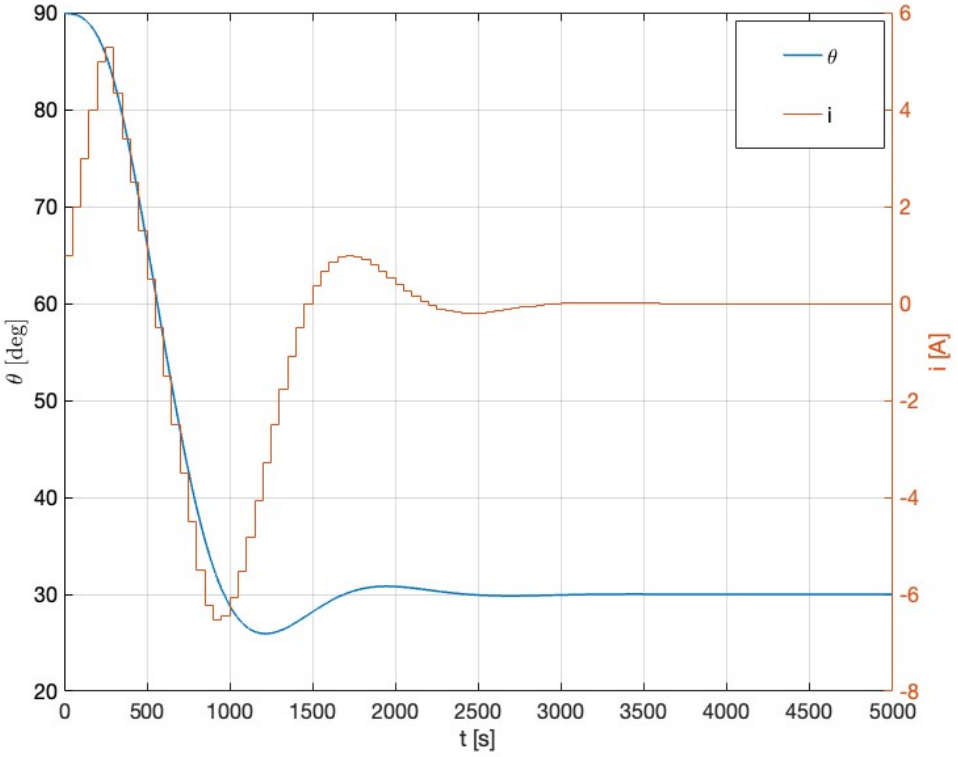

Figure 6.5 Simple control application 1 case

This figure illustrates the current along the y-axis, displaying both positive and negative values. It's important to note that the negative values indicate a reversal in the direction of current flow, implemented by the control system. This technical choice facilitates the inversion of torque, enabling precise control of the system's dynamics.
Each parameter has a specific meaning which will be analyzed as follow:

1.**Transient Time**: 1552 s
It's defined as the time required for the system's response (theta) to first enter within a certain tolerance band around the final value, typically ±5%. It represents the duration of the transient response phase where the system output is moving towards its final value but has not yet settled.
A shorter transient time is often desirable as it indicates that the system quickly starts to reach its desired state.

2. **Settling Time**: 2132 s
The settling time is the time required for the system output to remain within a certain percentage (5% in this case) of its final value for the first time. This parameter is crucial for determining how quickly the system stabilizes after a disturbance or setpoint change.

3. **Settling Min**: 25.9470 deg
It represents the minimum value that the system output reaches within the settling time window. This indicates the lowest value the controlled variable reaches as it settles. It is useful for understanding the range of oscillation from the setpoint during the transient phase.

4. **Settling Max**: 90 deg
It represents the maximum value that the system output reaches within the settling time window. This parameter shows the peak value the output reaches before settling, which usually helps in understanding the extent of overshoot.

5. **Undershoot**: 13.51 %
Undershoot refers to the percentage by which the system output falls below its final steady-state value before eventually settling to it. Undershoot is particularly relevant in this context as it provides insight into how much the output dips below the desired value. A 13.51% undershoot indicates that the output went significantly below the target before stabilizing. However, this value is acceptable, since it doesn't compromise system overall stability.

In a scenario where the system is moving from a higher initial value to a lower final value, the risk of the system dipping below the target value is more critical than the system temporarily exceeding the final value (overshoot). Particularly, significant undershoot value can indicate poor control performance, leading to potential instability.

As showed in figure 6.5, initially the controller set a positive current which has an initial increasing trend. Then, the current starts to decrease reaching the maximum negative value when the angle falls under the desired one. Larger current spikes correspond to faster changes in rotation angle. The controller changes current direction to invert the rotation and, finally, it switches the current to stop the ring at the target position. From the figure, at 1552 s the transient ends and at 2132 s, about 36 min, the ring finish to rotate at 30 deg. It can also be noticed that the rotation angle does not immediately follow the current changes perfectly. This is evident in the slight delay and overshoot (undershoot) observed in the rotation response to current steps. It's also important to note that increasing predictive horizon and control horizon values can drastically improve the system performance. However, it also increases computational complexity. The optimal choice of these parameters depends in the specific requirements of the application.

In figure 6.6, It is visible the results of a new simulation conducted with $\mathrm{Ph} = 40,\ \mathrm{Ch} = 15$. Each of the other input parameters have been maintained constant.

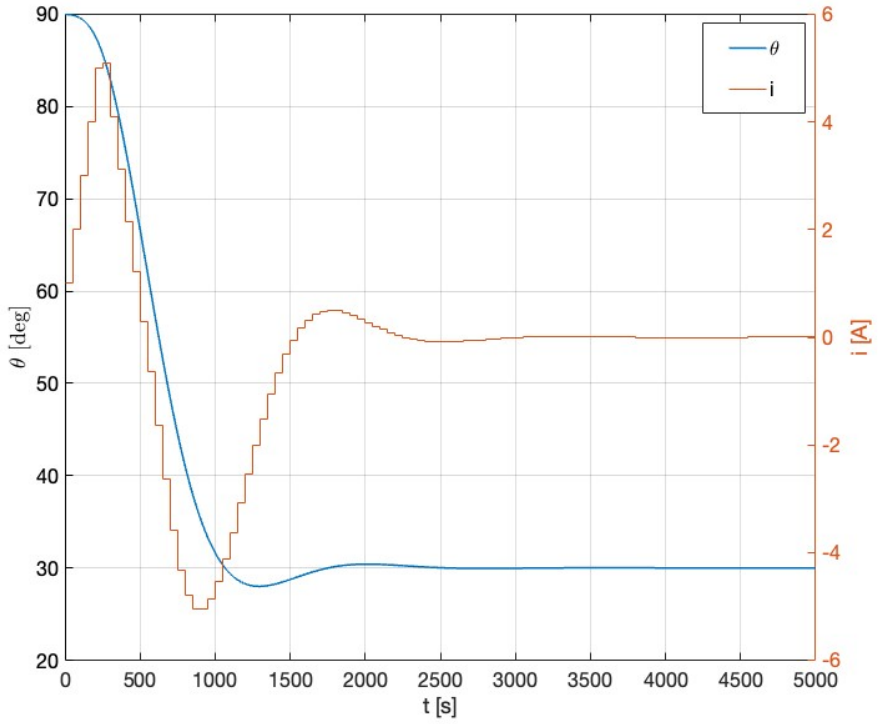

Figure 6.6 Simple control application 2 case

The resulting controller parameters are:

- Transient Time: 1509 s
- Settling Time: 1618 s
- Settling Min: 28.0025 deg
- Settling Max: 90 deg
- Undershoot: 6.66%

As expected, increasing the prediction and control horizons in a MPC controller has improved transient time and settling time. So, the system reaches the desired set point faster, improving the overall responsiveness. Furthermore, the undershoot decrease from 13.51% to 6.66%. Nevertheless, the primary drawbacks are the increased demand for processing power and the additional time required to compute the optimal control actions.
With the same hypothesis, in the Figure 6.7, the ring rotates from 90 deg to -90 deg.

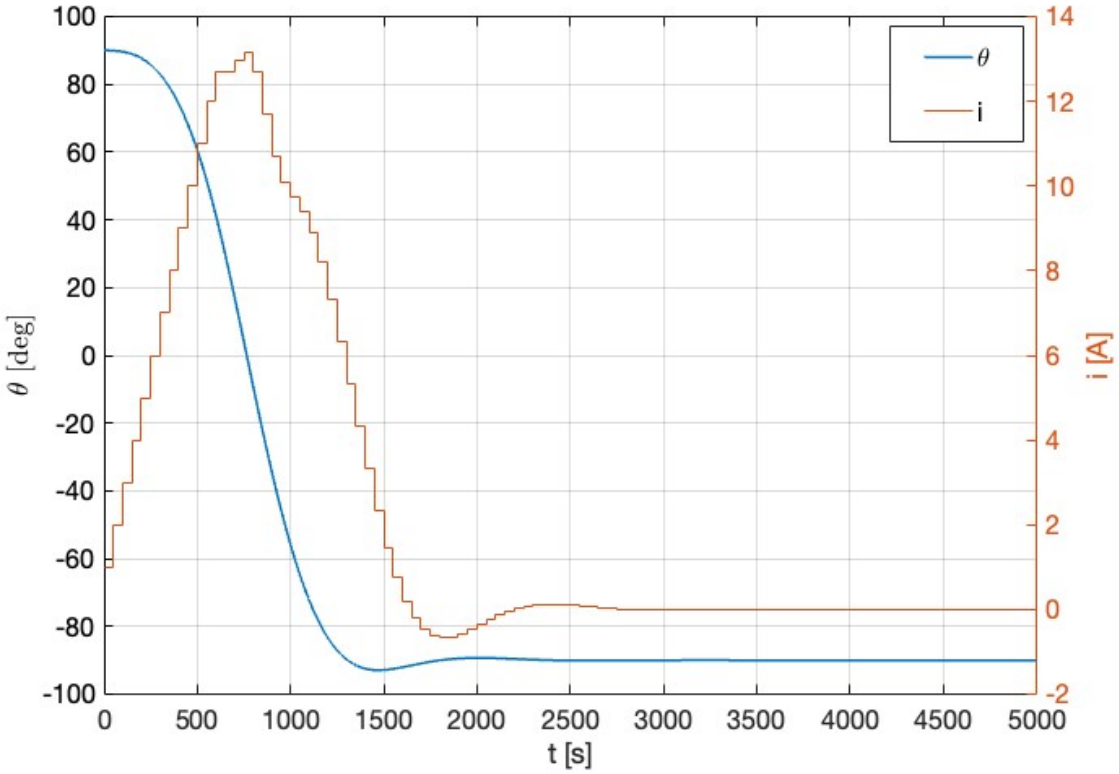

Figure 6.7 Simple control application 2 case

The parameter related to the controller are:

- Transient Time: 1240 s
- Settling Time: 1623 s
- Settling Min: -94.9146 deg
- Settling Max: -81.0007 deg
- Overshoot: 3,24 %
- Undershoot: 3,24 %

From Figure 6.7, after 1623 s about 27 min, the rotation is completed. The current values are less than 14 A and more than -2 A. At the start of the maneuver, the controller applies a positive current to initiate the rotation of the antenna toward the target angle. As the antenna's angular position approaches 0 deg, the controller reduces the current value in response to the antenna's dynamics. However, the current does not immediately reverse direction, even after θ crosses 0 deg. This phenomenon can be attributed to the interaction between the magnetic torque, the current flow, and the system's dynamics.
The magnetic torque is proportional to both the current and sinθ. When θ becomes negative, the torque acts in opposition to both the parameters, effectively preventing a reversal in the current direction. The controller maintains the same direction of current flow, as reversing it would oppose the torque's contribution to stabilizing the rotation. This behavior is evident in the figure, where the current remains positive despite angular position has negative values.

7. Simplified forces analysis

7.1. Magnetic Torque

For this preliminary analysis, the magnetic field value will be considered as constant both in module and direction (In the real case B change with the satellite latitude and the longitude).
The magnetic force can be considered as the resultant of a force systems applied at different point. Generally, the magnetic force system generates a torque that generate a rotation. For this application it will be analyzed the case of a current within a circular ring in a uniform magnetic field; in this case the resultant force is zero and the ring only rotate, without deformation.
Considering a rectangular circuit (Figure 7.1) with side a and b ($\Sigma = a \cdot b$), with a current i, let assume that the normal vector of the circuit plane, $\vec{u}_n$, is oriented as in the figure. The circuit is in a uniform magnetic field, $\vec{B}$, that forms an angle θ with the $\vec{u}_n$ vector. As in Figure 7.1, the $\vec{F}_3$ and $\vec{F}_4$ vector are equals and opposites and are on the same directions and forms a torque equal to zero. The forces $\vec{F}_1$ and $\vec{F}_2$ are equals and opposites but generate a torque equal to $Fb \sin\theta$, with $F = iaB$. Torque is equals to:

$$M = b \sin\theta \, F = iabB \sin\theta = i\Sigma B \sin\theta \qquad (7.1)$$

parallel to the circuit plane e oriented like Figure 7.1.

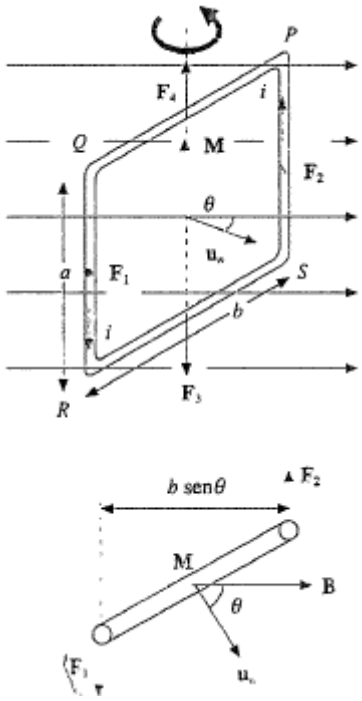

Figure 7.1 Circuit magnetic torque [7]

The circuit magnet torque applied to the circuit equals:

$$\vec{m} = i\Sigma\vec{u}_n \qquad (7.2)$$

Parallel to the $\vec{u}_n$ vector and module equals to the product of the current to the circuit area. The mechanic torque can be written like:

$$\vec{M} = \vec{m} \times \vec{B} = i\Sigma\vec{u}_n \times \vec{B} \qquad (7.3)$$

Where i is the current applied to the circuit, Σ is the ring surface and $\vec{B}$ is the magnetic field vector. This equation is valid for plane circuit of any shape in a uniform magnetic field.

7.2. Dynamics equation

Considering only the rotational equilibrium equation along the axis lying in the magnetic field plane and perpendicular to the field lines, and neglecting all perturbation torques, the following equation can be written:

$$I\alpha = I\ddot{\theta} = M = i\Sigma\vec{u}_n \times \vec{B} = -i\Sigma B \sin\theta \qquad (7.4)$$

Where α is the angular acceleration and I is the inertial torque. This equation is a nonlinear second order differential equation that can be resolved only with a numerical integration.
The last equation can be written like ($\alpha = \dot{\omega} = \ddot{\theta}$):

$$I\ddot{\theta} = I\dot{\omega} = I\frac{\omega_{k+1}-\omega_k}{\Delta t} = -i\Sigma B \sin\theta_k \rightarrow \dot{\omega} = -\frac{i\Sigma B}{I}\sin\theta_k \Delta t \qquad (7.5)$$

Where ω is the angular speed and $\Delta t = h$ is the integration step.
From this equation follow:

$$\omega_{k+1} = \omega_k - \frac{i\Sigma B}{I} h \sin\theta_k \qquad (7.6)$$

Where ω_{k+1} is the angular speed at k+1-step, ω_k is the angular speed at k-step and h is the integration step.
From the integration of the last equation is possible to obtain the θ angle:

$$\frac{d\theta}{dt} = \omega \rightarrow \frac{\theta_{k+1}-\theta_k}{\Delta t} = \omega_k = \omega_{k-1} - \frac{i\Sigma B}{I} h \sin\theta_{k-1} \qquad (7.7)$$

Follow:

$$\theta_{k+1} = \theta_k + \omega_k \Delta t = \theta_k + h\omega_{k-1} - \frac{i\Sigma B}{I} h \sin\theta_{k-1}$$

$$\theta_{k+1} = \theta_k + h\omega_{k-1} - \frac{i\Sigma B}{I} h^2 \sin\theta_{k-1}$$

The model, in this way, can be summarize in the following equation systems:

$$\begin{cases} \omega_{k+1} = \omega_k - \dfrac{i\Sigma B}{I} h \sin\theta_k \\ \theta_{k+1} = \theta_k + h\omega_{k-1} - \dfrac{i\Sigma B}{I} h^2 \sin\theta_{k-1} \\ \theta_0 = \theta(t=0) \\ \omega_0 = \omega(t=0) \end{cases}$$

7.3. Electromagnetic induction on the copper rings

Faraday's law of induction is used to compute the magnetic flux ϕ_B throught a region of space enclosed by a wire loop. The magnetic flux is defined by a surface integral:

$$\Phi(B) = \int_{\Sigma} \vec{B} \cdot \hat{u}_n d\Sigma \qquad (7.8)$$

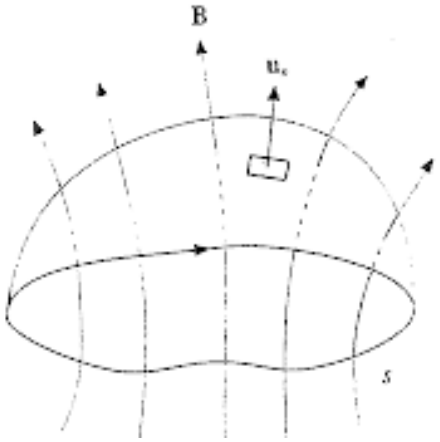

Figure 7.2 Magnetic flux on a close circuit [7]

where $d\Sigma$ is an element of the surface σ enclosed by the wire loop and $\vec{B}$ is the magnetic field. The scalar product $\vec{B} \cdot \hat{u}_n$ is the infinitesimal amount of magnetic flux.
When the flux through the surface changes, Faraday's law of induction says that the wire loop acquires an electromotive force. The induced electromotive force in any closed circuit is equal to the rate of change of the magnetic flux enclosed by the circuit:

$$\mathcal{E} = -\frac{d\Phi_B}{dt} \qquad (7.9)$$

The direction of the electromotive force is given by Lenz's law which states that an induced current will flow in the direction that will oppose the change which produced it. [18]
This is due to the negative sign in the previous equation.
Replacing the magnetic flux equation in the last equation and with $\vec{B}$ and Σ constant follow:

$$\mathcal{E} = -\frac{d}{dt}\int_{\Sigma} \vec{B} \cdot \hat{u}_n d\Sigma = -\frac{d}{dt}\int_{\Sigma} B\cos\theta\, d\Sigma = -\frac{d}{dt}(B\Sigma\cos\theta) = B\Sigma\, sin\,\theta\,\omega \qquad (7.10)$$

Replacing the Ohm law, $V = Ri$:

$$i_{induced} = \frac{B\Sigma}{R}\sin\theta\,\omega \qquad (7.11)$$

Where R is the ring resistor.

For this application, B have been supposed equal $43.52\ \mu T$, an input current i of 1 A, a total ring's surface of $706.86\ m^2$, a resistance of $1.58\ \Omega$ and a starting condition with an angle, θ_{start}, of 90 deg and zero initial speed, $\omega = 0\frac{rad}{s}$, so the follow results have been obtained:

Table 7.1 Induced magnetic current generated during a Rotation from 90° to 0°

CONDITION	**i [A]**	**θ [deg]**	**ω** $\left[\frac{\mathbf{rad}}{\mathbf{s}}\right]$
$\mathbf{i_{max}}$	$2.864*10^{-5}$	54.81	-0.0018
$\mathbf{E_{tot}}$ **[J]**[1]	$1.099*10^{-6}$	-	
$\overline{\mathbf{P}}$ **[W]**[1]	$1.35*10^{-9}$		

For the considered current of a few A to orient the spacecraft, the induced magnetic current can be neglected because it is approximately 1 million times lower than the considered main current.

[1] Value referred to a rotation from 90 deg to 0 deg

8. Evaluations of forces acting on the walls of an orbiting inflatable balloon

The Lorent's forces are responsible for the ballon rotation, however there are some components of the force which act on the ballon walls. Depending on the current direction, they can act as traction or compression forces. When the conductor crossed by current is immersed in a magnetic field to each electron is applied the Lorentz force [6]:

$$F_L = -e\vec{v}_d \times \vec{B} \qquad (8.1)$$

Where:

- e, is the electron charge
- $\vec{v}_d$, is the derivation electron speed
- $\vec{B}$, is the magnetic field.

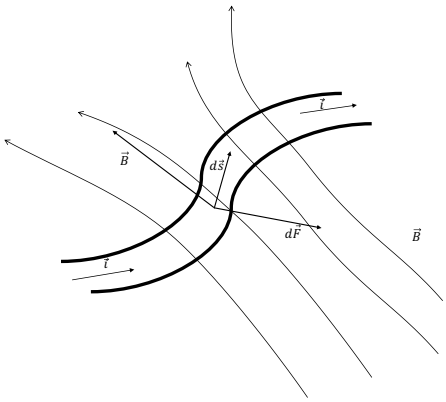

Figure 8.1 Magnetic force applied to a wire with a current I [7]

In a conductor section length "ds" and an area "Σ", there are $n * \Sigma ds$ electron and the total force can be computed as:

$$d\vec{F} = n\Sigma ds\vec{F}_L = -(\Sigma ds)ne\vec{v}_d \times \vec{B} = \Sigma ds\vec{j} \times \vec{B} \qquad (8.2)$$

Where $\vec{j} = ne\vec{v}_d$ is the current density. From this equation, Σds is the infinitesimal volume, $d\tau$ the volumetric force applied to the wire is:

$$\vec{F}_\tau = \vec{j} \times \vec{B} \qquad (8.3)$$

Considering a wire conduction and the current through the wire, i, is equal to Σj and with $d\vec{s}$ in the same direction of $\vec{j}$ follow that:

$$d\vec{F} = id\vec{s} \times \vec{B} \qquad (8.4)$$

This equation is the second elementary Laplace law and says that the magnetic force on a infinitesimal wire section is orthogonal to the wire and to the magnetic field: the module is equal to $dF = iB\sin\theta$ with θ the angle between $d\vec{s}$ and $\vec{B}$ and direct like Figure 8.1. The force is proportional to the current intensity.

The force on a finite length wire, through with a steady state current, i, is equals to:

$$F = i\int_P^Q d\vec{s} \times \vec{B}$$

Where P and Q are the wire ends. For a curvilinear planar wire, it can be demonstrated that the force is equals to:

$$F = i\int_P^Q d\vec{s} \times \vec{B} = i\overrightarrow{PQ} \times \vec{B} \qquad (8.5)$$

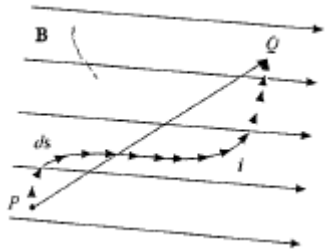

Figure 8.2 Magnetic force on a curvilinear planar wire [7]

8.1. Application of the Laplace law on a conductor ring

As explained in the previous section, the infinitesimal force applied on an infinitesimal section of wire is:

$$d\vec{F} = \vec{\imath} \times \vec{B}ds$$

With ds the infinitesimal length.
For our purpose, the current $\vec{\imath}$, Figure 8.3, can be decomposed in a component in the ξ direction and a component in η, in the ring plane:

$$\vec{\imath} = \begin{cases} i_\xi \\ i_\eta \end{cases} = \begin{cases} -i\sin\beta\,\hat{\xi} \\ i\cos\beta\,\hat{\eta} \end{cases}$$

Where β is the angle between the $O\vec{P}$ vector and ξ-axis.

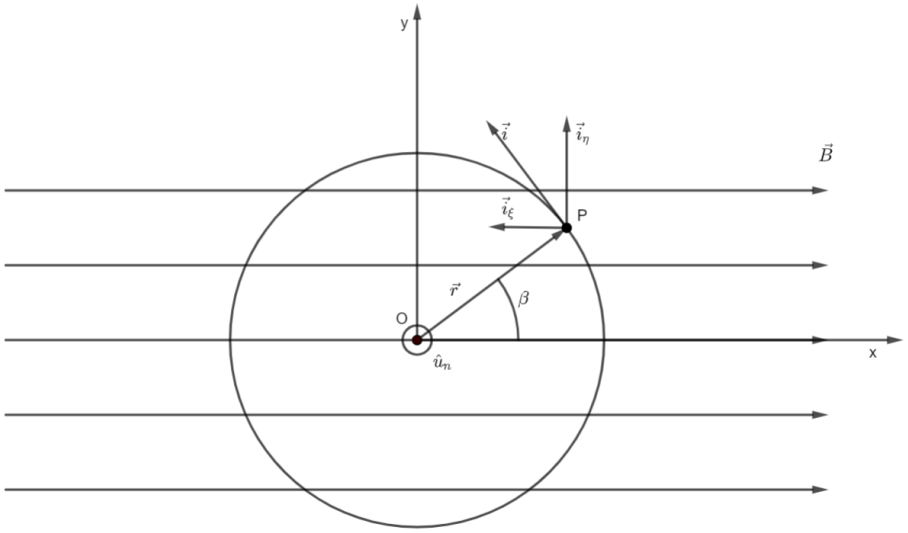

Figure 8.3 Current-carrying ring in a constant uniform magnet field

Replacing the current in the force equation follow:

$$\frac{d\vec{F}_\xi}{ds} = \vec{i}_\xi \times \vec{B} = -i \sin\beta\, \hat{\xi} \times \vec{B} = iB \sin\beta \cos\theta\, \hat{\jmath} \qquad (8.6)$$

$$\frac{d\vec{F}_\eta}{ds} = \vec{i}_\eta \times \vec{B} = i \cos\beta\, \hat{\eta} \times \vec{B} = -iB \cos\beta \sin\frac{\pi}{2} \hat{k} = -iB \cos\beta\, \hat{k} \qquad (8.7)$$

Where θ is the angle between $\vec{B}$ and $\hat{u}_n$, $\hat{\jmath}$ indicate the y direction axis and $\hat{K}$ indicate the z direction axis, Figure 8.4. The eta component doesn't depend to θ because $\hat{\eta}$ is always perpendicular to the magnetic field.
Each force generated by the magnetic field on the wire has an equal and opposite force, Figure 8.5, for this reason there is no translation of the loop but only the rotation along the y axis. The force responsible to the ring rotation are the $\vec{F}_\eta$ that have a distance different to zeros and equals to $b = 2R \cos\frac{\Delta\beta}{2} \sin\theta$. However, the $\vec{F}_\xi$ have a null distance and stretch the ring in the y direction.
The max force induced from the ring to the satellite structure is:

- For the ξ axis when $\theta = n\pi$ with $n \in Z_0$ and $\beta = (2n+1)\frac{\pi}{2}$ with $n \in Z_0$:

$$\left\| \frac{d\vec{F}_\xi}{ds} \right\| = iB$$

- For the η axis when $\beta = n\pi$ with $n \in Z_0$:

$$\left\| \frac{d\vec{F}_\xi}{ds} \right\| = iB$$

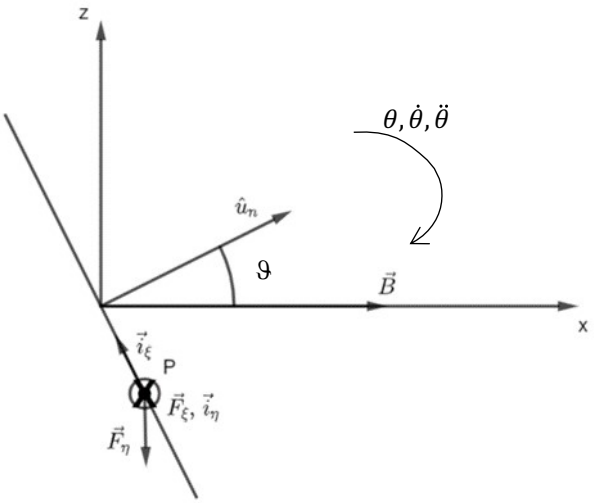

Figure 8.4 Magnetic force action on the ring

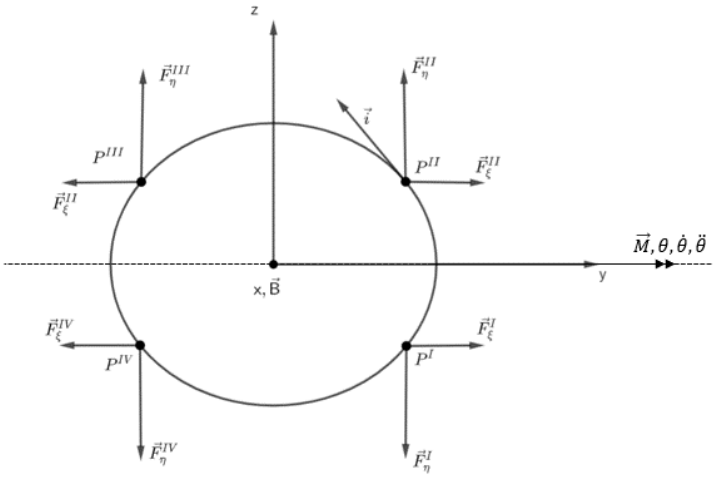

Figure 8.5 Forces acting on the ring

The total magnetic force acting on the ring can be calculating like:

$$\left|\frac{d\vec{F}}{ds}\right|_{tot} = \sqrt{\left(\frac{dF_\xi}{ds}\right)^2 + \left(\frac{dF_\eta}{ds}\right)^2} = iB\sqrt{\sin^2\beta\cos^2\theta + \cos^2\beta} = iB\sqrt{1 - \sin^2\theta\sin\beta^2} \qquad (8.8)$$

Assuming these conditions:

$$0 \le \sin^2(\beta), \sin^2(\theta) \le 1$$

Follow that:

$$\left|\frac{d\vec{F}}{ds}\right|_{tot} \le iB$$

The max force is proportional to the magnetic field module, B, and the current intensity, i. With a maximum B of 43.52 μT and a current of 100 A the maximum load on the balloon's shape is equal to:

$$\left|\frac{d\vec{F}}{ds}\right|_{tot_{max}} = iB = 43{,}52 * 10^{-6} * 100 = 43{,}52 * 10^{-4}\,\frac{N}{m}$$

The force direction changes with the current direction, if the current direction is counterclockwise the magnetic force acting on the balloons shape is a traction force, otherwise if the current direction is clockwise the magnetic forces are compressive forces.
The total force acting on the balloons form an angle from the ring plane equals to:

$$\tan\gamma = \frac{\left(\frac{dF_\xi}{ds}\right)}{\frac{dF_\eta}{ds}} = \frac{iB\sin\beta\cos\theta}{-iB\cos\beta} = -\tan\beta\cos\theta$$

When θ is nπ with $n \in Z_0^+$ than $\gamma = \pm\beta$, otherwise when θ is $\frac{2n+1}{2}\pi$ with $n \in Z_0^+$ γ is 0 and the total force is orthogonal to the balloon's shape.

8.2. Forces responsible to balloon rotation

The forces responsible to the balloon's rotation are the $\vec{F}_\eta$:

$$\frac{d\vec{F}_\eta}{ds} = -iB\cos\beta\,\hat{k}$$

The infinitesimal force for length unit is proportional to the current and the magnetic field and changes with the β angle, **Errore. L'origine riferimento non è stata trovata.**. When β is equal to 0 deg, $\frac{d\vec{F}_\eta}{ds}$ assume its max value equals to $-iB$, else if β is equals to 90 degree the force value is equals to 0.

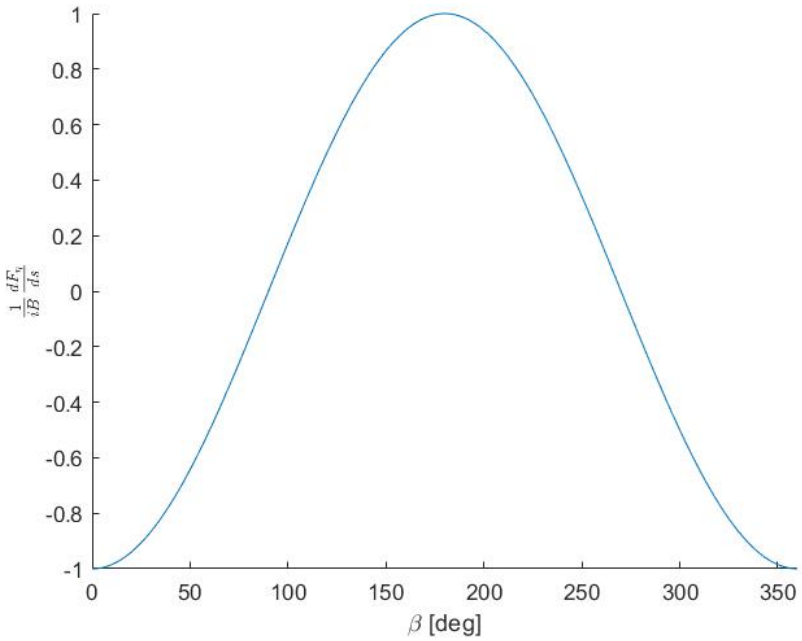

Figure 8.6 Dimensionless rotational forces vs. β angle

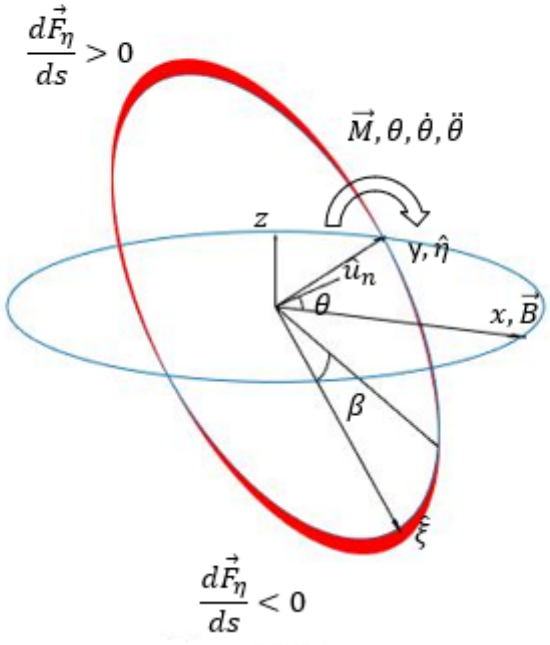

Figure 8.7 Force distribution at θ=30 deg

8.3. Tangential forces and their areal distribution

In Figure 8.8, it is visible the forces decomposition in tangential and radial component of the ξ and η component.

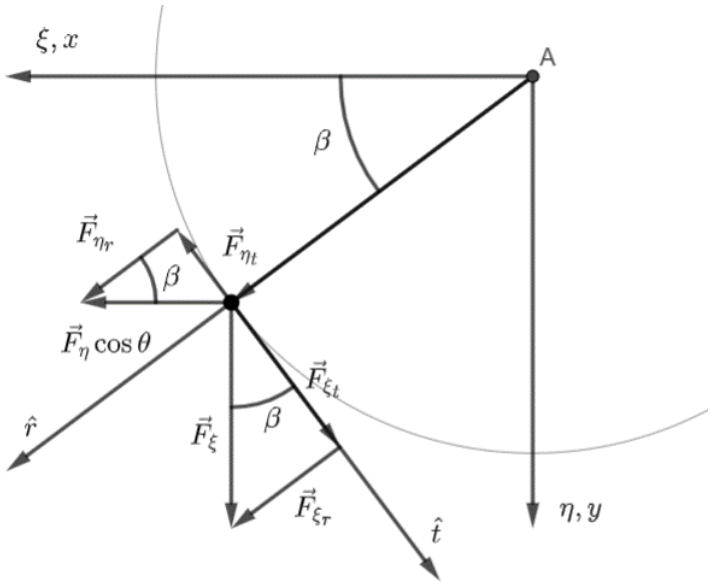

Figure 8.8 Magnetic force radial and tangential component

According to the Figure 8.8, the tangential forces, $\vec{F}_t$ to the balloons shape can be written:

$$\frac{d\vec{F}_t}{ds} = \left(\frac{d\vec{F}_\xi}{ds} \cdot \hat{t}\right)\hat{t} + \left(\frac{d\vec{F}_\eta}{ds}\cos\theta \cdot \hat{t}\right)\hat{t} = \frac{dF_\xi}{ds}\cos\beta\,\hat{t} + \frac{dF_\eta}{ds}\cos\theta\sin\beta\,\hat{t}$$
$$= (iB\cos\beta\sin\beta\cos\theta - iB\cos\beta\sin\beta\cos\theta)\hat{t} = 0$$

There are no tangential forces applied from the ring to the balloon surface.

8.4. Orthogonal forces to the balloons surface

The radial component, $d\vec{F}_r$, Figure 8.8, normal to the balloons shape is equals to:

$$\frac{d\vec{F}_r}{ds} = \left(\frac{d\vec{F}_\xi}{ds} \cdot \hat{r}\right)\hat{r} + \left(\frac{d\vec{F}_\eta}{ds}\cos\theta \cdot \hat{r}\right)\hat{r} = \frac{dF_\xi}{ds}\sin\beta\,\hat{r} - \frac{dF_\eta}{ds}\cos\theta\cos\beta\,\hat{r}$$
$$= iB\cos\theta\sin^2\beta\,\hat{r} + iB\cos\theta\cos^2\beta\,\hat{r} = iB\cos\theta\,(\sin^2\beta + \cos^2\beta)\hat{r} = iB\cos\theta\,\hat{r}$$

Where $\hat{r}$ is the radius infinitesimal vector with direction from the ring's center to the ring. The value of the radial forces is constant with β.

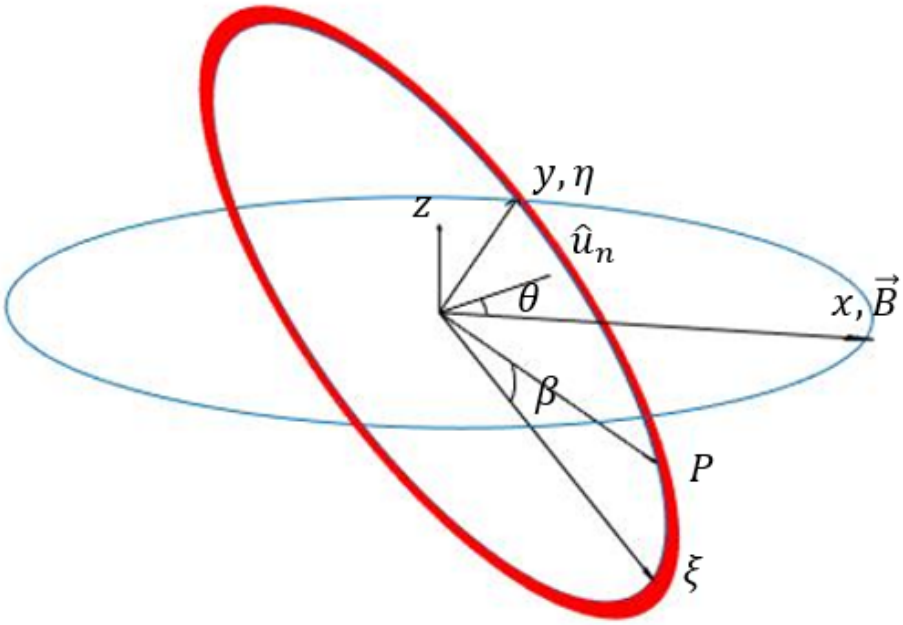

Figure 8.9 Radial force distribution

When θ is zero degree, the radial component reaches its maximum value equals to:

$$\left(\frac{d\vec{F}_r}{ds}\right)_{max} = iB$$

The value of the radial force is in range of:

$$-iB\cos\theta \leq \frac{d\vec{F}_r}{ds} \leq iB\cos\theta$$

To compute the radial stress, σ_r, due to the magnetic forces applied orthogonal to the balloon's surface, the radial linear force distribution is divided by the deep of the ring, d:

$$\sigma_r = \frac{1}{d}\frac{d\vec{F}_r}{ds} \rightarrow -\frac{iB}{d}\cos\theta \leq \sigma_r \leq \frac{iB}{d}\cos\theta \qquad (8.9)$$

The maximum stress is when θ is zero deg:

$$\sigma_{r_{max}} = |\sigma_r|_{\theta=0}$$

When $i > 0$ the maximum traction pressure, σ_{tr}, is:

$$\sigma_{r_{tr_{max}}} = \frac{iB}{d}$$

And the maximum compression pressure, σ_c, is computed as:

$$\sigma_{r_{c_{max}}} = \frac{iB}{d}$$

Else the forces are reversed.

The ring can be assumed as cylindrical wire with a section of 1 mm^2, $d = 2\sqrt{\frac{A}{\pi}} = 1.13$ mm.

In this case the max radial stress, σ_r is equal to:

$$\sigma_{r_{max}} = \left(\sigma_{r_c}, \sigma_{r_{tr}}\right)_{max} = \frac{(iB)_{max}}{d} = \frac{100 * 43{,}525 * 10^{-6}}{1{,}13 * 10^{-3}} = 3{,}85 \text{ Pa}$$

If the conductor is shaped as a copper strip 10 cm wide, d, the max radial stress, σ_r:

$$\sigma_{r_{max}} = \left(\sigma_{r_c}, \sigma_{r_{tr}}\right)_{max} = \frac{(iB)_{max}}{d} = \frac{100 * 43{,}525 * 10^{-6}}{0{,}10} = 4{,}35 * 10^{-2} \text{ Pa}$$

With a copper strip the structural load is 100 times less than the use of a copper wire.
To reduce the effect of the compression load, the balloons internal pressure, due to the internal gas, must be much than 3,85 Pa in the case of a cylindrical ring or much than $4{,}35*10^{-2}$ Pa in the case of the copper string.

9. Preliminary Structural Analysis

Introduction

The structural integrity of the inflatable antenna in the space environment is a critical aspect of its overall performance and reliability. The geometry selected for this analysis corresponds to a parabolic reflector with a focal-to-diameter (F/D) ratio of 0.38, as described in previous chapters. This ratio has been selected to have a compromise between compact stowage requirements and efficient signal reflection. This chapter presents the structural analysis conducted using ANSYS Mechanical, with a particular focus on the antenna's response to inflation pressure and the forces exerted by the traction/compression Z-ring. The analysis also examines the stress distribution across the antenna's surface after deployment, during inflation phase. The stress distribution encountered during and after Rigidization phase can be evaluated in future studies.

The primary goal of the analysis was to evaluate the stresses and deformations induced in the antenna's material by the operational loads and ensure they remain within acceptable limits. The study also aimed to identify critical zones that may require reinforcement or design adjustments.
To achieve this, the model was discretized using a triangular mesh, which is particularly suitable for capturing the curvature and complexity of the parabolic geometry.

Moreover, the methodology used in the simulation will be explained, including the setup of boundary conditions and material properties, and presents the results in terms of stress distribution, maximum deformation, and the verification of structural compliance with the material's yield limits.

9.1. Structural analysis overview

This section presents a preliminary static structural analysis to evaluate the feasibility of the inflatable balloon antenna. The analysis focuses on the first geometric configuration introduced in previous sections and illustrated in Figure 9.1. The structure is characterized by a parabolic reflector and a transparent canopy, with respective thicknesses of 12.6 μm and 12.8 μm. For simplification in this initial study, a uniform thickness of 12.5 μm has been applied throughout the entire structure, as the Mylar layer serves as the primary structural component of the antenna. The multilayer shell configuration, which includes functional layers for reflectivity and protection, has been detailed in earlier chapters.

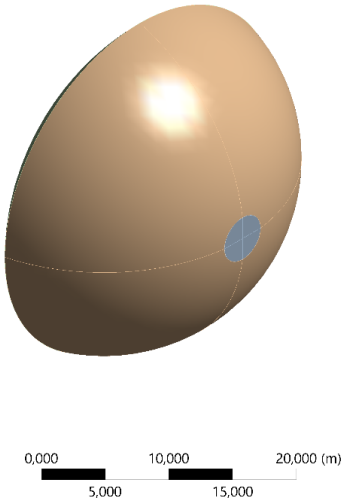

Figure 9.1 Structural analysis geometry

To accurately capture the curvature and complexity of the parabolic geometry, the structure was meshed using triangular shell elements, as shown in Figure 9.2. This choice of element ensures that the mesh conforms well to the curved surfaces and provides a robust representation for thin-shell structures. A carefully defined mesh is crucial in this context to balance computational efficiency with the precision needed to resolve the stresses and deformations induced by the applied loads.

The loads applied in this simulation include:

- **Inflation Pressure:** A uniform pressure applied internally to simulate the effect of the inflation gas on the canopy and reflector surfaces. This pressure is the primary load responsible for maintaining the antenna's deployed shape before rigidization.
- **Traction and Compression Forces:** Generated by the traction/compression ring, these forces have been modelled as line pressure. These forces are applied on the antenna's membrane during the balloon movement.

During its orbit path, the antenna faces a wide range of temperature. In the following sections, it will be exploited two cases in which the reference temperatures are the extremal ones.
The simulation parameters and boundary conditions have been tailored to represent the operational environment in low Earth orbit (LEO).

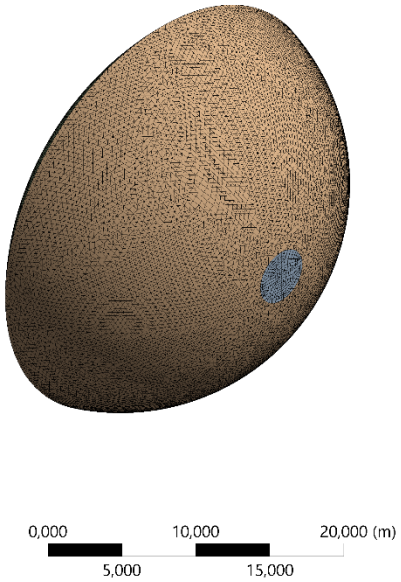

Figure 9.2 Structural analysis mesh

9.2. Methodology for Evaluating Stress and Strain Control

To ensure the structural integrity and operational feasibility of the inflatable antenna, it is essential to verify that the stress and strain within the material remain below acceptable thresholds. This section outlines the methodology employed to evaluate the stress and strain levels resulting from the applied loads, as well as the criteria used to determine their compliance with material limits.

9.2.1. Material Limits and Safety Factors

The material used for the antenna's structure is a multilayer shell with Mylar serving as the primary structural component. The mechanical properties of Mylar, including its yield stress and modulus of elasticity, have been documented in previous sections and provide the foundation for evaluating its performance under operational loads.

- **Yield Stress**: The material's yield stress defines the maximum allowable stress beyond which permanent deformation may occur. For Mylar at 25°C temperature, the yield stress is:

$$\sigma_{yield} = 68{,}94 \text{ MPa}$$

- **Safety Factor (SF)**: To ensure robustness, a safety factor of 2 is applied:

$$\sigma_{max\_allowable} = \frac{\sigma_{yield}}{SF} = 34{,}47 \text{ MPa} \qquad (9.1)$$

The maximum allowable strain is derived from the material's modulus of elasticity (E= 3,79 GPa) and Hooke's law:

$$\varepsilon_{max\_allowable} = \frac{\sigma_{max\_allowable}}{E} = 0{,}0091 = 0{,}91\% \qquad (9.2)$$

As anticipated, the simulation has been conducted considering the extremal temperature faced by the antenna during its path. Moreover, the yield stress and other parameters are dependent to temperature variation. So, the correct values of these parameters have been adjusted below:

- Hot case T= 358,40 K the yield stress point decreases according to the following formula:

  $$\sigma_y(T) = \sigma_{y,ref}(1 - k(T - T_{ref})) = \quad 60{,}63 \quad \text{MPa} \qquad (9.3)$$

  Where $\sigma_{y,ref}$= 68,94 MPa at 298,15 K, k= 0,002 1/K (material parameter dependent to temperature variation).
  So, $\sigma_{allowable\_hot} = 30{,}32$ Mpa
  Young Modulus also changes: E= (0,70 $E_{25°C}$)= 2,65 GPa

  So, $\varepsilon_{max\_allowable} = \frac{\sigma_{allowable\_hot}}{E} = 0{,}0114 = 1{,}14\%$ (9.4)

- Cold case T= 188,64 K the yield stress point increase according to the following formula
  $\sigma_y(T) = \sigma_{y,ref}\big(1 - k(T - T_{ref})\big) =$ 84,04 MPa
  So, $\sigma_{allowable_{cold}} = 42{,}02$ Mpa

  Young Modulus also changes: E=(1,20$E_{25°C}$)= 4,55 GPa
  So, $\varepsilon_{max\_allowable} = \frac{\sigma_{allowable\_cold}}{E} = 0{,}0092 = 0{,}92\%$

9.2.2. Stress and Strain Evaluation in ANSYS

The evaluation of stress and strain is a complex procedure, and it has been made through the Ansys mechanical simulation tool. The maximum equivalent stress has been computed with the Von Mises criteria, which evaluate whether the material experiences stress levels below the allowable threshold. This criterion accounts for multiaxial stress rated and is expressed as:

$$\sigma_{VM} = \sqrt{\frac{1}{2}\left[(\sigma_x - \sigma_y)^2 + (\sigma_y - \sigma_z)^2 + (\sigma_z - \sigma_x)^2\right] + 3\tau_{xy}^2} \qquad (9.5)$$

The maximum Von Mises stress is then compared with the maximum value of stress previously computed.
While the equivalent elastic strain is computed by the software, considering both axial and shear components. Then the maximum value of strain is compared to $e_{max\_allowable}$ to ensure that deformation remain in elastic field.

9.2.3. Identifying Critical Zones

Stress Concentration Zones

After conducting the simulation in both cases, the critical zone is easily identified since it has the highest value of Von Mises equivalent stress.

Strain Distribution

Areas where the strain approaches the allowable limit are identified to ensure that localized deformations do not compromise the structural integrity.

9.2.4. Strain values correction

Temperature significantly affects the strain experienced by the material. To accurately account for this contribution in the analysis, the thermal strain component is included:

$$\varepsilon_{temp} = \alpha \Delta T \qquad (9.6)$$

Where:

- α: Thermal expansion coefficient of Mylar.
- ΔT: Temperature variation from the reference temperature of 25°C, covering both the hot and cold cases.

So, the static structural simulation computes the equivalent Von Mises strain, which refers to mechanical loads. Then, it is taken the max strain value, and the thermal component is added respectively for each case.

9.3. Inflation pressure determination and gas evaluation

The structural analysis conducted identified an optimal inflation pressure of 12 Pa for the hot case of the antenna. This pressure was chosen to ensure the structural stability of the antenna while maintaining stresses and deformations within the allowable limits. Under this pressure, the antenna can sustain its shape and functionality, even under elevated temperatures, without exceeding the material's yield stress.
Nitrogen (N) was selected as the inflation gas, it offers a range of properties that make it suitable for space applications:

- It remains thermally stable and gaseous across the wide temperature range expected in orbit.
- Its inert nature ensures it does not react with the Mylar or any of the other layers used in the antenna's construction.
- Its low molecular weight minimizes the mass required for inflation, which is critical for optimizing the stowage volume and reducing the overall launch mass.

The required mass of nitrogen to achieve the inflation pressure of 12 Pa was estimated based on the antenna's volume and the operational temperature. Using the ideal gas law, the calculated mass will be:

$$M = \frac{pV}{RT} = \frac{12*4029,41}{296*358,40} = 0.45 \text{ Kg} \qquad (9.7)$$

So, considering an inflation pressure of 12 Pa at 358,40 K, the inflation mass needs to inflate the antenna is 0,45 Kg.

While, in the cold case the temperature is T=188 K, using the same amount of gas the inflation pressure can be computed:

$$p = \frac{MRT}{V} = \frac{0{,}45 * 296 * 188}{4029{,}41} = 6{,}25 \text{ Pa}$$

The force due to the ring on the balloon is a line pressure equal to:

$$\left(\frac{dF}{ds}\right)_{max} = (Bi)_{max} = 100 * 43{,}525 * 10^{-6} = 4{,}35 * 10^{-3} \frac{N}{m}$$

and can be a compression or a traction force according to the current direction.
This selection of inflation pressure and gas forms a critical component of the antenna's design, balancing structural performance and operational efficiency.

9.4. Simulation Results Hot Case

The structural simulation results provided valuable insights into the performance of the inflatable antenna under the operational conditions defined in the study. The analysis' results for the hot case, conducted using ANSYS Mechanical, are showed in the following pictures.

Equivalent Von Mises Stress distribution results

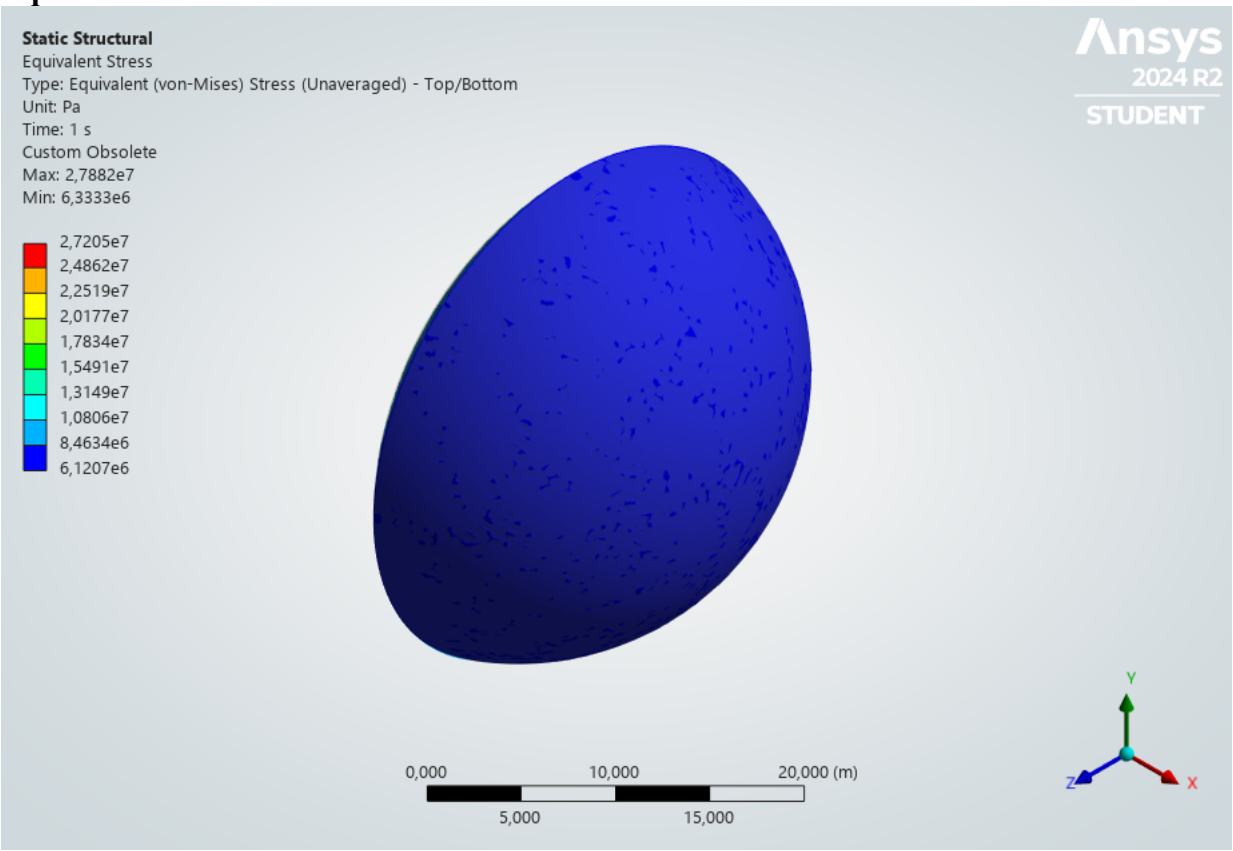

Figure 9.3 Equivalent Von Mises stress distribution in Hot case – Isometric view of canopy

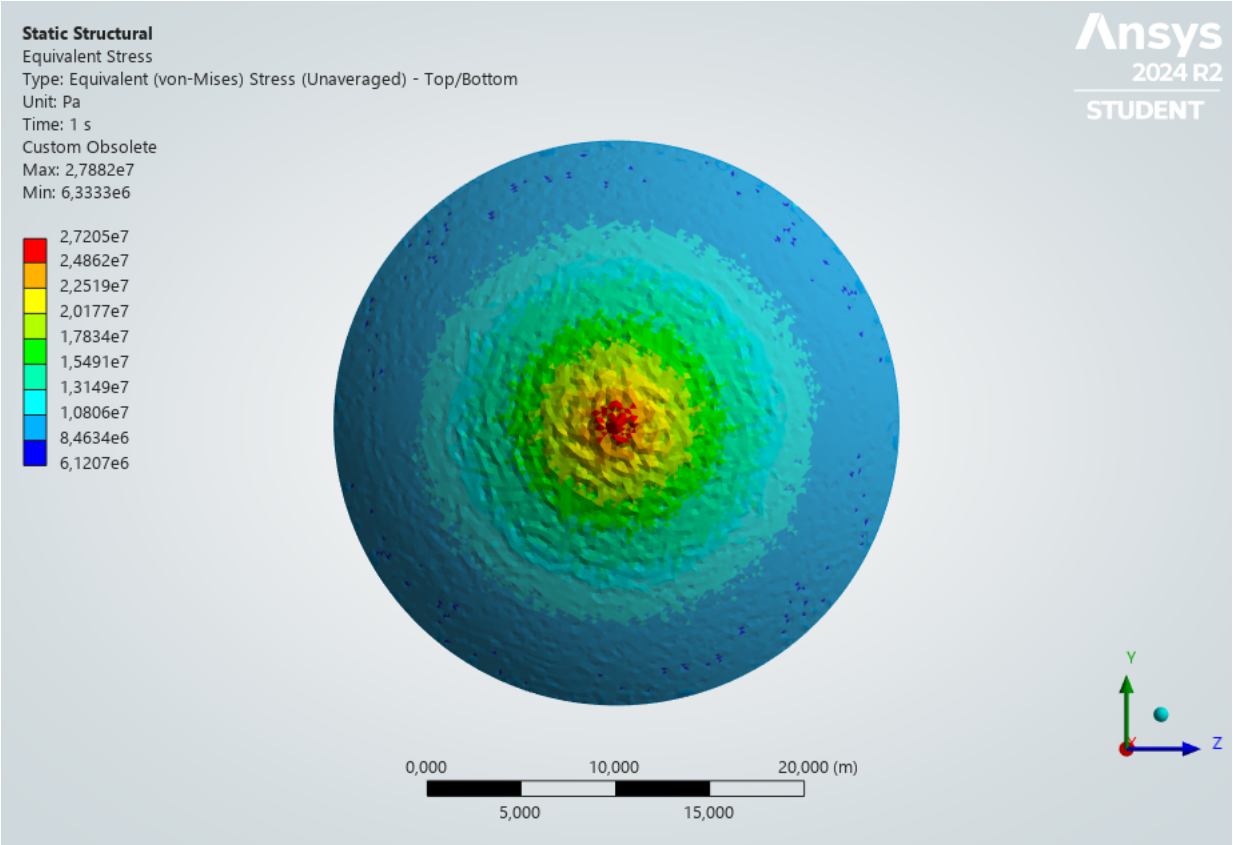

Figure 9.4 Equivalent Von Mises stress distribution in Hot Case – Reflector

The results have demonstrated that the line pressure applied by the Z ring during balloon motion is negligible respect to the stress generated on membrane by inflation pressure. For this reason, the equivalent stress values and equivalent elastic strain values have been computed for the traction ring case (the compression case reported the same values). Applying an inflation pressure of 12 Pa at 358,40 K, the maximum stress is reached on the central point of the reflector section of the antenna with a value of 27,88 MPa.

Equivalent Elastic Strain distribution results

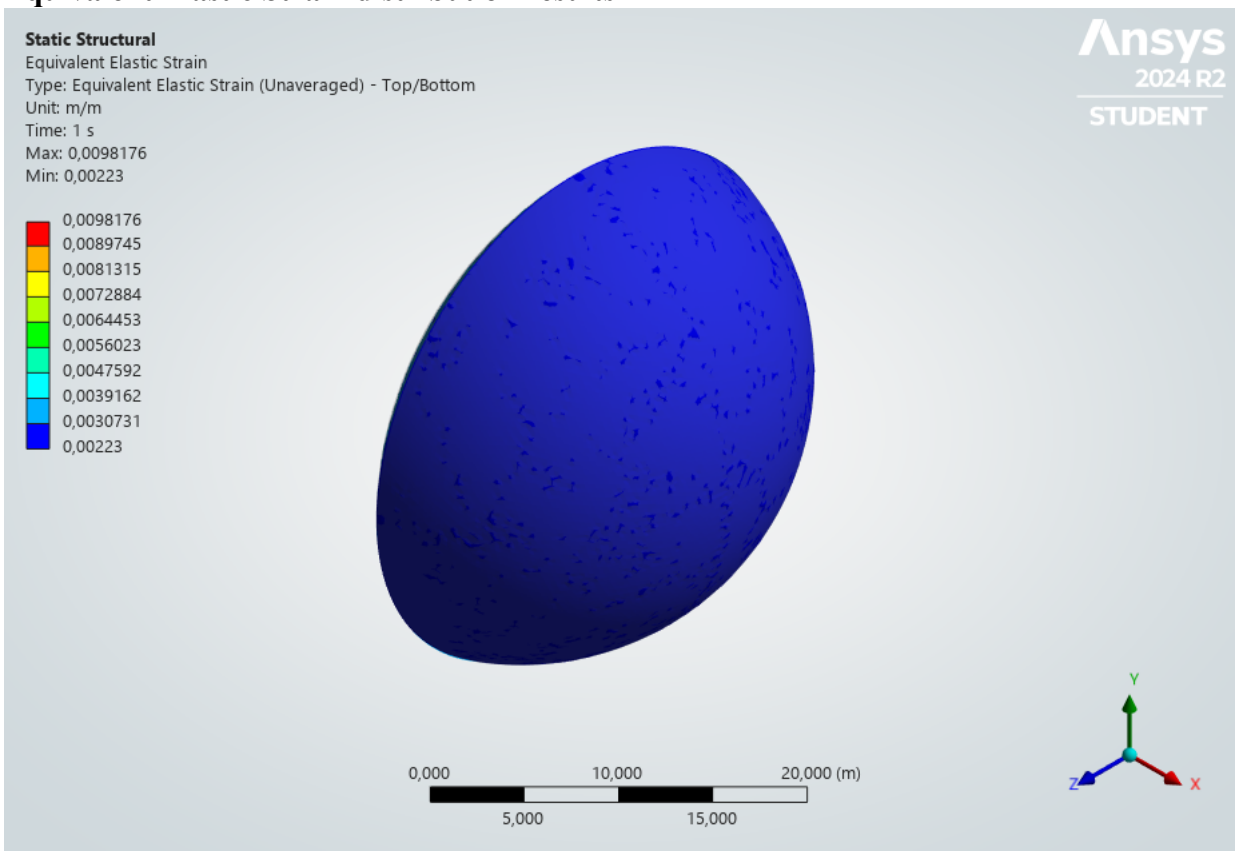

Figure 9.5 Equivalent Elastic Strain in Hot case – Canopy

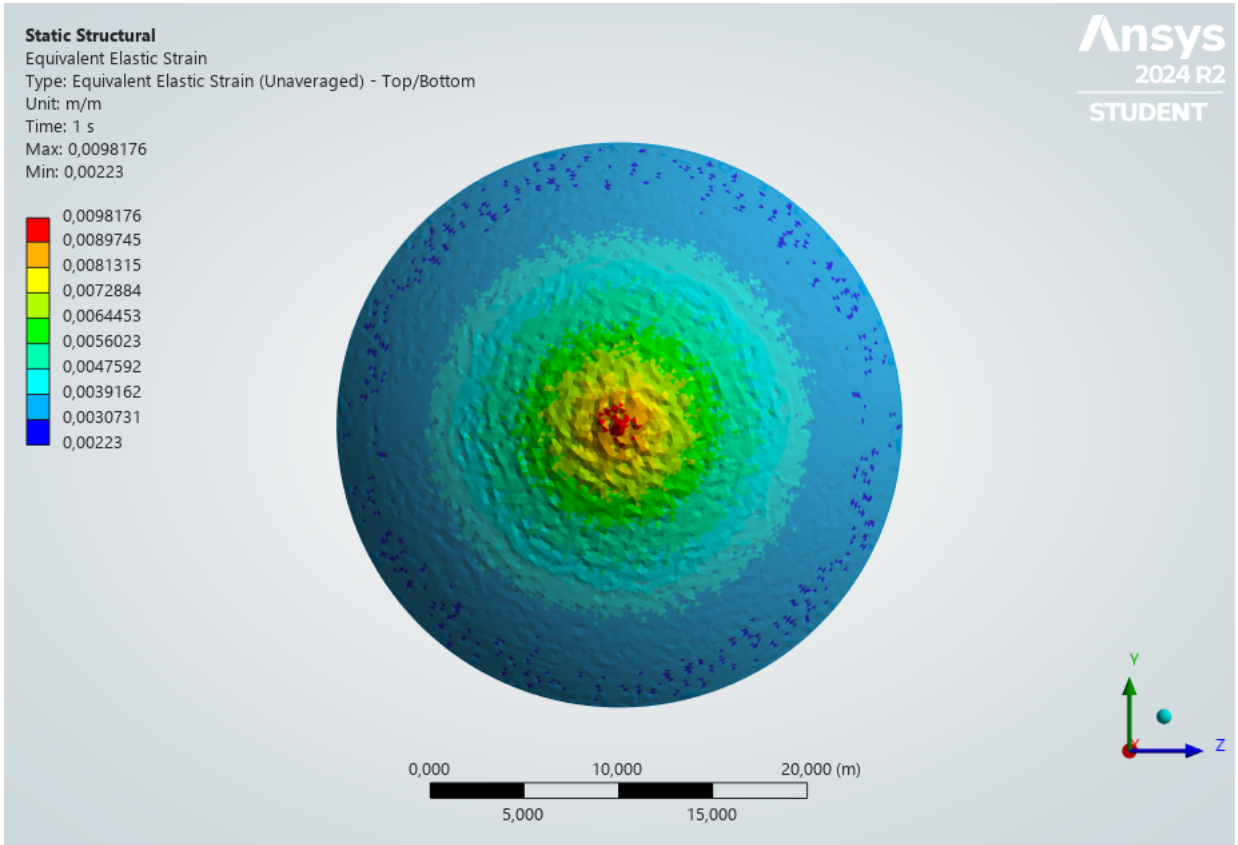

Figure 9.6 Equivalent Elastic Strain in Hot case – Reflector

The maximum elastic strain value is relative to the maximum stress value (mechanical) in the central point of the reflector section, with a value of 0,98%.
Considering the high temperature, the thermal strain component is computed as follows:

$$\varepsilon_{\mathrm{temp_{hot}}} = \alpha\Delta T = 1{,}7 * 10^{-5}(85 - 25) = 1{,}02 * 10^{-3}$$

Which is a 0,102% strain value in percentage. The highest value of strain, considering both thermal and mechanical stress is:

$$\varepsilon_{\mathrm{tot_{hot}}} = 1{,}08\%$$

The overall deformation of the antenna was consistent with the expected behavior of the structure under inflation. The reflector maintained its parabolic shape, ensuring optimal reflective performance. The canopy, designed for transparency and support, exhibited minimal deformation, confirming its structural integrity and compatibility with the reflective section.

Critical Zone Assessment
The simulation highlighted several zones requiring careful consideration.
The central point of the reflective section showed localized stress peaks, warranting further investigation to ensure long-term durability.
The second critical zone is the edge of the canopy, where the material transitions between layers, displayed slightly higher strain values, indicating the need for precise manufacturing tolerances to maintain performance.

9.5. Simulation Results Cold Case

The structural simulation results provided valuable insights into the performance of the inflatable antenna under the operational conditions defined in the study. The analysis' results for the cold case with an inflation pressure of 6,25 Pa, are showed in the following pictures:
Equivalent Von Mises Stress distribution results

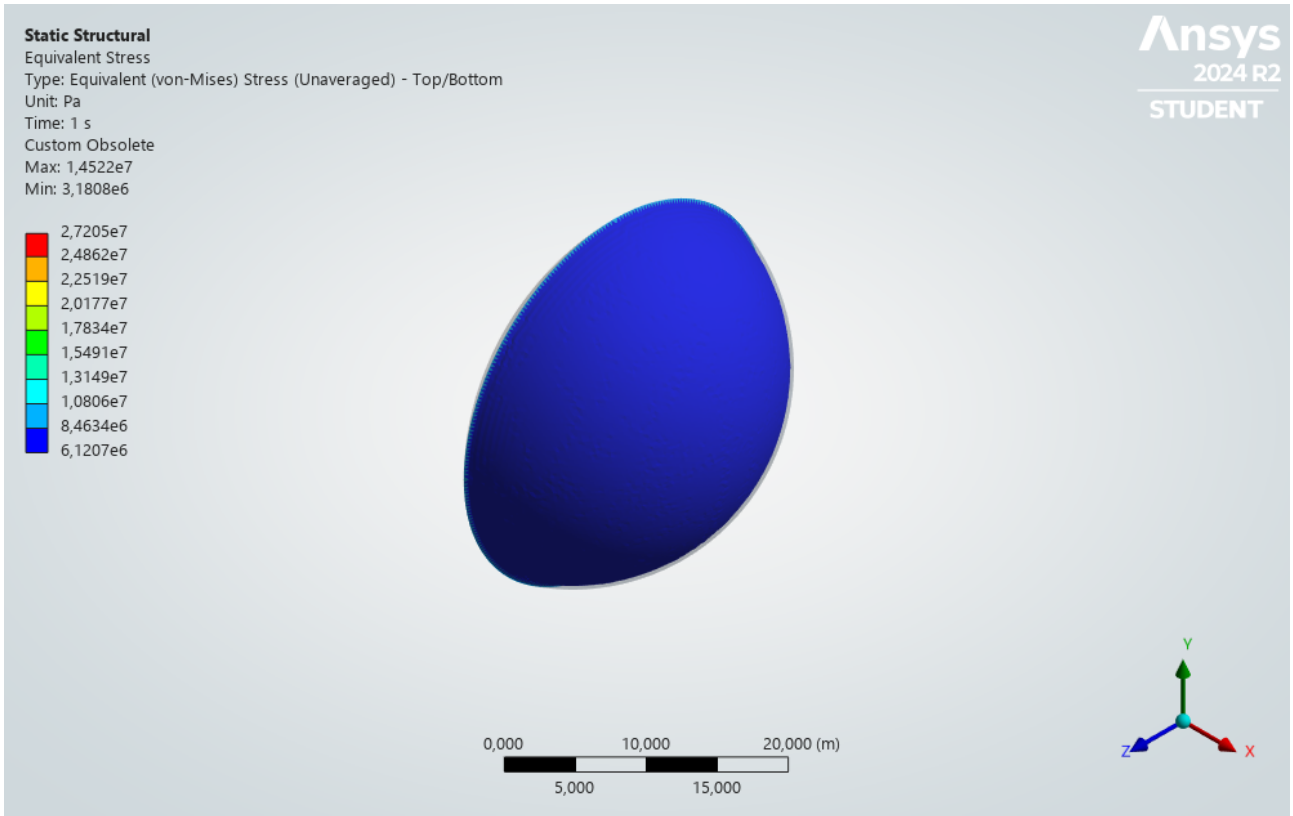

Figure 9.7 Equivalent Von Mises stress distribution in Cold Case – Isometric view of canopy

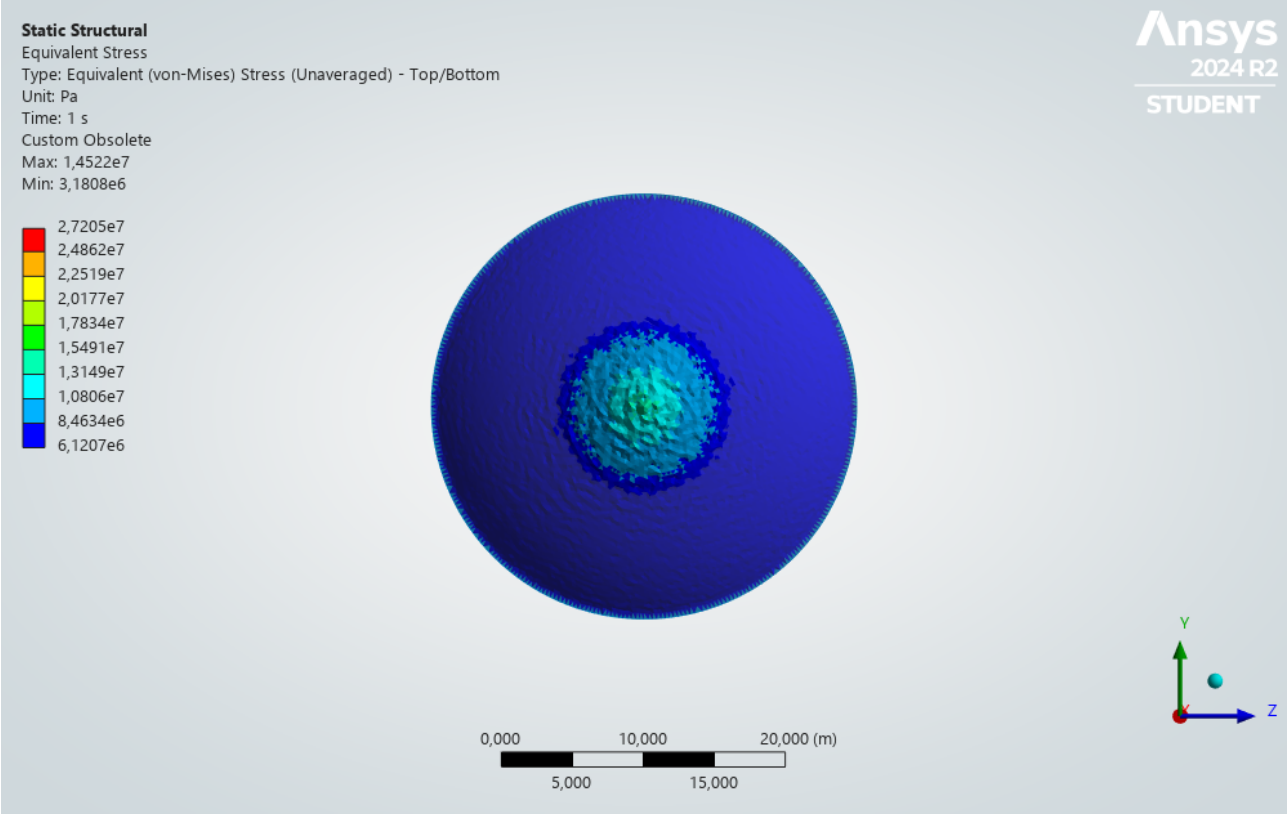

Figure 9.8 Equivalent Von Mises stress distribution in Cold Case – Reflector

Also, for the case in which the antenna faces a temperature of 188 K (-85 °C), the results have demonstrated that the line pressure applied by the Z ring during balloon motion is negligible respect to the stress generated on membrane by inflation pressure. Furthermore, applying an inflation pressure of 6,25 Pa, the maximum stress is significantly lower than the other case. The highest stress value, corresponding to 14,52 Mpa, is reached on the central point of the reflector section of the antenna.

Equivalent Elastic Strain distribution results

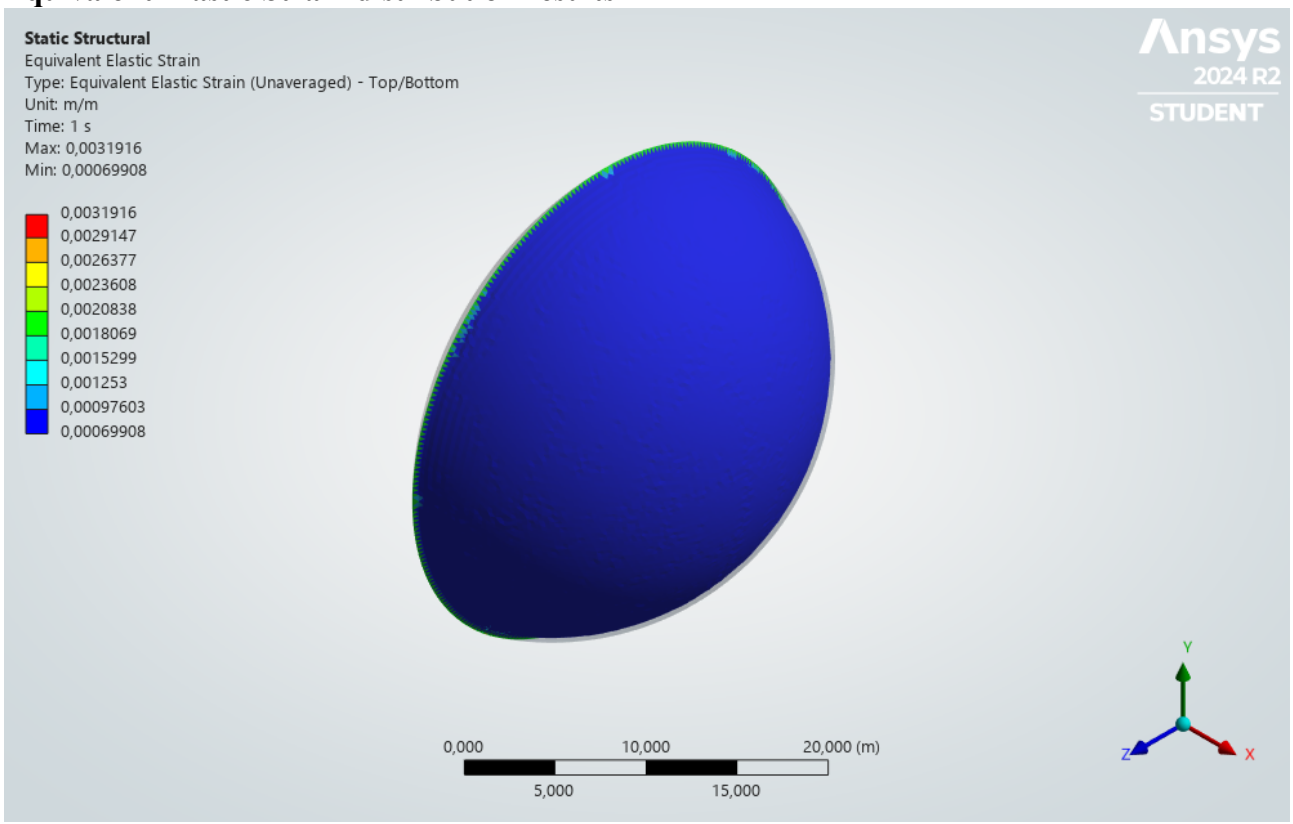

Figure 9.9 Equivalent Elastic Strain in Cold case – Canopy

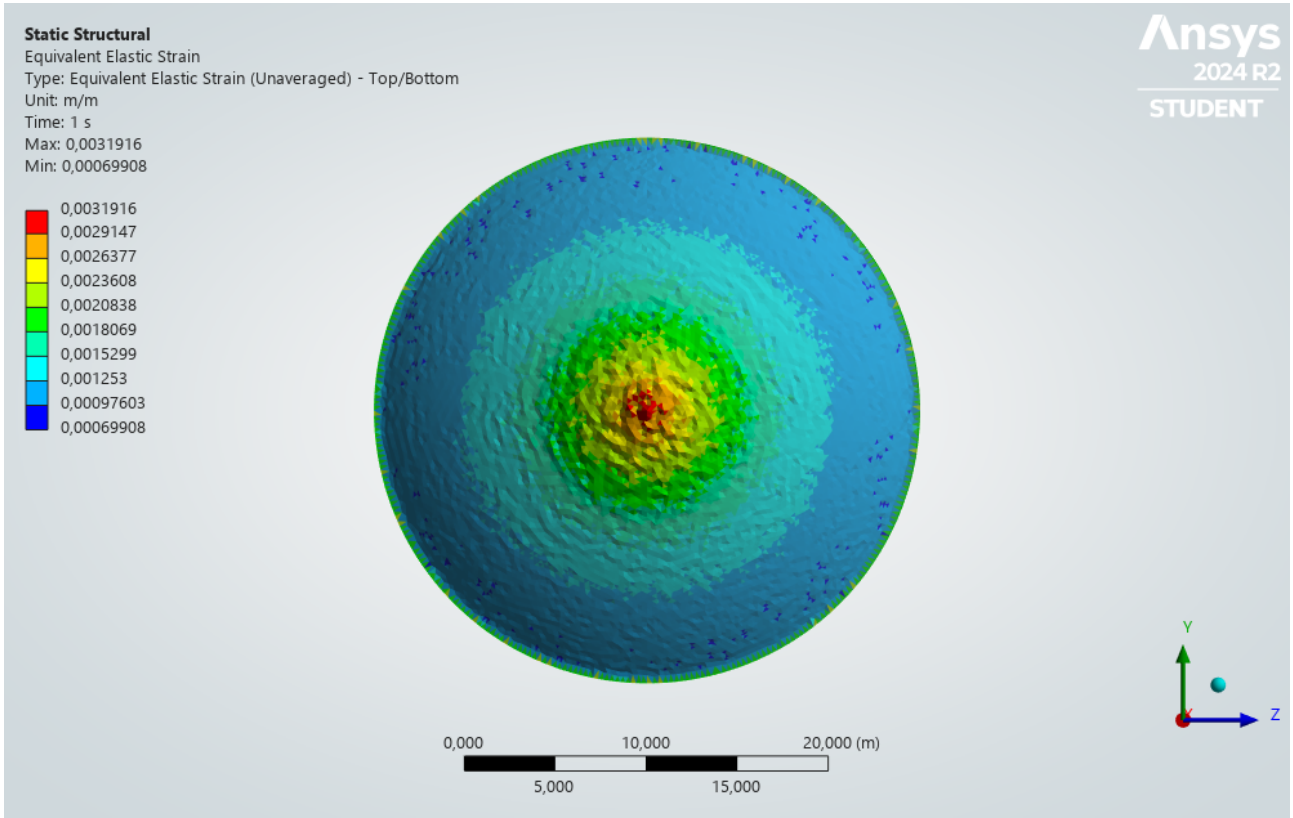

Figure 9.10 Equivalent Elastic Strain in Cold case – Reflector

The maximum elastic strain value is relative to the maximum stress value in the central point of the reflector section, with a value of 0,32%.
Considering the low temperature, the thermal strain component is computed as follows:

$$\varepsilon_{\mathrm{temp_{hot}}} = \alpha\Delta T = 1{,}7 * 10^{-5}(-85 - 25) = -1{,}87 * 10^{-3}$$

Which is a -0,187% strain value in percentage. This negative value decreases the strain generated by mechanical loads.
The highest value of strain, considering both thermal and mechanical stress is:

$$\varepsilon_{\mathrm{tot\_cold}} = 0{,}13\%$$

Also for this case, the overall deformation of the antenna was consistent with the expected behavior of the structure under inflation. The reflector maintained its parabolic shape, ensuring optimal reflective performance. While the canopy exhibited minimal deformation, confirming its structural integrity and compatibility with the reflective section.
In conclusion, the critical zone assessment is the same of the previous case, due to a similar behavior of the structure under different load condition.

Conclusion
The structural analysis conducted demonstrates the mechanical viability under the operational conditions anticipated in orbit. Simulations were performed to evaluate the behavior of the structure under inflation pressure and thermal variations, focusing on the hot and cold cases. The results were compared with the maximum allowable stress and strain values to verify the compliance of the design with the material's limitations.

For the hot case, with a temperature of 85°C, the maximum Von Mises stress was determined to be 27,88 MPa, slightly below the allowable stress limit of 30.32 MPa. The strain values also remained within the elastic range, confirming the structural stability of the material under these conditions. Even though, the train value of 1,08% is slightly below the allowable limit ($\varepsilon_{\mathrm{allow}} = 1{,}14\%$), the situation is not critical since has been adopted a safety factor of 2. The thermal strain, resulting from the expansion due to temperature, was included in the analysis to ensure a realistic assessment of the antenna's behavior.

In the cold case, corresponding to -85°C, the maximum von Mises stress reached 14,52 MPa, remaining well within the allowable limit of 42.02 MPa. The strain values were similarly evaluated. With a total strain value of 0,13%, the safety limit of 0,92% is respected confirming that the material maintained its elastic behavior even at low temperatures.
The analysis confirmed that the selected material configuration can withstand the combined effects of mechanical and thermal loads. Stress distribution across the structure was largely uniform, with minor concentrations near critical points such as the traction/compression ring, which were within acceptable limits.

10. Preliminary Thermal analysis of an orbiting balloon

For most spacecrafts, heat balance is the dominant factor in the thermal design. For simplicity, most mission scenarios are initially assumed to be in a steady-state energy balance. Balance is achieved when all the heat sources on a spacecraft are equal to the heat lost to space. Heat sources include external environmental inputs and internal heat generation. The heat balance for a typical spacecraft can be estimated as follows.

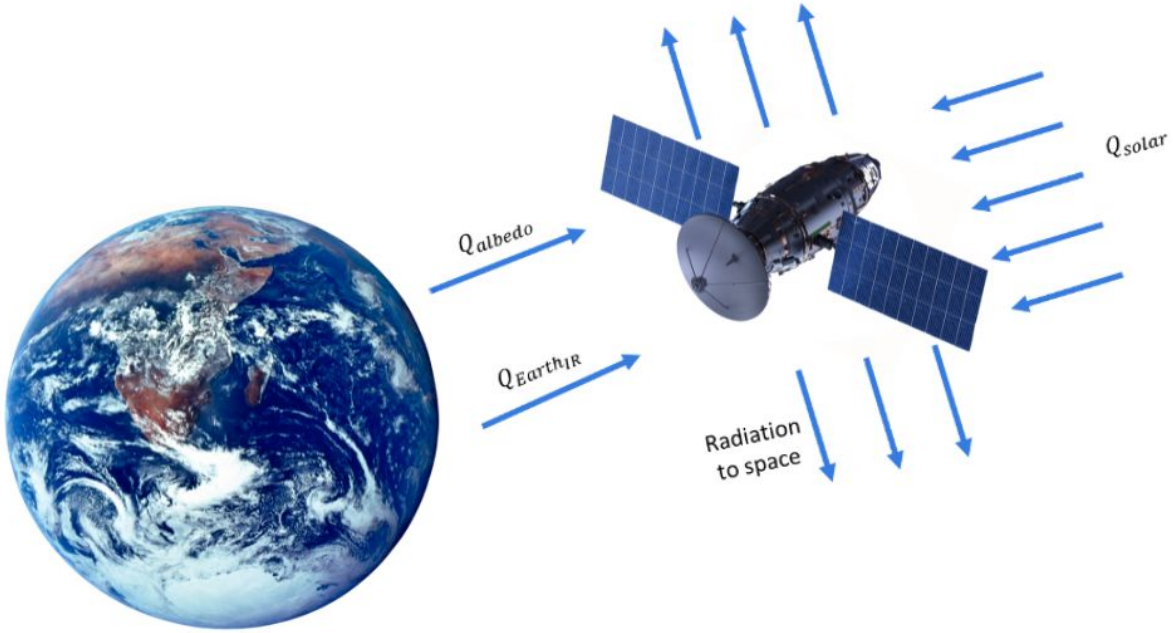

Figure 10.1 Antenna thermal environment

From a generalized heat balance equation:

$$Q_{in} = Q_{out}$$
$$Q_{external} + Q_{internal} = Q_{radiatior} + Q_{MLI} \qquad (10.1)$$

Where $Q_{external}$ is the environmental heat absorbed, $Q_{internal}$ is the power dissipation, $Q_{radiator}$ is the heat rejected from the spacecraft primary radiator surfaces, and Q_{MLI} is the heat lost from blankets and elsewhere on the spacecraft.
To simplify the hot case calculation, it can conservatively assumed that the net Q_{MLI} is negligible, so $Q_{external}$ becomes the flux absorbed by the radiators only. For an individual radiator:

$$Q_{external} + Q_{internal} = Q_{radiator}$$

Substituting $Q_{radiator}$ and $q_{external}A$ for $Q_{external}$ the radiator heat balance becomes:

$$Q_{internal} + q_{external}A = \varepsilon\sigma AT^4 \qquad (10.2)$$

where $Q_{internal}$ is the internal spacecraft heat, $q_{external}$ is the external environmental heat load on the radiator per unit area, A is the area perpendicular at flux, ε is the radiator emittance, σ is the Stefan-Boltzmann constant (5.67051 x 10^{-8} W/m^2K^4), and T is the radiator temperature. [8]
The external environmental load, $q_{external}$ can be broken down into the following individual heat loads:

$$q_{external} = q_{solar} + q_{albedo} + q_{Earth_{IR}} \qquad (10.3)$$

where q_{solar} is the absorbed solar load per unit area, q_{albedo} is the absorbed heat load per unit area and $q_{Earth_{IR}}$ is the absorbed Earth IR heat load per unit area.
To size a radiator, one must calculate a value for each of the terms in the last equation. The solar term, q_{solar} con be considered a constant value equal to 1367 W/m^2. Earth IR and albedo loads per unit area, $\sigma_{Earth_{IR}}$ and σ_{albedo} can be calculated using the following:

$$q_{Earth_{IR}} = \varepsilon I_{EIR} F_{EIR} \qquad (10.4)$$
$$q_{albedo} = \alpha I_{solar} \rho_{albedo} F_{albedo} \qquad (10.5)$$

where α and ε are the absorptivity and emissivity of the radiator, I_{EIR} and I_{solar} are the intensity of the Earth IR and solar fluxes, and ρ_{Albedo} is the Earth's albedo. Suggested hot and cold case values for these parameters are shown in Table 10.1. The remaining terms, F_{EIR} and F_{albedo} are geometrical factors that account for the direction of the radiator relative to the Earth and Sun.

Table 10.1 Parameter value for thermal analysis [6]

PARAMETER	HOT CASE	COLD CASE
SOLAR CONSTANT $\left[\frac{W}{m^2}\right]$	1420	1360
ALBEDO	0.30	0.23
IR $\left[\frac{W}{m^2}\right]$	244	218
SOLAR ABSORPTANCE	Maximum	Minimum
IR EMITTANCE	Minimum	Maximum
MYLAR-AL ABSORPTANCE	0.17	0.11
MYLAR-AL EMITTANCE	0.76	0.83
POWER DISSIPATION	Maximum	Minimum

Hot case:

$$\varepsilon\sigma AT^4 = Q_{internal} + \left(q_{solar} + q_{Albedo} + q_{Earth_{IR}}\right)$$

With $F_{albedo} = 0.4904$, $F_{Earth_{IR}} = 0.5883$ and power dissipation, taking account a current of 10 A on each ring and the electronic consumption on the satellite, equal to 50 W:

$$T = 358.40 \text{ K}$$

Cold case

$$\varepsilon\sigma AT^4 = Q_{internal} + q_{Earth_{IR}}$$

With $F_{Earth_{IR}} = 0.5883$ and a power consumption of 10 W, taking account only the telemetry and survival system:

$$T = 188.64 \text{ K}$$

Once the temperature of the satellite is evaluated, it is possible to determine the pressure that the gas contained within the sphere exerts on the surface of the spacecraft:

$$p = \frac{MRT}{V}$$

Considering 2 kg of Air, M, for air R is equal 287 J/kgK and a volume, V, equals to 3913.04 m^3:

- In hot case, with a temperature of 359.39 K the pressure is equal to:

$$p = 2 * 287 * \frac{358.40}{3913.04} = 52.57 \text{ Pa}$$

- In cold case, with a temperature of 188.63 K the pressure is equal to:

$$p = 2 * 287 * \frac{188.63}{3913.04} = 27.68 \text{ Pa}$$

11. Preliminary Power Budget analysis

This chapter exploit a preliminary power budget analysis, both in sunlight and eclipse phase. Assuming to choose an elliptical orbit with the perigee at 2000 km and the apogee to 5000 km and an inclination of 28.5 deg, the orbit period, τ, is 9771.024 s. In the worst case, the total sunlight time, τ_s, is about 7058.763 s and the eclipse time, τ_e, is 2712.261 s, with a ratio eclipse to orbital period to 19.02 %.
With a power consumption in eclipse, P_e, of 10 W and considering a safety factor of 2, the total consumption in equal to 20 W. The total energy needed in eclipse phase is equals to:

$$E_{eclipse} = P_e \tau_{eclipse} = 20 * 2712.261 = 54.25 \text{ kJ} \qquad (11.1)$$

In sunlight phase, it can be assumed a power consumption, P_s, of 50 W. With a safety factor 2 the total power consumption is equal to 100 W. In this way:

$$E_{sunligth} = P_s \tau_s = 100 * 7058.763 = 705.88 \text{ kJ} \qquad (11.2)$$

The energy consumption, E_{tot}, in an orbital period is equal to:

$$E_{tot} = E_{sunlight} + E_{eclipse} = 760.13 \text{ kJ}$$

The solar array power, P_{SA}, needed to feed the satellite power consumption is about:

$$P_{SA} = \frac{E_{tot}}{\tau_{sunligth}} = \frac{760.13}{7058.763} = 107.69 \text{ W} \qquad (11.3)$$

With a solar array yield of 12%, η_{SA}, a degradation coefficient for years, I_d, equals to 2.35% and a solar power of 1367 W/m^2, the total area needed is about:

$$A_{SA} = P_{SA} * \frac{(1+I_d)^y}{I_{solar}\eta_{SA}} = \frac{107.69*(1+0.0235)^2}{1367*0.12} = 0.69 \text{ m}^2 \qquad (11.4)$$

The specific solar array power, P_{kg}, is in range from 25 to 200 $\frac{W}{kg}$, in this way with:

$$m_{SA} = \frac{P_{SA}}{P_{kg}}(1 + I_d)^y = \frac{107.69}{25}(1 + 0.0235)^2 = 4.51 \text{ kg} \qquad (11.5)$$

The use of a solar array needs the utilization of a battery to storage the power needed for the solar eclipse. For this application, the energy needed in the eclipse period is equals to:

$$E_{eclipse} = 54.25 \text{ kJ} = 15.07 \text{ Wh}$$

For an operative time, OT, of 2 years, the total life cycle, L_c, is equals to:

$$L_c = \frac{OT(s)}{\tau} = \frac{62208000}{9771.024} \approx 6367 \qquad (11.6)$$

In Figure 11.1, can compute the battery deep of discharge, DOD, that for a life cycle of 8162 and a Nickel Cadmium battery is approx. 50%.

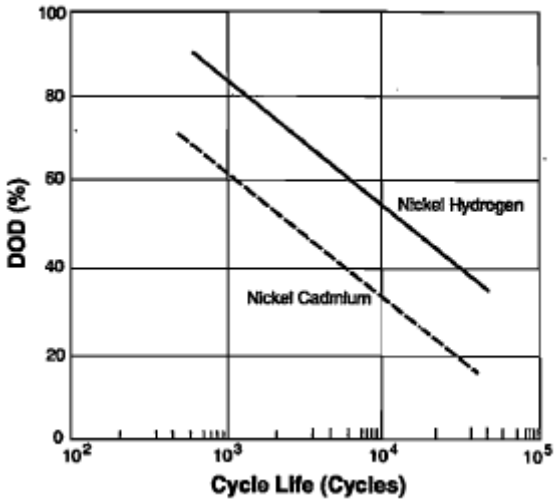

Figure 11.1 Depth-of-Discharge vs. Cycle Life for Secondary Batteries [8]

In this way, the total battery power, $E_{battery}$, needed is equals to:

$$E_{battery} = \frac{E_{eclipse}}{DOD} = \frac{15.07}{0.5} = 30{,}14 \text{ Wh} \qquad (11.7)$$

With a specific energy, $E_{battery_w}$ of $30 \frac{Wh}{kg}$ the total battery pack weight, $m_{battery}$, is:

$$m_{battery} = \frac{E_{battery}}{E_{battery_w}} = \frac{30.14}{30} = 1.00 \text{ kg} \qquad (11.8)$$

Final Consideration

By selecting an orbit that ensures continuous exposure to sunlight, the need for onboard batteries can be effectively eliminated. This approach offers multiple benefits, including a significant simplification of the power management architecture and a reduction in the overall complexity of the electronic control systems. Furthermore, it enhances reliability by minimizing the number of critical components subject to degradation over time.

12. Solar arrays for inflatable structures

Solar Arrays as a Power Source for the Inflatable Antenna

The deployment and operation of the inflatable antenna in space necessitate a reliable and efficient energy source for its subsystems, including communication devices, inflation mechanisms, and structural monitoring sensors. Solar arrays present an ideal solution for generating power in space due to their high efficiency, scalability, and proven performance in numerous space missions. This chapter explores the integration of solar arrays into the inflatable antenna system, analyzing their feasibility, challenges, and potential configurations. The discussion concludes with the recommendation of the most suitable approach to meet the mission's energy requirements effectively.
These arrays typically consist of photovoltaic cells that convert sunlight into electrical energy.
Inflatable structures, such as the antenna in this mission, introduce unique challenges due to their large surface areas, thin material layers, and sensitivity to mechanical and thermal stresses. The integration of solar cells onto such a structure must ensure that the antenna's primary functions, such as signal reflection and rigidity, are not compromised.

Analysis of Solar Array Placement

The placement of solar arrays can significantly influence the performance and reliability of the system. Two primary configurations are considered: integrating solar cells onto the antenna surface (reflector section) and attaching them to the CubeSat supporting the antenna.

Solar Cells on the Antenna Surface

Integrating solar cells directly onto the antenna's surface offers the advantage of utilizing its large area. Flexible and ultra-lightweight solar cells, such as thin-film technologies, are particularly suited for this purpose. These cells can be adhered to the reflective and transparent sections of the antenna without significantly increasing its mass or altering its mechanical properties. To ensure the functionality of the antenna, consider placing solar array onto the outer surface of the reflective section.
However, this approach presents several challenges. The orientation of the antenna may not always align optimally with sunlight, particularly if the antenna must prioritize communication or scientific objectives. Additionally, the presence of solar cells may interfere with the antenna's reflective properties, especially on the parabolic reflector's surface. The mechanical stresses during inflation and rigidization also pose risks to the adhesion and integrity of the solar cells, necessitating careful material selection and robust testing under simulated space conditions.
This solution will require to test again the material stress distribution among the structure and an inflation pressure reduction may be necessary.

Solar Cells on the CubeSat

Positioning solar arrays on the CubeSat provides an independent and reliable power source for the antenna system. The CubeSat can be equipped with deployable solar panels that maximize energy collection by orienting themselves toward the Sun. This configuration avoids the risks associated with integrating solar cells onto the antenna and simplifies its structural design.

However, relying solely on the CubeSat for power generation introduces the challenge of energy transmission to the antenna. This could be achieved through lightweight tethers or wireless power transfer methods such as inductive coupling or microwave beaming. While these methods are

technically feasible, they add complexity to the system and may introduce energy losses during transmission.

Proposed Hybrid Approach

A hybrid approach is proposed to leverage the advantages of both configurations while mitigating their limitations. In this approach, the CubeSat serves as the primary power generator, equipped with deployable solar panels that provide most of the energy required for the antenna system. Simultaneously, lightweight solar cells are integrated onto specific areas of the antenna, such as non-critical sections of the reflector, to serve as supplementary energy sources.

This configuration offers several benefits. The CubeSat's independent power generation ensures a reliable energy supply, while the supplementary solar cells on the antenna provide redundancy and additional power during high-demand phases. The integration of solar cells on the antenna can also contribute to thermal regulation by absorbing sunlight in specific areas, reducing thermal gradients across the structure.

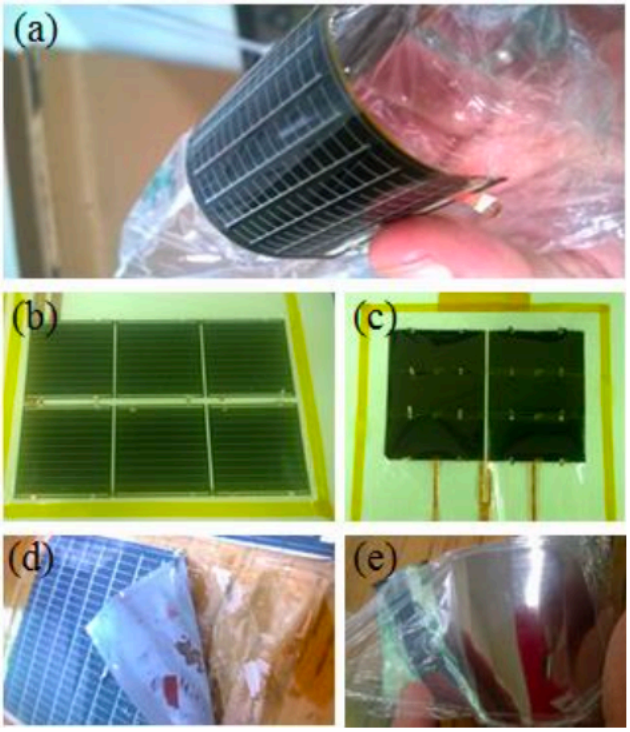

Figure 12.1 (a) Generation II LISA-T material assembly. (b) CIGS based sub-coupon. (c) IMM based sub-coupon. (d) PV bonded via adhesive and (e) PV bonded without adhesive. [34]

Figure 12.1 illustrates the development and characteristics of second-generation photovoltaic (PV) assemblies designed for space applications. These assemblies are fabricated using covered PV cells bonded to a 3 µm toughened colorless polyimide (TCP1) substrate via an innovative adhesive-less joining method. The images describe two types of generation II assemblies and provide a comparison between adhesive and adhesive-less bonding techniques.

Figure 12.1b, showcases a low-cost (about $20/W), moderate-performance copper indium gallium selenide PV cell with 9-11% power conversion efficiency under AM0 conditions (air mass zero solar spectrum). While originally intended for terrestrial use, these cells show promising potential for low Earth orbit (LEO) missions.

While, Figure 12.1c represents a higher-performance option using an inverted metamorphic (IMM) cell with a typical cost of $350/W and a PCE of 25-30% under AM0 conditions.
Both configurations feature CORIN XLS polyimide as a cover material. This optically clear polyimide offers exceptional stability under radiation and resistance to atomic oxygen erosion, making it well-suited for the harsh space environment. [34]

Implementation Considerations

The successful implementation of this hybrid approach requires careful attention to material selection, energy management, and structural integration. Flexible solar cells must be compatible with the antenna's materials, such as Mylar and silicon dioxide coatings, to ensure secure adhesion and durability. Thermal management systems must be designed to handle the heat generated by the solar cells and prevent localized overheating.
The CubeSat's solar panels should be designed to maximize efficiency while minimizing mass and stowage volume. Deployable panels with automated tracking systems can optimize energy collection throughout the orbit. For energy transmission, lightweight tethers provide a straightforward solution, though wireless transfer technologies may offer greater flexibility for future iterations of the design.

Conclusion

The integration of solar arrays into the inflatable antenna system represents a critical step in ensuring its operational success. The hybrid approach proposed in this chapter provides a balanced solution that combines the reliability of CubeSat-based power generation with the additional benefits of supplementary solar cells on the antenna. This configuration maximizes energy efficiency, enhances redundancy, and maintains the structural integrity of the antenna. By addressing the challenges of material compatibility, thermal management, and energy transmission, this approach demonstrates the feasibility of solar-powered inflatable antenna systems for advanced space applications.

13. CubeSat Solution for Inflatable Antenna Deployment

13.1. CubeSat

The CubeSat is a standardized, miniaturized satellite platform that has become very used in modern space missions due to its compact size, modular design, and cost-effectiveness. Typically measuring units of 10 cm × 10 cm × 10 cm (1U) and weighing less than 1.33 kilograms per unit, CubeSats can be configured in larger sizes, such as 3U or 6U, by combining multiple units. Their versatility allows them to host a variety of payloads. CubeSats have revolutionized space missions by enabling innovative and cost-efficient approaches to research.

In the context of this mission, this spacecraft plays a pivotal role in the successful deployment of the inflatable antenna. Additionally, CubeSats offer advanced control capabilities, such as attitude control systems (e.g., reaction wheels and magnetorquers) and onboard sensors, which are essential for ensuring precise deployment and operational stability.

The CubeSat's modular design aligns seamlessly with the antenna's requirements for compact stowage and efficient deployment in orbit. Its ability to carry onboard systems for power management, communication, and navigation reduces the need for integrating these systems directly into the antenna structure, thereby simplifying its design. Moreover, its ability to act as a wireless controller for the antenna after deployment further enhances the mission's flexibility and reliability.
This chapter explores the CubeSat's role in detail, highlighting its functionality as an integral component of the mission. It discusses the methods used to integrate the CubeSat with the antenna, its role during inflation and rigidization, and the challenges and advantages associated with this approach. [35]

13.2. Characteristics of the CubeSat Deployment Method

Deployment may begin with the CubeSat stabilizing itself in orbit. This critical step is achieved through advanced attitude control systems such as reaction wheels or magnetorquers, which counteract any rotational dynamics or perturbations. Stability during this phase is essential to prevent misalignment or deformation of the antenna structure as it begins to inflate. Once stabilized, the CubeSat initiates the inflation sequence, releasing the gas at a controlled rate through precision valves. This ensures that the antenna's membrane experiences consistent and uniform pressure, avoiding localized stress concentrations that could compromise its structural integrity. This process is fast, and it usually takes seconds to be completed.

Throughout the inflation process, the CubeSat continuously monitors key parameters such as internal pressure and temperature using its sensors. These measurements are essential for maintaining the inflation process within safe operational limits, ensuring the material behaves as expected under the applied loads. Additionally, imaging systems onboard the CubeSat provide real-time visual feedback, allowing operators to verify the proper unfolding and deployment of the antenna.
The CubeSat's role extends beyond simply deploying the antenna; it also acts as a robust platform for monitoring and managing the entire process.

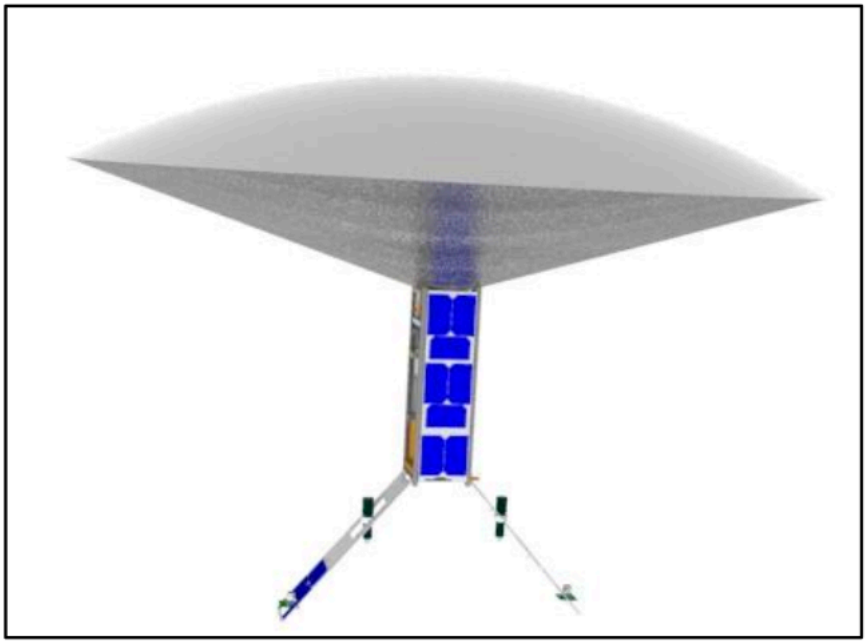

Figure 13.1 CubeSat Antenna in Deployed State for similar configuration [37]

13.3. Rigidization process with the CubeSat support

The rigidization phase represents a critical step in transitioning the inflatable antenna from its expanded state to a structurally stable configuration suitable for ensuring long lifetime of the mission. This process follows the inflation phase and ensures that the antenna maintains its designed shape and mechanical integrity under operational loads. In this application, UV curing is employed as the rigidization method, leveraging sunlight to activate a UV-curable resin integrated into the antenna's multilayer structure.

During the rigidization phase, the CubeSat may play a supporting role. While the inflation process necessitates a direct physical connection between the CubeSat and the antenna, the rigidization phase allows the CubeSat to detach and maintain a close but independent orbit near the antenna. This detachment minimizes interference and dynamic loads on the antenna during the curing process, enabling a smoother transition to rigidity.

The UV curing process begins once the antenna is fully inflated and properly oriented to receive direct sunlight. UV radiation penetrates the antenna's outer layers, activating the resin embedded within the structural materials. This resin undergoes a photochemical reaction that causes it to solidify, transforming the antenna's flexible membrane into a rigid shell.

Maintaining proximity to the antenna without physical attachment during rigidization offers several advantages. First, it eliminates the potential for dynamic interactions between the CubeSat and the antenna that could disrupt the curing process. For example, residual vibrations or thermal expansion in the CubeSat's structure could induce stress concentrations on the antenna if the two remain physically connected.

Second, the detached configuration simplifies thermal management. The CubeSat, which generates heat from its onboard systems, does not contribute to localized heating of the antenna, ensuring a uniform curing process.

Figure 13.2 Inflation of antenna sample on left, rigidization on right [37]

However, a detached CubeSat must remain sufficiently close to the antenna to fulfill its monitoring and control roles. Precise orbit determination and station-keeping capabilities are required to ensure that the CubeSat can maintain this proximity. Propulsion systems, such as micro thrusters, or attitude control mechanisms, enable the CubeSat to adjust its position and orientation relative to the antenna. The decision to detach the CubeSat during rigidization also aligns with the modularity of the mission design. By separating the two systems, the CubeSat can transition to other mission roles once the rigidization process is complete. For instance, it can serve as a communication relay or perform orbit maintenance tasks independently of the antenna. This aspect will be better discussed in the following section.
In conclusion, this configuration reduces the risk of mechanical interference and ensures uniform curing of the UV resin. Although this strategy introduces the need for precise relative orbit control, its benefits in ensuring the structural integrity and reliability of the antenna outweigh the additional complexity. [36]

13.4. Functionality of the CubeSat After Deployment

Once the inflatable antenna is successfully inflated and rigidized, the CubeSat transitions to its post-deployment functionalities, ensuring the mission's success and extending its operational capabilities. After completing its primary role in the deployment process, the CubeSat detaches from the antenna using a reliable mechanical separation system.
One of the CubeSat's primary roles, at this stage, is to act as a control and monitoring unit for the antenna. Using an advanced attitude control system, it can maintain its orientation relative to the antenna. Moreover, it can also provide critical telemetry data, monitoring the antenna's structural health, thermal performance, and alignment in real time.

In addition to its control and monitoring functions, the CubeSat can act as a communication relay, facilitating the transfer of data between the antenna and ground stations. This is especially useful if the antenna operates in a configuration that limits its ability to communicate directly with Earth.
A key innovation in this mission is the CubeSat's ability to wirelessly transfer energy to the antenna. Although this capability must be further studied, it can address the antenna's power requirements without relying on physical tethers.
Wireless energy transfer methods, such as inductive coupling or microwave beaming, can be employed. Inductive coupling involves creating a magnetic field between the CubeSat and the antenna to transmit energy over short distances efficiently. Microwave beaming, on the other hand, uses directed electromagnetic waves to deliver power across larger gaps.

Another main function of the CubeSat is controlling the movements of the inflatable antenna by wirelessly transmitting signals to regulate the current flow within the antenna's structural elements, such as conductive circuits or rings. The CubeSat's onboard control unit calculates the required

current adjustments based on the desired movement or alignment of the antenna. These control commands are transmitted wirelessly, typically using radio frequency communication.
The antenna is equipped with conductive pathways or actuators designed to respond to changes in current flow. By modulating the current, the CubeSat induces electromagnetic forces within the antenna's structure, enabling precise movements or torque generation. This mechanism allows the antenna to adjust its orientation, maintain stability, or realign for optimal operation, such as targeting a ground station or maintaining its structural integrity in orbit.
This data is transmitted back, creating a closed feedback loop. The CubeSat processes this feedback to refine its control commands in real time, ensuring stable and precise adjustments to the antenna's movements.

Conclusion

The CubeSat-based deployment approach offers a practical and efficient solution for the inflatable antenna. Its ability to integrate the inflation system and manage the rigidization process ensures a reliable transition from stowed to operational configuration. This method also simplifies the antenna's structural design by externalizing key functionalities, such as gas storage and control. However, further studies and rigorous testing are required to validate this approach, particularly under simulated space conditions. Challenges such as dynamic stability during inflation, thermal management, and separation reliability must be addressed through additional analysis and experimental validation.

14. Conclusions

This work has presented a preliminary feasibility study concerning the development of an ultra-light inflatable antenna intended for deployment in Low Earth Orbit. The research investigated an innovative approach to orientation control based on the interaction between electric currents flowing through conductive elements integrated within the antenna structure and the Earth's magnetic field. This method enables actuation without conventional mechanical systems, thereby significantly reducing complexity, mass, and deployment constraints.

A comprehensive material selection process identified aluminized Mylar coated with silicon dioxide as the most suitable candidate, offering an excellent balance of mechanical flexibility, space environmental resistance, and minimal mass. Gas inflation was selected for its simplicity, reliability and compatibility with mission constraints. To ensure long-term structural integrity and resistance to micrometeoroid impacts, a UV curing rigidization strategy was proposed, leveraging solar ultraviolet radiation in orbit to transition the membrane into a self-supporting configuration. Moreover, the use of Origami folding technique for the stowage of the inflatable antenna mitigates the risk of wrinkle formation during the deployment phase.

Two geometric configurations of the parabolic reflector were assessed, characterized by different focal length-to-diameter (F/D) ratios. The configuration with F/D = 0.38 demonstrated superior performance in terms of reduced mass, volume, and resistive losses—making it the most favorable solution from a system efficiency and launch cost perspective.

A central aspect of this study was the development and preliminary validation of a control methodology to ensure accurate antenna orientation. By modulating electric currents within conductive rings, the antenna can be precisely oriented through electromagnetic torques according to Lorentz's Law. Dedicated simulations were performed to investigate the relationship between applied current and maneuver time under various magnetic field conditions. The results confirm that this approach enables controlled, power-efficient alignment of the antenna with acceptable settling times, particularly in LEO conditions.

Thermal and structural analyses confirmed the viability of the proposed design, with the selected materials and geometry proving stable under the extreme environmental conditions encountered in orbit. Additionally, the integration of lightweight photovoltaic solutions—either directly on the membrane or via auxiliary CubeSat—was considered to ensure sufficient power supply during operation. In conclusion, the findings of this thesis demonstrate the technical feasibility and potential of the proposed inflatable antenna system for a broad range of space applications, including radio astronomy, deep-space communications, and orbital energy transmission. While the results are promising, further experimental validation, prototyping, and in-orbit testing will be required to transition from conceptual design to fully operational systems.

Aknowledgments

Giunto al termine di questo importante percorso accademico, sento il dovere e il desiderio di esprimere la mia più profonda gratitudine a tutte le persone che, a vario titolo, hanno contribuito al raggiungimento di questo traguardo.

Desidero innanzitutto ringraziare i miei relatori, la Prof.ssa Raffaella Sesana ed il Prof. Ladislau Matekovits per la disponibilità, la competenza e il prezioso supporto offerto durante la stesura di questa tesi. La loro guida ha rappresentato un punto di riferimento importante, permettendomi di approfondire questa tematica con il giusto rigore.
Il pensiero più sentito va alla mia famiglia. A voi devo tutto. Grazie per l'amore incondizionato, per il sostegno nei momenti più difficili e per aver sempre creduto in me, anche quando io stesso facevo fatica a farlo. Durante questo percorso, ci sono stati diversi momenti in cui ho pensato di mollare, grazie a voi ho trovato la forza di proseguire e concludere questo cammino.

Un ringraziamento speciale va ai miei amici dell'aula studio Gianluca, Paola, Yab, Arianna, Bianca, Francesco, Simone e tanti altri con cui ho condiviso ore interminabili di studio, confronto e risate. Insieme abbiamo affrontato sfide quotidiane, e la vostra compagnia ha reso questo cammino più leggero e piacevole. Ringrazio anche i miei coinquilini Andrea, Fabio e Rei per avermi sopportato e supportato durante gli anni trascorsi a Torino, abbiamo condiviso tanti bei momenti insieme e ve ne sarò per sempre grato.
Ai miei amici tutti, grazie per esserci stati. E un grazie dal profondo del cuore a Simone, Fabiano, Antonio e Alessia. La vostra vicinanza, la vostra lealtà e la vostra capacità di ascoltare senza giudicare mi hanno sostenuto più di quanto possiate immaginare. Questo traguardo è anche vostro.

Non posso non rivolgere un pensiero carico di riconoscenza a Marco, per il suo inestimabile aiuto e per l'incoraggiamento sincero che mi ha accompagnato durante gli ultimi esami. Il suo supporto ha fatto la differenza, in un momento in cui ne avevo davvero bisogno.
Ringrazio anche tutti i professori e tutte le persone che ho avuto il piacere di incontrare in questi anni, sia nel bene che nel male ho avuto modo di imparare lezioni importanti che hanno contribuito fortemente alla mia crescita. Se sono diventato ciò che sono oggi è anche grazie a voi.

Un pensiero colmo d'amore va a mia nonna Rosa, che purtroppo non è più con noi. La sua dolcezza, la sua saggezza e il suo esempio continuano a vivere in me. A lei dedico con commozione questa tesi, come simbolo di un traguardo che avrebbe voluto vedere con i suoi occhi, ma che spero possa sentire con il cuore. Come diceva sempre, bisogna andare avanti a testa alta, con Forza e Coraggio.

Infine, voglio ringraziare me stesso per essere riuscito a superare gli innumerevoli ostacoli che si sono presentati duranti questi anni di studio. Questo percorso è stato sicuramente impegnativo, ma proprio attraverso le difficoltà si ha la possibilità di crescere e diventare una persona migliore. D'altronde, per ottenere ciò che non si è mai ottenuto, si deve fare qualcosa che non si è mai fatto.

Bibliography

[1] G. D. Krebs, “Echo1,1°,” *Gunter’s Space Page*, 2024.
URL: https://www.nasa.gov/centers/langley/about/project-echo.html.

[2] C. Staugaitis and L. Kobren, “Mechanical and Physical Properties of the Echo II Metal-Polymer Laminate (NASA TN D-3409),” NASA Goddard Space Flight Center, 1966.

[3] R. Schilizzi, B. Burke, R. Booth, R. Preston, P. Wilkinson, J. Jordan, E. Preuss, and D. Roberts, “The Quasat Project,” *Proc. Int. Astron. Union*, vol. 110, p. 407, Jan. 1984.

[4] R. A. Massom, A. Worby, V. Lytle, T. Markus, I. Allison, T. Scambos, H. Enomoto, T. Tamura, K. Tateyama, T. Haran, *et al.*, “ARISE (Antarctic Remote Ice Sensing Experiment) in the East 2003: validation of satellite-derived sea-ice data products,” *Ann. Glaciol.*, vol. 44, pp. 288–296, 2006.

[5] R. R. Bate, D. D. Mueller, and J. E. White, *Fundamentals of Astrodynamics*. Dover Publications Inc., 1971.

[6] J. H. Henninger, *Solar Absorptance and Thermal Emittance of Some Common Spacecraft Thermal-Control Coatings*, NASA Scientific and Technical Information Branch, 1984.

[7] P. Mazzoldi, M. Nigro, and C. Voci, *Fisica Vol. II*, 2nd ed. Napoli: EdiSES, 2021.

[8] W. J. Larson, *Space Mission Analysis and Design*, Microcosm Press, 1992.

[9] G. Perona, A. R. Meo, M. Allegretti, I. Bordi, E. Marengo, B. Mazzetti, and M. Scovazzi, “A new class of orbiting very large ultra-light orientable MW antennas in low Earth orbits,” 2023.

[10] B. S. Munjal, “Challenges in Spacecraft Reflector Technologies–A Few Potential Applications of Smart Materials,” *Academia.edu*, 2014.

[11] M. Schenk, S. G. Kerr, and A. M. Smyth, “Inflatable cylinders for deployable space structures,” *Proc. 1st Conf. Inflatable Structures*, 2013.

[12] B. Duan, “Large spaceborne deployable antennas (LSDAs) - a comprehensive summary,” *Chinese J. Electronics*, 2020.

[13] M. Chandra, S. Kumar, and S. Chattopadhyaya, “A review on developments of deployable membrane-based reflector antennas,” *Adv. Space Res.*, 2021.

[14] B. F. Dorfman, “Toward inflatable structures with functional phase transitions: An up-to-date review with a view of potentials,” *Recent Patents on Space Technology*, 2012.

[15] M. Schenk, A. D. Viquerat, and K. A. Seffen, “Review of inflatable booms for deployable space structures: Packing and rigidization,” *J. Spacecraft Rockets*, 2014.

[16] M. Vasile, G. Tibert, and T. Sinn, “Design and development of a deployable self-inflating adaptive membrane,” in *Proc. 53rd AIAA/ASME/ASCE/AHS/ASC Structures, Structural Dynamics and Materials Conf.*, 2012.

[17] R. E. Freeland, G. D. Bilyeu, G. R. Veal, and M. M. Mikulas, “Inflatable Deployable Space Structures Technology Summary,” in *Proc. IAF-98-1.5.01*, Jet Propulsion Lab, L’Garde Inc., Univ. of Colorado, 1998.

[18] L. Urbinati, *Inflatable Structures for Space Applications*, M.Sc. Thesis, Politecnico di Torino, 2020.

[19] R. S. Pappa, J. O. Lassiter, and B. P. Ross, “Structural Dynamics Experimental Activities in Ultra-Lightweight and Inflatable Space Structures,” NASA Langley Research Center, NASA Marshall Space Flight Center, NASA Goddard Space Flight Center, 2001.

[20] ILC Dover and L’Garde, Inc., “Inflatable Space Structures,” in *Proc. IAC 04 IAF I.1.10*, 2004.

[21] D. P. Cadogan and S. E. Scarborough, “Rigidizable Materials for Use in Gossamer Space Inflatable Structures,” in *Proc. AIAA Gossamer Spacecraft Forum*, Apr. 16–19, 2001.

[22] A. Chandra, P. T. Pat, and C. Walker, “CATSAT: A 6U Inflatable Antenna Technology Demonstration Mission,” *Proc. 36th Annual Small Satellite Conf.*, Univ. of Arizona, 2022.

[23] C. Vertegaal and M. Bentum, “Feasibility Study of Inflatable Antennas as Observational Antenna for Ultra Low Frequency CubeSat Applications,” 2020.

[24] A. Chandra, *Inflatable Parabolic Reflectors for Small Satellite Communication*, Master’s Thesis, Arizona State University, 2015.

[25] J. C. Yang and K. K. de Groh, “Materials issues in the space environment,” *MRS Bulletin*, vol. 35, no. 1, pp. 12–19, 2010.

[26] Z.-Q. Liu, H. Qiu, X. Li, and S.-L. Yang, “Review of Large Spacecraft Deployable Membrane Antenna Structures,” *Chinese Journal of Mechanical Engineering*, vol. 30, pp. 1447–1459, 2017.

[27] A. Baptista, F. Silva, J. Porteiro, J. Míguez, and G. Pinto, “Sputtering Physical Vapour Deposition (PVD) Coatings: A Critical Review on Process Improvement and Market Trend Demands,” *Coatings*, vol. 8, no. 11, p. 402, 2018.

[28] G. Wahl, O. Stadel, O. Gorbenko, and A. Kaul, “High-temperature chemical vapor deposition: An effective tool for the production of coatings,” *Pure and Applied Chemistry*, vol. 72, no. 11, pp. 2167–2175, 2000.

[29] H. Tsunoda, Y. Senbokuya, and M. Watanabe, “Deployment characteristics evaluation of inflatable tubes with polygon folding under airplane microgravity environment,” *Space Technology*, vol. 25, no. 3, pp. 127–137, 2005.

[30] K. Senda, T. Oda, S. Ota, Y. Igarashi, A. Watanabe, T. Hori, H. Ito, H. Tsunoda, and K. Watanabe, “Deploy experiment of inflatable tube using work hardening,” in *Proc. AIAA Gossamer Spacecraft Forum*, 2006, pp. 1–18.

[31] MatWeb, LLC, "Aluminum 1199-H18." URL: https://www.matweb.com/search/DataSheet.aspx?MatGUID=7a321b89269943629bb6d7a0a4a357b2. [Accessed: Jul. 12, 2024].

[32] L. Filipovic, "Silicon Dioxide Properties." 21 Jan 2013 URL: https://www.iue.tuwien.ac.at/phd/filipovic/node26.html

[33] DuPont Teijin Films, *Mylar H-37232-3: Polyester film product information*, Tech. Datasheet 2003.

[34] J. A. Carr, D. Boyd, A. Martinez, M. SanSoucie, L. Johnson, G. Laue, B. Farmer, J. C. Smith, B. Robertson, and M. Johnson, "The Lightweight Integrated Solar Array and Transceiver (LISA-T): Second generation advancements and the future of SmallSat power generation," *Proc. 30th Annual AIAA/USU Conf. on Small Satellites*, NASA Marshall Space Flight Center, 2016.

[35] A. Babuscia, B. Corbin, R. Jensen-Clem, and K. Kiwak, "Inflatable antenna for CubeSat: Fabrication, deployment, and results of experimental tests," *Proc. IEEE Aerospace Conf.*, 2014.

[36] A. Babuscia, B. Corbin, and R. Jensen-Clem, "Inflatable antenna for CubeSat: A new spherical design for increased X-band gain," 2015.

[37] U. Battista, "Design of net ejector for space debris capturing," *Aerospace Conference*, 2019.

[38] A. Smith, "Atomic oxygen protection of materials for space applications," in *Proc. 8th Int. Conf. on Composite Materials (ICCM8)*, 2019.

[39] I. Hung, "Analysis and Characterization of Multilayered Reflector Antennas: Rain/Snow Accumulation and Deployable Membrane," *IEEE Trans. Antennas Propag.*, vol. 46, no. 11, 1998.

[40] Y. Shlepnev, "Modeling frequency-dependent conductor losses and dispersion in serial data channel interconnects," *Simberian Inc.*, 2007.

[41] G. Perona and M. Allegretti, "A new class of orbiting very large ultra-light orientable MW antennas," *SCIREA J. Electr. Eng.*, 2020.

[42] A. M. M. Emam, *Gossamer Structures Overview: Packing, Deployment, Rigidization and Control*, M.Sc. Thesis, Politecnico di Milano, 2023.